THE PROPERTIES OF POLYMER/SOLVENT SYSTEMS AT SURFACES AND INTERFACES

ROMAN BARANOWSKI

INFORMATION TO USERS

This manuscript has been reproduced from the microfilm master. UMI films the text directly from the original or copy submitted. Thus, some thesis and dissertation copies are in typewriter face, while others may be from any type of computer printer.

The quality of this reproduction is dependent upon the quality of the copy submitted. Broken or indistinct print, colored or poor quality illustrations and photographs, print bleedthrough, substandard margins, and improper alignment can adversely affect reproduction.

In the unlikely event that the author did not send UMI a complete manuscript and there are missing pages, these will be noted. Also, if unauthorized copyright material had to be removed, a note will indicate the deletion.

Oversize materials (e.g., maps, drawings, charts) are reproduced by sectioning the original, beginning at the upper left-hand corner and continuing from left to right in equal sections with small overlaps. Each original is also photographed in one exposure and is included in reduced form at the back of the book.

Photographs included in the original manuscript have been reproduced xerographically in this copy. Higher quality 6" x 9" black and white photographic prints are available for any photographs or illustrations appearing in this copy for an additional charge. Contact UMI directly to order.

UMI

A Bell & Howell Information Company
300 North Zeeb Road, Ann Arbor MI 48106-1346 USA
313/761-4700 800/521-0600

The properties of polymer/solvent systems at surfaces and interfaces.

by

© Roman Baranowski

M.Sc. (Maria Curie-Skłodowska University, Lublin, Poland) 1982

A thesis submitted to the
School of Graduate Studies
in partial fulfilment of the
requirements for the degree of
Doctor of Philosophy

Department of Physics and Physical Oceanography
Memorial University of Newfoundland

(June, 1997)

St. John's Newfoundland

0-612-25767-3

Abstract

In this thesis, a comprehensive study of the structure and physical properties of polymer layers, carried out using numerical self-consistent field theory, is presented. Diblock copolymer with one of the blocks adsorbed at the surface and the second block dangling into solution, and forming the polymer brush is considered. For many properties, the results are compared with experimental data, therefore realistic values of the statistical segment lengths, interaction parameters, densities of pure materials and molecular weights are used throughout the calculations. In other cases, model calculations are performed and the results are compared with the analytical predictions.

The properties of the uncompressed polymer brush are examined first. The thickness, the free energy and density profile, and the dependence of these properties on surface density, molecular weight and solvent quality are examined. The density profile is discussed in terms of its general shape, maximum polymer concentration and its location, and the depletion and tail regions.

Next, the compression of polymer brushes in good and Θ solvents is considered. For each case, the density profile, root mean squared thickness and free energy of the compressed brush, as functions of the molecular weight and surface coverage, are calculated and presented in the form of power law dependences. Three modes of compression are considered: by a second brush adsorbed on a second surface, by a bare, repulsive surface and by a surface which is neutral for adsorption. The

interpenetration of opposing layers is quantified and the results are compared with recent numerical studies.

Finally, surface pressure effects in the adsorbed layers are examined. First, a homopolymer/poor solvent system with an attractive surface interaction is considered. The surface pressure as a function of coverage is calculated. Then the copolymer/solvent system is considered in which the anchoring block is the same as the homopolymer and the solvent is good for the dangling block. Both blocks are incorporated within the self-consistent formalism. The excess surface pressure for this system is calculated and compared with recent experimental work in which rapid increases were observed.

To my wife Elżbieta, son Filip

and to my parents.

Contents

List of Tables

List of Figures

Acknowledgements

I would like to take this opportunity to thank all those who have made contributions to this dissertation.

First and foremost, I wish to thank my thesis supervisor, Dr. Mark D. Whitmore, for his constant support, encouragement and extremely helpful assistance in completing this thesis. I also thank him for sharing his knowledge and expertise in physics for many discussions which led to my fascination by polymers.

I thank Dr. John Whitehead and Dr. John deBruyn for acting as members of my Supervisory Committee, for their critical guidance and insightful comments and helpful suggestions on my thesis work in its final stage.

I am very grateful to Dr. Michael S. Kent for many discussions and for freely sharing his data.

I gratefully acknowledge the financial assistance by the School of Graduate Studies and Department of Physics in the form of graduate fellowships.

I also wish to acknowledge research assistance from the High Performance Computer Centre in Calgary.

I would like to thank all my friends in St. John's. Here, far away from my home, I have met many wonderful people who shared with me their lives and helped me in many ways. Thanks a lot for everything.

I also want to express thanks to my wife Elżbieta, and son Filip. Without their unwavering support, love and constant affection it would not have been possible to

write this thesis.

I extend my sincere thanks to all my friends and family in Poland for their constant interest, support and belief in me.

Chapter 1

Introduction

1.1 Polymers at Surfaces - General Remarks

Structures formed by polymers constitute a field of very diverse and interdisciplinary studies. The variety and complexity of polymer systems arising from a few simple building blocks inspire much experimental and theoretical work. and physicists. chemists and material scientists are all active contributors.

One of the aspects of polymer science which. in recent years. has attracted considerable interest is the structure and the properties of polymer systems near surfaces and interfaces. These interfaces are very important in many commercial applications such as blends. composite materials. adhesives and coatings. The adsorption or grafting of polymers onto surfaces is of importance in a number of other areas. A favored current application is the coating of medical devices with polymer surfaces that form strong repulsion layers; this technology is used in the manufacture of bioimplants. A more comprehensive understanding of how different types of polymers organize at the surface may provide further advances in the design of such biomedical devices. There is also strong interest in the lubricating properties of these layers in contact with the tissue and other biomatter. Furthermore, diblock copolymers are the high-molecular-weight analog of short-chain amphiphilic molecules. They may be surface active and may form a variety of phases (micellar, lamellar and cylindrical among many others). Thus, they can be used in the prevention of protein adsorbtion to biosurfaces and in the design of new drug delivery systems. The successful design of these polymeric materials depends on the physical and chemical properties of all the constituent elements and this, in turn, requires a fundamental understanding of the relationship between the molecular architecture and thermodynamic properties of such polymer systems.

Polymers are large molecules consisting of repeated chemical units (*monomers*) bonded together. The simplest architecture is a linear homopolymer: identical units are joined in a line, much as a chain is built up from its links. In other cases, the chains are branched or interconnected to form three-dimensional structures. Further complexity can arise from the fact that polymer chains can be built from two or more kinds of monomers and assembled into distinct blocks, first one species and then another. The resulting structure is referred to as *a block copolymer.*

When polymer molecules are immersed in a solvent, their behavior depends strongly on the interaction between the solvent and polymer molecules. One can distinguish between good, poor and Θ solvents. A good solvent is one in which a polymer of infinite molecular weight would dissolve. A poor one is one in which it would not. Finally, a Θ solvent corresponds to the cross-over between good and bad solvent. Diblock copolymer/solvent systems are the primary focus of this thesis.

Near a surface, large molecules experience constraints on their configurations and experience interactions that differ from those in bulk. When a solution comprised of different polymers and solvent is in contact with a surface or air-liquid interface, the constituents of the polymer solution which can best accommodate the constraints and interactions tend to concentrate near surface. Furthermore, the molecular connectivity of the polymers can effectively link the surface to the interior of the system, or in other words, a long chain located near the surface can also extend relatively deeply into the bulk of the system. It is convenient to consider three types of surfaces. In general, one can think of the surface exerting attractive, neutral or repulsive forces on the polymer in solution. The range of this interaction is also important; it can be short or long-range. All these effects can be enhanced or diminished by the quality of the solvent.

The interfacial properties of homopolymer chains in a solution depend strongly on their affinity towards the surface. If the surface is attractive, then an adsorbed layer forms. Repulsive interactions between the surface and the monomers result in a reduction of the amount of homopolymer near the surface, often referred to as depletion. When one end of every polymer chain is attached to the surface by functionalized end-groups, the interfacial properties of such a structure depend not only on the properties of the surface but also on the grafting density. If the grafting density is high enough such that the chains stretch away from the surface, a structure referred to as a polymer brush is formed. For end-grafted homopolymers, an attractive monomer-surface interaction can also lead to adsorption of the polymer chain at the surface. Conversely, if only the grafted end is attracted to the surface, a depletion layer is formed and the density of polymer near the surface is lowered. Polymer brushes can also be formed by a selective adsorption of diblock copolymers. The block with the higher surface affinity (anchoring block) adsorbs onto the surface and the second block (buoy) extends to at least some degree into the solution. When the density of adsorbed chains in the vicinity of the surface is high enough such that the dangling chains stretch away from the surface, a polymer brush is formed.

This variety of possible situations, as well as the complexity of each system, make the study of polymers at surfaces interesting and challenging. Prediction of the structure and physical properties of copolymer/solvent systems near surfaces and interfaces is the objective of this work. Polymers at an air-liquid interface are present in a number of systems including composite materials and colloidal dispersions, thus such theoretical predictions can be technologically important [3]. Additional motivation for this work is provided by the possibility of coupling the results presented in this work to a number of experimental studies [1, 2].

The picture of homopolymer adsorbed at the surface can be described as a continuous succession of "loops" and "trains" as well as "tails". A train is a series of consecutive segments, all in contact with the surface. A loop consists of segments, all extending into the solvent; it is bound by a train on each side. A tail is terminally bound to a train; the outer end dangles into the solution [4]. The adsorption of homopolymers, when each monomer can adsorb at the surface, is rather well understood at present. At low surface concentrations when neighboring adsorbed chains do not overlap, the conformation of macromolecules is determined primarily by the value of the adsorption energy of each monomer [5]. At high surface coverage, the structure of the adsorption layer depends also on the concentration, chain flexibility, adsorption energy and polymer-solvent interaction as well as the molecular weight of the adsorbing chains. The physical description of the adsorbed layer contains the details of the density distribution profile, thickness of the adsorbed layer, as well as the adsorbed amount, Γ, which is defined as the total number of monomers per unit area which belong to the adsorbed layer.

A different structure is formed by end-grafting technique. Homopolymer chains are terminally attached to the surface or interface and, depending on the grafting density, different regimes are considered. The main factors which determine the properties of these polymer layers are the degree of polymerization of the chain, Z, the quality of the solvent, and the average area per adsorbed molecule, Σ. As is commonly done, it is useful to introduce the reduced surface concentration, σ^*, defined by

$$\sigma^* = \frac{\pi {R_g}^2}{\Sigma} , \tag{1.1}$$

where R_g is the radius of gyration of an isolated polymer in the solvent, with $R_g \propto Z^\nu$.

where $\nu \approx 0.5$ or 0.6 in Θ or good solvent, respectively. In worse than Θ solvent $\nu \approx 1/3$ [6]. To within a numerical factor, σ^* is the ratio of the cross sectional area of a molecule in solution to the average area associated with it in the grafted state.

Two limits are commonly identified and schematically presented in figure 1.1. In the first, $\sigma^* \ll 1$, the distance between the grafting points is greater than R_g. The chains are isolated from one another, and extend a distance which is proportional to R_g from the surface. This limit is known as the "mushroom regime" [7]. In the other limit, which corresponds to $\sigma^* \gg 1$, the average area per grafted chain is much smaller than the cross sectional area of a chain in a solution, and they are obliged to

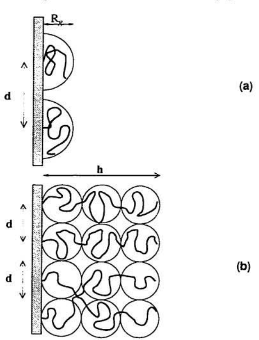

Figure 1.1: Polymer chains attached by one end to nonadsorbing surface. Mushroom (a) and brush (b) regimes. The brush thickness is h.

stretch away from the surface. This limit is frequently referred to as the brush limit and will be considered in this thesis.

The adsorption of diblock copolymers depends very strongly on the quality of solvent for each block of the copolymer. One can distinguish between non-selective and selective solvents. If the interaction parameters between the solvent molecules and both blocks of the copolymer are similar, the solvent is called non-selective. The adsorbed block can be interpreted in terms of a self-similar, "fluffy carpet" structure [8]. In the case of a selective solvent the solvent is poor for one block and good for the other. The block for which the solvent is poor can then adsorb onto the surface, and the second dangles into solution. The adsorbed block is interpreted in terms of molten and swollen by solvent layer [9]. In either selective or non-selective solvent the dangling block is similar to the end-grafted homopolymer and is treated as a polymer brush.

In order to fully describe the adsorption layer, both the details of the density distribution profile and the free energy of the system have to be determined. Most of the other thermodynamic quantities can be derived or calculated from the free energy. In most analytical and numerical approaches the Helmholtz free energy, F, of the system is specified. Usually it is expressed as a sum of two contributions - the interaction energy, which involves all components of the system and the interaction with the surface, plus the entropic contribution. Then the surface tension γ can be calculated using

$$\gamma = \left(\frac{\partial F}{\partial \mathcal{A}}\right)_{T,V,N_\kappa} , \qquad (1.2)$$

where $\mathcal{A}$ is the total area of the interface, T is the temperature, V is the volume of the system,and N_κ are the numbers of the molecules of species κ present in the system.

In the case of the air-liquid interface the change in the surface tension can be interpreted as a two-dimensional pressure. This change is called the surface pressure

$$\Pi_a = \gamma_0 - \gamma . \qquad (1.3)$$

where γ_0 is the surface tension of the pure solvent and γ is the value with an adsorbed polymer.

Polymer layers at surfaces or interfaces have been extensively studied theoretically and experimentally, and in the following sections some important and relevant results will be discussed in detail.

1.2 Analytic Theories of Polymers at Surfaces

The ultimate goal of every polymer adsorption theory is to provide a description of the polymer concentration in the vicinity of the surface as well the physical properties of the adsorbed layer. One can categorize each theoretical method as either an analytical or a simulation technique. In this section, analytic descriptions of homopolymer adsorption will be discussed first. Next, analytic models of end-grafted homopolymers and nonadsorbing surfaces will be considered. Finally some models for diblock copolymer adsorption will be presented.

1.2.1 Homopolymer Adsorption

There are two major analytic approaches to the description of homopolymer adsorption. i.e., scaling [10-16], and mean field descriptions [17-19].

The scaling description of homopolymer adsorption from good and Θ solvents was developed by de Gennes [10, 12]. It is based on the concept of the correlation length. ξ, introduced by scaling theory in the description of dilute and semidilute polymer solutions [5]. The central result of this theory is that this correlation length. ξ. is proportional to the concentration of polymer in solution. ϕ. which scales as

$$\frac{\xi}{a} \simeq \begin{cases} \phi^{-3/4} & \text{good solvent} \\ \phi^{-1} & \Theta \text{ solvent} \end{cases} , \tag{1.4}$$

where a is the monomer length. This result was used to derive power law dependences for different parts of the polymer density profile in the vicinity of the surface. The adsorbed layer is divided into three regions:

1. The *proximal regime*, $x < D$, close to the surface where the profile is very sensitive to the details of the segment-surface interaction. The parameter D is approximately the thickness of an isolated adsorbed polymer chain and is determined by the adsorption energy parameter δ.

2. The *central regime*, $D < x < \xi_b$, where the profile follows a universal scaling law, and for the adsorbing wall is independent of the bulk concentration. ξ_b is

the bulk correlation length and it is assumed that D and ξ_b satisfy [10]

$$a \ll D \ll \xi_b \,. \tag{1.5}$$

3. The *distal regime*, $x > \xi_b$, where the density profile, $\phi(x)$, approaches the bulk concentration, ϕ_b, exponentially.

In general, the adsorbed amount Γ is obtained by integrating $(\phi(x) - \phi_b)$ over the distance from the surface and depends on the adsorption energy and the number of segments per chain as well as the quality of the solvent. Similarly, one can also obtain the expression for the free energy or the interfacial tension, γ. The detailed discussion of these quantities and their dependences on relevant parameters goes beyond the scope of this thesis but can be found in the literature [13, 14, 16, 20].

The scaling theory provides only global information on the properties of adsorbed homopolymers. Furthermore, it is valid over rather limited range of conditions. There are several analytic treatments of homopolymer adsorption based on the mean field approach. Jones and Richmond [18] considered adsorption from solution onto a planar surface using the self-consistent field theory (SCF) of Edwards and Dolan [21, 22]. They discussed adsorption from Θ and good solvents. Their approach is based on the ground state approximation for the solution of a diffusion equation. The probability distribution function for a polymer of Z segments starting at $\boldsymbol{r}$ and ending at $\boldsymbol{r}'$ which satisfies the diffusion equation is expanded in terms of eigenfunctions with corresponding eigenvalues, and only the lowest eigenvalue and corresponding eigenfunction is assumed to contribute to the solution.

Another approach is based on the square gradient theory introduced by Cahn and Hilliard [17], and developed for polymer adsorption by Poser and Sanchez [19] and by de Gennes [10]. In this method the local contribution to the surface tension or free energy excess is decomposed into a concentration gradient term and a concentration dependent term. The interfacial tension can be written as

$$\gamma = \int_0^\infty dx \left[L(\phi) \left(\frac{d\phi}{dx} \right)^2 + F(\phi) \right] . \tag{1.6}$$

The stiffness function $L(\phi)$ represents the energy cost of making local changes in the polymer concentration [10] and, for low polymer concentration, can be written [23]

$$L(\phi) = \frac{k_B T}{a^3} \left(\frac{a^2}{24\phi} \right)^2 , \tag{1.7}$$

where ϕ is the local volume fraction of homopolymer and a is the monomer size. The second term in Eq. (1.6) represents the free energy density difference associated with the transfer of molecules from bulk to the adsorbed layer

$$\frac{F(\phi)}{k_B T} = \frac{1}{a^3} \left(\frac{\phi}{Z} \log \phi + \frac{1}{2} v \phi^2 + \frac{1}{6} w \phi^3 + \cdots \right) , \tag{1.8}$$

where Z is the degree of polymerization and v and w are the excluded volume and ternary interaction coefficients respectively. Equation (1.8) was first introduced by Flory [24]. By minimizing γ, the equilibrium profile and free energy excess can be obtained. For some cases analytic solutions for adsorption from good [10, 23] and Θ solvents [23, 25], and for worse than Θ solvents [26], have been found.

The interesting and very detailed discussion of these aspects of homopolymer adsorption is also presented in a comprehensive book by Fleer *et al.* [27].

1.2.2 End Grafted Homopolymer

There are two main analytical approaches to highly stretched polymer brushes. the scaling [7, 11, 28], and mean field [29, 30]. The scaling theory of polymer brushes. formed by end-grafting, in a good solvent was developed by Alexander and de Gennes (ADG) [7, 28]. They consider a flat. nonadsorbing surface bearing monodisperse chains of Z monomers characterized by mean statistical segment length. b. such that $Z\,b$ gives the full contour length of the chain. The theory is based on the concept of "blobs" of linear size d. where d is the average distance between grafted sites on the surface (see Fig.1.1 b). Introduction of this characteristic length scale leads to a density profile which, except for a small depletion zone and a tail region. is a step-like function. i.e., the polymer volume fraction within the layer. $\phi \approx Zb^3/d^2h$. is constant and h is the equilibrium layer thickness. The grafting density of chains can be expressed in dimensionless terms as $\sigma = b^2/d^2$. Furthermore. the model assumes that all the chains are uniformly stretched, so the free end of every chain is located in the tail region of the brush. Dense grafting results in strong overlap among the chains and this increases the number of monomer-monomer contacts and the corresponding interaction energy. This effect is reduced by stretching the chains along the normal to the grafting surface, but results in an increase of the layer thickness. h. The interplay between the interaction energy and the entropy loss due to stretching, or in other words, the increase of elastic energy, determines the equilibrium value of h.

There are two ways to obtain an explicit expression for the free energy per chain. The first is based on a simple Flory type mean-field argument [24], and the free energy per chain (in the units of k_BT) is written as

$$F_c \approx v\phi^2 \frac{d^2h}{b^3} + \frac{h^2}{Zb^2} \,. \tag{1.9}$$

where v is a dimensionless excluded volume parameter (a measure of binary monomer contacts) and $Z^{1/2}b = R_0$ is the *rms* end-to-end distance of an unperturbed, ideal chain. In the above Eq. (1.9) the symbol $\approx$ means that every term should be multiplied by some numerical factor of order one. The first term represents interactions (ϕ is h dependent) and the second one is the elastic contribution. In terms of grafting density, σ, and the degree of polymerization, Z, Eq. (1.9) can be expressed as

$$F_c \approx v\frac{Z^2\sigma}{h} + \frac{h^2}{R_0^2} \,. \tag{1.10}$$

The second way to estimate the free energy per chain in a brush is based on scaling arguments. A polymer chain in this picture is considered to satisfy ideal Gaussian behavior on the scale of blob size d. The correlations of the monomers inside each blob result in an interaction energy of order k_BT. Since the number of blobs per chain is (Z/g), where $g = (d/b)^{5/3}$ is the number of segments per blob, the interaction energy can be written as

$$F_{int} \approx \frac{Z}{g} \approx Z\left(\frac{d}{b}\right)^{-5/3} \approx \phi^{9/4}\frac{d^2h}{b^3} \,. \tag{1.11}$$

The elastic free energy is modified in the terms of blob picture by recognizing that the chain can be considered as ideal at larger scale and

$$F_{el} \approx \frac{h^2}{R^2} , \tag{1.12}$$

where $R \approx (Z/g)^{1/2} d$ is the radius gyration of an unperturbed chain of (Z/g) blobs, each of size d [31]. In contrast to the first approach, the elastic contribution here is concentration dependent. The total free energy per chain (in $k_B T$ units) can be written in terms very similar to Eq. (1.9), but now the term describing the elastic contribution has become explicitly ϕ dependent:

$$F_c \approx \phi^{9/4} \frac{d^2 h}{b^3} + \phi^{1/4} \frac{h^2}{Z b^2} . \tag{1.13}$$

Expressing the volume fraction of the polymer in terms of the grafting density and the degree of polymerization results in

$$F_c \approx Z \left(\frac{Z b \sigma}{h} \right)^{5/4} + Z \sigma^{1/4} \left(\frac{h}{Z b} \right)^{7/4} . \tag{1.14}$$

The equilibrium state of the brush is obtained by minimizing the free energy with respect to h. The two approaches result in the same scaling for the thickness of the brush, i.e.,

$$h \propto Z \sigma^{1/3} . \tag{1.15}$$

but slightly different dependence of the equilibrium free energy per chain, F_c,

$$F_c \propto \begin{cases} Z\sigma^{2/3} & \text{Flory - type argument} \\ Z\sigma^{5/6} & \text{Scaling - type argument} \end{cases} . \tag{1.16}$$

The difference in the power of σ between the Flory type approach and scaling picture reflects differences in the elastic and interaction terms in the free energy, which can be seen by a direct comparison of Eqs. (1.9) and (1.13). Both terms of Eq. (1.9) differ by a factor of $\varphi^{1/4}$ from the corresponding terms in Eq. (1.13) [5, 32]. This difference can be accounted for the fact that in the Flory - type argument the correlations within each blob are neglected. A difficulty in both approaches, however, is the assumption of a uniform density profile.

A more detailed picture of the density distribution within the polymer brush was proposed in the analytic SCF model developed independently and simultaneously by two research groups: Milner, Witten and Cates (hereafter referred to as MWC) [29, 33], and Zhulina, Borisov, Pryamitsyn and Birshtein [34]. The key point of this analytical model is based on the analogy drawn by Semenov [35], that a configuration of weakly stretched or unstretched chain is analogous to the possible trajectories of a quantum-mechanical particle, whereas in the limit of complete stretching, the chain configuration is reminiscent of the trajectory of a classical particle. Consequently, for strongly stretched chains, the analytic SCF model looks for the dominant trajectory between the two given endpoints for which the classical action is at a minimum [33]. Furthermore, in this model the assumption that all the chains have their free end in the periphery of the layer is relaxed and, instead, chains can have their free ends anywhere within the brush. If one begins the trajectory at the free end of each chain, no matter what the conformation, it takes Z steps (monodisperse chains) to arrive at the surface, beginning with zero stretching (mechanical equilibrium condition). In the mechanical analogue, the chain path, $x(\tau)$, is the particle trajectory; the monomer number τ corresponds to time; the chain length Z is the total time of flight of the particle; the local chain stretching $dx/d\tau$ is the particle velocity; and the condition that the free end of the chain is unstretched corresponds to a particle starting from rest [30]. The next step is the self-consistent determination of the mean-field potential. A harmonic field has these properties; the period of an oscillator in a harmonic field is not dependent on the amplitude of oscillation. Since in mean field and for low polymer density the effective potential is proportional to the monomer density the composition profile is parabolic. Using the notation of MWC, this parabolic profile is expressed as

$$\phi(x) = w^{-1}(A(h) - Bx^2) \; , \tag{1.17}$$

where w is an excluded volume parameter with dimensions of length^3 [36]. x is the distance from the grafting surface and h is the thickness of the brush. The constant $A(h)$ is fixed by requiring that the number of monomers per unit area equal $Z\sigma$. The constant B is obtained by the equal "time" requirement [29]. Again using their notation, the result is

$$\begin{aligned} \phi(x) &= \frac{\pi^2 v}{8Z^2 w}(h^2 - x^2) && (1.18) \\ h &= \left(\frac{12}{\pi^2 v}\right)^{1/3} (\sigma w)^{1/3} Z \; , && (1.19) \end{aligned}$$

where v has dimensions of length^{-2} and can be related to statistical segment length discussed in the next chapter.

The free energy per chain in the MWC model is obtained by progressively adding chains; the change in system free energy upon adding a chain is $s(\sigma)$ for that chain. The $s(\sigma)$ is independent of the location of the chain's free end, and the free energy can be calculated by considering the chain which starts very near the surface [29]. It results in

$$F_c = \frac{9}{10}\left(\frac{\pi^2 v}{12}\right)^{1/3}(w\sigma)^{2/3}Z\,. \tag{1.20}$$

These solutions are strictly correct in the limit of infinite molecular weight, highly stretched molecules and low to moderate polymer density. In this limit the depletion region near the surface and the extended tail can be neglected because the total thickness of the layer scales linearly with the degree of polymerization. Similarly, for the long stretched chains the fluctuations around the most probable trajectory are negligible in the high molecular weight limit. In later work, Milner, Wang, and Witten formally considered finite molecular weight corrections [37], and MWC included polydispersity [38]. Each of these corrections is most important at the tip of the brush.

An important conclusion of the MWC model is that the simpler Alexander-de Gennes picture based on the step profile gives the same scaling relationships for the thickness of the brush, Eqs. (1.15) and (1.19), but with different numerical prefactors. The scaling relationships for the free energy per chain are also essentially the same in both models, except for a slight difference in the case when one applies the blob picture in determining the elastic and interaction contributions, Eqs. (1.16) and (1.20). The analytical SCF treatment of MWC includes the same physics as the ADG model, namely, it balances the osmotic type interactions with the elastic resistance to stretching, but does it locally at every point along the chain rather than globally over the entire chain. The difference arises physically from the reduction in stretching with increased distance from the surface, since the decreasing density means that there is more space to relieve crowding.

Both the scaling and analytical SCF models also discuss the compression of polymer brushes, which is one of the earliest experimental techniques used to investigate their properties and structure. Both models assume that the opposing brushes do not interpenetrate, at least at the initial stage of compression. An argument for the non-interpenetration assumption is that the stretching which occurs in the single layer is caused by swelling into the pure solvent bath in order to reduce osmotic interactions within the brush. When the two layers are brought into contact, this tendency is removed, so the layers retract to reduce their stretching energy [39]. Hence, the compression of the two brushes becomes equivalent to compression of two non-interacting brushes by a nonadsorbing surfaces. Furthermore, the profiles are assumed to retain their original shapes, with suitable increase in densities. Thus, the ADG profiles remain flat, and the MWC profiles remain parabolic up to the midpoint between the surfaces, where there is a discontinuity in the slope. Both theories predict that the free energy per unit area of the compressed brush, E, can be expressed in terms of a free energy per unit area of the uncompressed brush, E_0, and some universal function of the reduced distance, $u = D/(2h)$, where D is the distance between the surfaces with terminally attached chains and h is the thickness of the uncompressed polymer brush

$$E \sim \begin{cases} E_0\left(\frac{1}{u} + \frac{u^2}{2}\right) & \text{ADG} \\ E_0\left(\frac{1}{u} + u^2 + \frac{u^5}{5}\right) & \text{MWC} \end{cases} . \qquad (1.21)$$

The lateral compression of the polymer brush formed at the air-liquid interface results in a change in the grafting density and, according to Eq. (1.3), the MWC or Flory mean field models predict that the surface pressure scales as

$$\Pi_a \propto Z\sigma^{5/3} , \qquad (1.22)$$

and the scaling picture of ADG, which takes into account the correlations of the monomers inside the blob predicts

$$\Pi_a \propto Z\sigma^{11/6} . \qquad (1.23)$$

The details of the structure and scaling relations for the polymer brush under good solvent conditions and detailed comparison with analytic theories as well as comparison with the experiments will be discussed in chapter 3. Interpenetration of the brushes, and the functional dependence of the free energy of the compressed brush, will be examined in chapter 4. The surface pressure effects and the scaling relation of Eq. (1.22) will be examined and discussed in chapter 5.

The structure of end-grafted chains in Θ and worse than Θ solvent has been the subject of several analytical studies [40-47]. In the laterally homogeneous layer in

Θ and worse than Θ solvent, inhomogeneities can develop leading to the "dimpled" structure [45, 48], but as long as the density of grafting points is large enough that the neighboring chains overlap, polymer brushes still form with the chains stretching away from the surface [45]. The essential idea of the ADG model, a global balance of interaction and stretching energies, was applied by Halperin [41] for monodisperse chains irreversibly bonded to a flat, solid surface, and Zhulina *et al.* [42] who extended this type of analysis to cylindrical and spherical surfaces. In these studies the scaling relations for the thickness of the brush and the equilibrium free energy in Θ and worse than Θ solvents were obtained, and for the planar surface, thickness of the brush scales as

$$h \propto \begin{cases} Z\sigma^{1/2} & \Theta \text{ solvent} \\ Z\sigma & \text{worse than } \Theta \text{ solvent} \end{cases} . \tag{1.24}$$

and the equilibrium free energy per chain

$$F_c \propto \begin{cases} Z\sigma & \Theta \text{ solvent} \\ Z & \text{worse than } \Theta \text{ solvent} \end{cases} . \tag{1.25}$$

It is worth noting that, for worse than Θ solvent, the free energy per chain is independent of surface concentration. In this model, as in the ADG picture, the density distribution is assumed to be constant within the layer. In order to obtain these asymptotic relations, only the leading terms were kept during the minimization of the free energy expression with respect to the height of the brush. For Θ solvent, these were the elastic stretching and the ternary type interactions, Eq. (1.8) with

$v = 0$, approximated through $F_{int} \propto \phi^3$, while for worse than Θ solvent only binary and ternary interactions were considered as dominant and the stretching of the chains was neglected.

A more detailed and complete theory of the structure of a planar layer in other than good solvent conditions was presented by Zhulina *et al.* [42, 43], and by Shim and Cates [40]. The approach proposed by Zhulina is essentially the same as MWC: the interaction and stretching energies are balanced locally. The scaling relations for the thickness and equilibrium free energy are recovered as in the simpler Flory type picture but the density profile obtained in Θ solvent conditions is described by an elliptic function. Shim and Cates [40] exploited the "equal time" requirement of the self-consistent potential and derived a set of coupled integral equations for the density profile of the end-grafted chains and the free energy of the system in equilibrium as well as during the compression of two polymer layers. The result for the density profile in Θ solvent is elliptic and the same as was obtained by Zhulina *et al.* [42, 43]. The assumption of noninterpenetration is still a key point in calculations of the free energy of the system during compression. In this picture, the compression of the polymer layer by the second brush is assumed to be equivalent to a compression by an impenetrable wall. The analytic solution can be obtained only for a very simple case (athermal solvent, $\chi = 0$).

1.2.3 Diblock Copolymer Adsorption

In the previous section the properties of the polymer brushes were discussed and this discussion can be applied to the dangling block of the adsorbed diblock copolymer. This section is meant as a short description of the adsorption of diblock copolymers.

Scaling and mean field descriptions of diblock copolymer adsorption from non-selective and selective solvents were originally proposed by Marques *et al.* [8, 9]. In non-selective solvent, they considered an $A - B$ diblock copolymer, adsorbing from a dilute solution onto a solid surface which strongly attracts the A block and strongly repels the B block. The solvent was considered to be good for both blocks. The structure of the adsorbed layer was described as consisting of a swollen anchoring layer and a more dilute and extended buoy layer. The key parameter in determining the layer structure is the relative length of the blocks expressed in terms of the asymmetry ratio, β, which is

$$\beta = \frac{R_B}{R_A} = \left(\frac{Z_B}{Z_A}\right)^{3/5} \quad . \tag{1.26}$$

where R_A and R_B are the radii of gyration of the anchored (strongly attracted) and buoy (strongly repelled) block respectively, and Z_A and Z_B are the corresponding degrees of polymerization. When the asymmetry is small, the adsorbing block forms a self-similar layer which corresponds to the same type of profile as in homopolymer adsorption, and the nonadsorbing block forms a brush-like structure. When the nonadsorbing block is much larger than the adsorbing one, the anchored block forms a discontinuous "pancake" structure and the B block remains stretched and forms a brush structure. The scaling relations for the thickness of the adsorbed and dangling layer as well as the average surface concentration are obtained through minimization of the free energy functional.

In a highly selective solvent, the A block is in a poor solvent environment. This leads to its collapse on the surface and it forms a molten layer on the solid wall where the solvent does not penetrate. The B block is considered to be in a good solvent environment and forms a brush grafted on this molten layer. The structure of the adsorbed layer is governed by the chemical potential of the soluble block in solution, μ_{ex}. An important issue of this work is the role of the van der Waals interaction between the wall and the adsorbed A layer. The asymmetry between the two parts of the copolymer is measured by

$$\beta = \frac{Z_B^{3/5}}{Z_A^{1/2}} . \tag{1.27}$$

If the copolymer asymmetry is large enough, the thickness of the molten layer results from a balance between the van der Waals energy and the stretching energy of the brush. Various other adsorption regimes occur when the asymmetry of the copolymer is decreased [8].

1.3 Summary of Relevant Experimental Work

The present rapid growth in the experimental activity in the field was initiated with the surface force measurements on layers of adsorbed copolymers by Hadziioannou *et al.* [49], and Patel *et al.* [31], and on end-grafted polymers by Marra *et al.* [50], and Taunton *et al* [51]. Subsequent and current experimental work includes force balance measurements [52-54] , small angle neutron scattering (SANS) [55, 56], and neutron reflectivity measurements [1, 57, 58]. Excellent reviews of experimental techniques are presented by Stamm [59], Tirrell and Parsonage [60], and Garbassi, Morra and Occhiello [3]. In this section representative experimental results which are relevant to this thesis will be discussed. More extensive descriptions will be provided in later chapters, when the results obtained in this thesis are discussed.

The polymer density profiles can be directly probed by neutron scattering and reflectivity experiments. Field *et al.* [61] used neutron reflectometry to measure the density profile of four PS-PEO copolymers adsorbed on quartz from deuterated toluene. The profiles of the dangling PS could be well described by a parabolic or error function with maximum at the surface and an exponential-like tail. Using SANS, Cosgrove *et al.* [55] studied one deuterated PS-PVP copolymer adsorbed onto mica with the d-PS dangling into good solvent. The data suggested the presence of a depletion layer and a maximum in the polymer density about 3 nm from the surface, followed by a decrease which is similar to the parabolic form. Auroy *et al.* [56, 62] used SANS to study PDMS polymer grafted onto porous silica, with Z_{PDMS} ranging from about

350 to 8,000. They found that a consistent density profile of the ADG form could not be constructed, and concluded that a parabola with a smooth tail was indicated. However, in contrast to the results of Cosgrove *et al.* [55], they detected no depletion layer near the surface for the good solvent case, which they suggested could be due to a surface-monomer attraction. Overall, therefore, a picture of the profiles is emerging which indicates a maximum at or near the surface (depletion layer), beyond which the density monotonically decreases, smoothly reaching zero at the tips. The SCF theory of MWC however, predicts a profile for monodisperse polymer with no depletion layer and an abrupt drop to zero density at the outer edge of the brush.

Many of the experimental and numerical results have been analyzed in terms of the scaling relations given by the scaling picture of ADG (Eq. (1.15)), and the analytic SCF theory of MWC (Eq. (1.19)), and the results have often been claimed to support them. The actual degree of this support is dependent on assumptions made in the analyses, and limited by the fact that, until the recent work of Kent *et al.* [1, 2] there have been no experiments in which the molecular weights and surface densities were independently varied.

Hadziioannou, Patel and coworkers [31, 49] carried out surface force measurements on PS brushes in toluene, with PS degrees of polymerization, Z_{PS}, of about 600 and 1,500. On the basis of the surface separations at which the forces began, these experiments were said to support the scaling of Eqs. (1.15) and (1.19). However, Ansarifar and Luckham [63] later studied poly(t-butylstyrene) (PBS) brushes in toluene, with $Z_{PBS} \simeq 50$, 200 and 400, and were able to incorporate their results and those of Patel *et al.* [31] within one, much weaker, scaling law, $h^* \propto Z^{0.7}$. Marra and Hair [50] also studied PS/TOL. A comparison of the cases with $A_{PS} \simeq 850$ and 2,400, which had nearly equal values of Σ, suggests that the range of the force scaled faster than linearly with Z_{PS}. This can be explained by the additional complication that the interpretation of these experiments depends on the definition of the range of the force [64]. If it is defined by the surface separation at which the force reaches a given value, e.g. the threshold for measurement, then its scaling differs from that of the brush height: if the brush height scales as $h^* \propto Z^{\alpha}$, then this range of the force would scale approximately as $Z^{\alpha-0.2}$.

As another illustration of the difficulties in data interpretation, Field *et al.* [61] found that, by assuming $h^* \propto \sigma^{1/3}$, then the best fit for the molecular weight dependence was $h^* \propto Z^{0.97}$. However, if no *a priori* assumptions are made, then the best fit to their published data gives $h^* \propto Z^{0.73}\sigma^{0.14}$, in sharp contrast with Eq. (1.15) and similar to the Ansarifar and Luckham result [63].

The point to be emphasized is that determining the quantitative dependences of the brush thickness on both molecular weight and surface coverage has been problematic, and these results do not, necessarily, indicate that the systems are in the asymptotic scaling regime. In particular, until very recently, there has been only one surface coverage for a given molecular weight in each experiment. This situation changed with the work of Kent *et al.* [1, 2] who studied seven copolymers, with the

PS molecular weight ranging over a factor of about 10. By applying lateral pressure. the surface density was independently varied for each copolymer. also over factors of about 10. Hence, they were able to extract quantitative functional dependences of the brush thickness, and to fully compare them with the scaling predictions of the asymptotic theories. The experiments of Kent *et al.* [1. 2] also provide detailed information on the density profiles. including the depletion layer.

One general conclusion that can be drawn from these experiments is that. except for the experiments by Auroy *et al.* [56. 62] and Karim *et al.* [58] on systems at very high σ^*, the coverage in real experiments is limited to $\sigma^* \lesssim 15$. and they do not correspond to the asymptotic regime of analytic theories.

The properties of compressed brushes can be probed by measuring the long range forces between the surfaces with adsorbed polymer. The results are conveniently expressed in terms of $F(D)/R$ where R is the geometric mean of the radii of curvature of cylinders used in the Israelachvilli force apparatus and D is the distance of closest approach. With the Deryaguin approximation [65]. this is directly related to the free energy per unit area for flat. parallel plates via

$$\frac{F(D)}{R} = 2\pi \Big(E(D) - E(\infty) \Big) \ . \tag{1.28}$$

where $E(D)$ is the free energy per unit area of the system at separation D and $E(\infty) = E_0$ is the free energy per unit area of the system when the brushes attached to the opposite surfaces do not overlap. As discussed in section 1.2.2, the analytic theories predict that these forces can be expressed as universal functions of D/h.

where h is the height of the uncompressed brush.

Most of the experiments on compressed brushes have been analyzed in terms of analytic theories, and they tend to support universal behavior predicted by analytic theories [31, 36, 51, 66]. However, Watanabe and Tirell [52], and Dhoot *et al.* [53], made measurements using highly monodisperse brushes in a good solvent and found that the force and its range were unpredicted by a factor of about 2 in analytic theories.

The experimental studies performed by Kent *et al.* [1, 2, 57] are of great importance in this thesis. First, as noted already, in these experiments both molecular weight and surface coverage for layers of chains tethered to the air-liquid interface were varied independently, each over an order of magnitude. The results presented there contain detail and careful examinations of the density profiles and the scaling relations. Second, in these experiments the maximum attainable surface densities were limited by a sharp rise in pressure, with the result that σ^* varied from about 1 to 12 and is typical of experiments in which the chains have been tethered to the surface from dilute solutions in a good solvent. To date, the systems studied by Auroy *et al.* [56, 62] and Karim *et al.* [58] appear to be the only ones which exceed this coverage. Furthermore, this rapid increase of surface pressure cannot be explained on the basis of analytic theories. The experimental work of Kent *et al.* is the focal point of numerical studies presented in chapter 3 and chapter 5 and in many ways motivates this thesis.

In summary, many questions addressed by experimental studies cannot be explained in terms of analytic theories and more detailed numerical work which is not limited to the asymptotic limits or sharply defined regimes is needed. The relevant numerical results and some theoretical predictions drawn from these studies will be discussed below.

1.4 Numerical Approaches to Brushes and Adsorbed Layers

A system comprised of a large number of interacting macromolecules and solvent molecules is suitable for description in the language of statistical physics. In general, the description of the system proceeds in three steps:

1. Characterization of the various microscopic configurations of the system which are compatible with its macroscopic state and, for every configuration, determination of its energy.
2. Evaluation of the partition function $\mathcal{Z}$
3. Determination of the Helmholtz free energy

$$\mathcal{F} = -k_B T \ln \mathcal{Z} \tag{1.29}$$

Most other quantities of physical interest can be directly obtained from the free energy expression, Eq. (1.29). The way the particular approach addresses points (1) and (2) can be used to classify it to a given type of theory. The methods used to study the polymer system near the surfaces and interfaces vary from the models in which all the properties of the interfacial layer are expressed in the local concentrations and concentrations gradients, self-consistent mean field (SCF) type approaches to Monte Carlo (MC) and molecular dynamics (MD) simulations.

Polymer configurations are modeled as walks in continuous space or on a lattice; thus one can distinguish between continuous and discrete, lattice type models. In the models which start from the density profile, individual conformations of chains are not considered, but only their overall effect on the concentration profile is taken into account. The lattice models of Roe [67], and the square gradient theory of Cahn and Hilliard [17] which describe homopolymer adsorption, are examples of this type of approach. In many mean field approaches, fluctuations of the polymer chains about their equilibrium positions are neglected and the free energy of the system is evaluated for the configuration which corresponds to the sharp maximum in the Boltzmann distribution. The numerical self-consistent field theory presented in chapter 2 and used throughout this thesis is another example of a mean field approach realized in the continuous space and applied to diblock copolymers in the presence of the interface. A slightly different approach is presented by Ploehn [68].

Lattice models, exemplified by the Scheutjens and Fleer theory applied to homopolymer [4, 69, 70, 71], and copolymer [72-74] adsorption, represent space as a discrete lattice with cells of constant volume. The total potential energy is assumed to be the sum of pair interactions, and the surface-monomer interactions are restricted to those lattice sites in direct contact with the surface. In the Scheutjens-Fleer theory, the polymer chains are described as walks on a lattice, and each step is weighted with two factors, a local entropy of mixing and an energy factor describing the nearest neighbor interactions. The lattice sites are occupied by either monomer or a solvent molecule. The space adjoining the surface is divided into parallel lattice layers. At equilibrium, there is a certain concentration profile for segments and for solvent. The entropic weighting factor for any step in this concentration profile depends on the lattice type and on the local concentration in the nearest layers. A set of self-consistent equations are derived and solutions have to be found numerically.

In the MC method, states of the system are generated randomly, and the task lies in the selection of the most probable configurations followed by the averaging of various characteristics over them [75, 76]. Monte Carlo simulations of copolymer at surfaces were reported by Zhan *et al.* [77-79] .

The essential principle of the MD method is to numerically solve the classical Newtonian equation of motion, assuming the potential energies of interactions to be known [76]. MD studies on grafted polymer brushes were reported by Murat and Grest [80-82].

Finally polymers near the surfaces can be also studied by means of the cluster variational method CVM [83] and renormalization group (RG) calculations [84].

Comprehensive reviews of numerical approaches which include SCF calculations in continuum and on lattice, square gradient approaches, MC and MD simulations applied to homopolymer and copolymer adsorption as well as to end-grafted polymers are given by Fleer *et al.* [27], and Sanchez [85]. Many aspects of polymers near surfaces are also discussed in an earlier monograph by Napper [86].

The main focus of chapter 3 of this thesis is the structure of the polymer brush in a good solvent. Numerical SCF calculations have been reported by Whitmore and Noolandi [64], Evers *et al.* [73], Milner [87], Wijmans *et al.* [88], and Carignano and Szleifer [89]. These calculations covered the cases of good, Θ and poor solvents with realistic interaction parameters [64, 73, 87] extremely good solvent with $\chi = -1$ [88], and athermal solvents [88, 89]. All density profiles showed a depletion layer and a maximum, followed by a decrease which terminated in a smooth tail, with some variation in the location of the maximum and extent of the tail. The values of ϕ_m generally depended only weakly on Z. The profile shapes become more parabolic with increasing Z, σ^* and solvent quality, with the depletion layer and tail sizes diminishing relative to the overall size of the profile. As well, for a given degree of polymerization, the degree of stretching increases with solvent quality [64, 88]. Recently, Carignano and Szleifer performed numerical calculation using the single-chain mean field theory (SCMF) on tethered polymer layers in a good solvent [90]. They studied chains consisting of up to 100 segments and surface coverage $\sigma^* \lesssim 20$ and found that, in a good solvent, the mushroom to brush regime is broad and the thickness of the brush scales as $h \sim \sigma^{1/4} Z^{0.9}$ throughout the brush regime. In the study of Shull [91], the numerical Scheutjens-Fleer SCF theory was used and good agreement with the parabolic type profile proposed by MWC was reported.

Murat and Grest [80-82] carried out MD simulations of 7 chains in good solvents with Z ranging from 10 to 200 and surface coverages of $\sigma^* \lesssim 20$. Their density profiles contained a depletion layer near the surface, followed by a quasi-parabolic decrease ending in a smooth tail.

Chakrabarti and Toral [92], and Lai and Binder [93] carried out detailed Monte Carlo calculations, including only hard core repulsions between monomers for the interactions. Together, they treated chain lengths up to $Z = 100$ and surface coverages up to, approximately, $\sigma^* \simeq 15$. All the density profiles showed a depletion layer and maximum, beyond which they could be approximated by parabolas evolving into tails. The distance from the surface to the maximum was on the order of, but slightly smaller than, the radius of gyration, and decreased weakly with increasing σ.

The properties of tethered polymers in a mushroom regime were investigated by Adamuti-Trache *et al.* [84] using RG calculations. They considered excluded volume and variable surface-polymer interactions for the tethered chains in a good solvent and reported qualitative agreement with the experimental results of Kent *et al.* [2].

The compression of polymer brushes and formal comparison with the analytical theories is the subject of the chapter 4. Numerical calculations based on SCF theory were reported by Muthukumar [94] who investigated the compression of polymer brushes by a second brush as well as a hard wall in good, Θ and worse than Θ solvents. The conclusions drawn from this work, however, are only qualitative.

The compression of two polymer brushes and detailed comparison with the analytic theories and the experimental studies was reported by Whitmore and Noolandi [64]. They determined the thickness and shape of the polymer density profiles, obtained approximate scaling relations and the ranges of their applicability, studied finite molecular weights effects, as well as the extent of the interdigitation of layers adsorbed on opposite surfaces.

The calculations performed by Dan and Tirrel [95], and Martin and Wang [96] support the analytical SCF model of compression, except they indicated interpenetration of the opposing brushes during compression. The effect of the interpenetration was also emphasized in the numerical SCF study of Wijmans *et al.* [97]. The numerical two dimensional SCF study on compression of polymer brushes in Θ and poor solvents were also reported by Singh and Balazs [98].

The interactions between grafted polymer brushes in good solvent were also studied by means of MC [99, 100], and MD [101] methods. Chakrabarti *et al.* [99] addressed the interpenetration of polymer brushes and made a direct comparison to the results of Shim and Cates [40]. Their results showed that both compression and interpenetration effects are present as the plate separation is decreased, in contrast with the analytical picture, which predicts no interpenetration of the brushes in such situations. They attributed this discrepancy to the fact that the simulations corresponded to the "non-classical" regime of short chains. Dickman and Anderson [100] performed extensive MC simulations of brush compression in athermal (good) solvent and found that the force between the brushes as well as the structure of the density profiles are in overall agreement with the prediction of the analytic SCF theory of MWC. At high surface coverages, the density profiles of strongly compressed brushes obtained through the simulations resembled the step-function profiles assumed in the scaling theory. The main disagreements between MWC theory and the simulations occurred at large separations, and were attributed to the tails in the density profiles for finite-length brushes.

Murat and Grest [101] performed an MD study of the system of two parallel surfaces with end-grafted polymers in a good solvent. They found that the interaction was purely repulsive and the onset of the force starts as soon as the opposing brushes touch each other before any interpenetration. They also found that, for intermediate values of surface coverage, the force profiles were satisfactorily described by both the scaling and SCF theories, and the interpenetration of the brushes can be described by a simple scaling form.

There have been only a very few numerical studies which have as their subject the rapid increase in excess surface pressure in experiments on diblock copolymer layers at the air-liquid interface [1, 2]. Most of the work deals with the homopolymer adsorbed at the interface and the related reduction of the interfacial tension [23, 102, 103]. An increase of surface pressure was reported by Carignano and Szleifer [90], who performed SCMF (single chain mean field) calculations and found that lateral pressures in the brush regime (good solvent) can be described by an approximate power law dependence, $\Pi \sim \sigma^{2.4}$. Grest [82] has reported MD simulations for end-grafted chains in good solvent in which the surface pressure was found to increase slightly more rapidly than predicted by scaling and analytic SCF models, $\Pi \sim \sigma^{2.5}$. This was also confirmed in SCMF simulations by Carignano and Szleifer [104] who found that surface pressure shows good agreement with analytic SCF theory only when the parabolic density profile is used in the full virial equation. The values of the exponent on order of 2.5 are significantly higher than the values of 5/3 or 11/6 predicted by Eqs. (1.22) and (1.23), but still much lower than the results of experimental observations, in which the values in the range (4.2-6.6) were obtained.

1.5 Outline of the Thesis

This thesis uses numerical SCF theory to study the problems of the structure and properties of the polymer/solvent systems at surfaces that are not addressed fully by other calculations. The general theory for numerical self-consistent field calculations is introduced in chapter 2. The approach is then used to study uncompressed brushes, compressed brushes, and lateral surface pressure effects.

Following de Gennes early work on brushes a great deal of emphasis, in both experimental and theoretical studies, has been placed on the strongly stretched chain regime. Recently, de Gennes [105] noted that many interesting effects can take place in mushroom and intermediate regimes. The numerical SCF calculations presented in this thesis are in the intermediate and mushroom regime. It is also interesting to explore the limits of applicability of the mean field approximation, via detailed comparison with experiment.

Chapter 3 provides quantitative and qualitative descriptions of the polymer brush in a good solvent and formed by selective adsorption of one block of copolymer. The thickness of the brush, the maximum polymer concentration, the location of the maximum, the depletion layer, and the dependence of these properties on surface density and molecular weight are discussed. The results are compared in detail with the recent experiments of Kent *et al.* [1, 2] performed on poly(dimethylsiloxane-*block*-styrene) copolymer spread as a monolayer at the free surface of ethylbenzonate. They are also analyzed in terms of the scaling [7, 11, 28], and analytic SCF theories [29, 106]. The results presented in this chapter have appeared in a previously published article [107]. The structure of the brush in Θ solvent is also analyzed and compared with the predictions of the analytic theories.

Chapter 4 deals with the compression of a polymer brush in good and Θ solvents. Three modes of compression are considered. The first is the compression of a polymer brush by a second identical brush; the second corresponds to compression of the polymer brush by a bare repulsive surface; and, finally, the third mode is the compression of the brush by a surface which is neutral for adsorption. These model calculations are directly compared with analytic theories of polymer brushes under different solvent conditions. The density profiles, as well as the free energy under compression, are calculated for each type of deformation and the results are presented in terms of effective power laws and universal functions of the simple measure of the degree of compression of a brush. The questions raised there address the problem of equivalence of different modes of the compression and the interpenetration of polymer brushes. The range of force and its magnitude is also of interest in this chapter.

The lateral compression of the polymer layers is the subject of chapter 5. First. a homopolymer/poor solvent system with an attractive surface interaction is considered. The surface pressure as a function of coverage is calculated. Then. a copolymer/solvent system is considered in which the anchoring block is the same as the homopolymer and the solvent is good for the dangling block. Both blocks are incorporated within the self-consistent formalism. The excess surface pressure. defined as a difference between the surface pressure for the diblock copolymer system and the system when only homopolymer is present, is calculated and compared with the rapid rise observed in recent experimental work [2]. Interesting questions raised in that chapter are about the steric effects in the adsorbed polymer layers and the equilibrium of the system under consideration.

Chapter 6 summarizes and concludes with some general comments on the results drawn from all studies presented in this dissertation.

Chapter 2

Numerical Self-Consistent Field Theory

2.1 Introductory Remarks

In the following section the general self-consistent theory for polymer/solvent systems near surfaces will be discussed. The formalism presented here was introduced by Hong and Noolandi [108-110] , and Helfand and coworkers [111-113], and developed by Ohta and Kawasaki [114], Whitmore and Noolandi [115, 64], as well as by Banaszak [116] and is based on the SCF theory of Edwards and Dolan [21, 22, 117].

As discussed in section 1.4, the statistical mechanical description of a polymer system proceeds in three steps. In order to characterize the various microscopic configurations of the system, models for linear flexible polymer chains and the interactions between segments within the chain are needed. The interactions are divided into two parts. The interactions among the polymer segments limited to within a few neighbors along the chain, are usually called "short range interactions", and those between the segments which are far apart along the chain are referred to as "long range", or solvent mediated, effective monomer-monomer interactions [24, 32, 118]. The conditions under which the effective, "two body", long range interactions vanish define the Θ point at which the chain is considered as an "ideal polymer" [32]. The Θ point can be also defined considering a dilute solution of polymer chains in a solvent. The osmotic pressure can be expressed in the form of a virial expansion

$$\Pi_{\text{osmotic}} = N_A k_B T c_p \left(A_1 + A_2 c_p + A_3 c_p^2 + \cdots \right) , \tag{2.1}$$

where N_A is the Avogadro number, c_p is the polymer concentration and the A_i are the virial coefficients. A_2 is called the second virial coefficient or excluded volume parameter. For the polymer/solvent system, $A_2 = 0$ defines the Θ solvent.

The simplest quantity which characterizes the spatial size of a polymer chain is the root-mean-squared (rms) end-to-end distance. Microscopically different models of polymer chains produce the same general universal description in terms of the rms end-to-end distance [32]

$$< \boldsymbol{R}^2 > \sim Z . \tag{2.2}$$

If one introduces the effective bond length b [118] Eq. (2.2) becomes $< \boldsymbol{R}^2 > = Zb^2$. In addition to $< \boldsymbol{R}^2 >$ of the chain, there is a more specific quantity describing the chain. This is $\Psi_Z(\boldsymbol{R})$, the probability distribution function that the end-to-end vector of Z segments equals $\boldsymbol{R}$. For the freely jointed and freely rotating chain models [32], as well as for other ideal chain models in which the orientational correlations diminish rapidly with distance, $\Psi_Z(\boldsymbol{R})$ has a Gaussian distribution for $Z \gg 1$. Furthermore, the local structure of the chain appears in these models only through the effective bond length b. The simplest model which satisfies these criteria but is still very useful and powerful, is a Gaussian chain. The Gaussian chain is defined as a chain in which every bond has a Gaussian distribution, $\psi(\boldsymbol{r})$, and

$$\psi(\boldsymbol{r}) = \left(\frac{3}{2\pi b^2}\right)^{3/2} \exp\left(-\frac{3\boldsymbol{r}^2}{2b^2}\right) . \tag{2.3}$$

so that the mean squared bond length is

$$< \boldsymbol{r}^2 >= b^2 . \tag{2.4}$$

The effective bond length b is referred to as the statistical segment length. The other quantity of interest here is the probability that a chain consisting of Z segments will follow a particular spatial conformation, $\Psi(\boldsymbol{r}_0, \boldsymbol{r}_1, \ldots, \boldsymbol{r}_{Z-1}) \equiv \Psi_Z\{\boldsymbol{r}_\tau\}$. $\Psi_Z\{\boldsymbol{r}_\tau\}$ is conditioned by "linear memory" and can be written as

$$\Psi_Z\{\boldsymbol{r}_\tau\} = \prod_{k=0}^{Z-1} \psi(\boldsymbol{r}_{k-1} - \boldsymbol{r}_k) . \tag{2.5}$$

An important property of the Gaussian chain is that the distribution of the vector $\boldsymbol{r}_k - \boldsymbol{r}_j$ between any two units k and j is Gaussian [118]. Hence, the flexible polymer chain, without loss of generality, can be modeled via *an equivalent Gaussian chain* [32], which has n segments and the same rms end-to-end distance as for the real macromolecule. The segment length in the equivalent chain, denoted Δs, is chosen such that

$$n\Delta s = Zb , \tag{2.6}$$

where Z is the degree of polymerization of the molecule, and $< \boldsymbol{R}^2 >= Zb^2$. Using

Eq. (2.3), the probability distribution for any link can be written as

$$\psi(\boldsymbol{r}) = \left(\frac{3}{2\pi b\Delta s}\right)^{3/2} \exp\left(-\frac{3\boldsymbol{r}^2}{2b\Delta s}\right) . \tag{2.7}$$

It is convenient to consider a polymer chain whose two terminal segments are fixed in space. The chain's segments are indexed from 0 to n. This situation is schematically presented in figure 2.1. The probability distribution function that the chain starts at position $\boldsymbol{r}_0$ and ends at $\boldsymbol{r}_n$ is called the Green's function of the polymer chain, or the chain "propagator". For the equivalent Gaussian chain, it can be expressed as

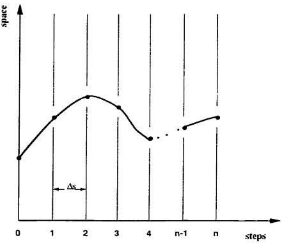

Figure 2.1: Polymer chain configuration which starts at position $\boldsymbol{r}_0$ and after n steps ends at $\boldsymbol{r}_n$, with the intermediate positions specified by $\{r_k\}$

$$Q(\boldsymbol{r}_n, n|\boldsymbol{r}_0, 0) \equiv \int \Psi_n\{\boldsymbol{r}'_\tau\}\delta(\boldsymbol{r}'_0 - \boldsymbol{r}_0)\delta(\boldsymbol{r}'_n - \boldsymbol{r}_n) \prod_{k=0}^{n} d\boldsymbol{r}'_k \tag{2.8}$$

$$= \left(\frac{3}{2\pi b\Delta s}\right)^{3n/2} \int \exp\left[-\frac{3}{2b}\sum_{k=0}^{n}\frac{(\boldsymbol{r}'_{k+1} - \boldsymbol{r}'_k)^2}{\Delta s}\right] \delta(\boldsymbol{r}'_0 - \boldsymbol{r}_0)\delta(\boldsymbol{r}'_n - \boldsymbol{r}_n) \prod_{k=0}^{n} d\boldsymbol{r}'_k .$$

In the limit that $n \to \infty$ and $\Delta s \to 0$ so that Eq. (2.6) is satisfied, one can pass to the continuous limit [119, 120] which defines the *Wiener Measure*

$$P[\boldsymbol{r}(\cdot)] \propto \exp\left[-\frac{3}{2b^2}\int_0^Z d\tau \left|\frac{d\boldsymbol{r}(\tau)}{d\tau}\right|^2\right] , \tag{2.9}$$

and the polymer chain is modeled as a space curve $\boldsymbol{r}(\tau)$ with τ varying from 0 to Z. The Green's function or chain propagator becomes

$$Q(\boldsymbol{r}_Z, Z|\boldsymbol{r}_0, 0) = \int \delta\boldsymbol{r}(\cdot)\, \delta(\boldsymbol{r}(0) - \boldsymbol{r}_0)\delta(\boldsymbol{r}(Z) - \boldsymbol{r}_Z)P[\boldsymbol{r}(\cdot)] , \tag{2.10}$$

and it can be shown that it satisfies the ordinary diffusion equation

$$\frac{b^2}{6}\nabla^2 Q(\boldsymbol{r}, \tau|\boldsymbol{r}', 0) = \frac{\partial}{\partial\tau}Q(\boldsymbol{r}, \tau|\boldsymbol{r}', 0) \tag{2.11}$$

with the initial conditions

$$Q(\boldsymbol{r}, 0|\boldsymbol{r}', 0) = \delta(\boldsymbol{r} - \boldsymbol{r}') . \tag{2.12}$$

The more rigorous definition of the Wiener Measure and the correspondence of the Wiener integral, Eq. (2.10), to the diffusion and Schrödinger equations can be found in Refs. [119, 121, 122] and references therein.

2.2 Partition Function

In this section the general theory for the diblock copolymer spread as a monolayer at the air-liquid interface will be introduced. The modifications and simplifications of this formalism for the analysis of the properties of the dangling block only will be discussed in the chapter 3. The details of the formalism for compression of a polymer brush by two kinds of surfaces and by a second identical brush will be discussed in detail in chapter 4. Finally the details of the theory and simplifications to the case of a homopolymer spread as a monolayer will be presented in the chapter 5.

The system under investigation can be described by $\tilde{N}_C$ diblock copolymer chains and $\tilde{N}_S$ solvent molecules in some volume $\boldsymbol{\Omega}$. The interface is located at $x = 0$. and is characterized by its total area. $\mathcal{A}$. A diblock copolymer consists of a block A. characterized by its degree of polymerization. Z_A. statistical segment length. b_A. and the density of pure material, ρ_{0A}. in monomers per unit volume. Similarly. block B can be characterized by Z_B, b_B, and ρ_{0B}. For solvent molecules. the density of pure material, ρ_{0S}. has to be specified. Since the system consists of $\tilde{N}_C$ chains the total number of monomers of type κ is $N_\kappa = \tilde{N}_C Z_\kappa$. $\kappa = A, B$

It is useful to introduce at this point the concept of conservation of volume on mixing. The condition of no volume change associated with mixing is equivalent to the local volume fractions adding up to unity everywhere

$$\sum_\kappa \frac{< \hat{\rho}_\kappa(\boldsymbol{r}) >}{\rho_{0\kappa}} = 1 \ . \tag{2.13}$$

where $\hat{\rho}_\kappa(\boldsymbol{r})$ is the local density of species κ for a given configuration. and $< \ldots >$ denotes the ensemble average. Equation (2.13) is often referred to as incompressibility condition [108].

Having the model for the polymer chains and assuming that there is no volume change upon mixing, the configurational partition function can be written using functional integrals over all possible chain configurations and locations of solvent molecules

$$
\begin{aligned}
\boldsymbol{Z} \;=\; & \left(\prod_{\kappa=C,S} \frac{\mathcal{Z}_{\kappa}^{\tilde{N}_{\kappa}}}{\tilde{N}_{\kappa}!} \right) \int (\prod_{i=1}^{\tilde{N}_S} d\boldsymbol{r}_{Si}) \times \\
& \int \prod_{j}^{\tilde{N}_C} \delta \boldsymbol{r}_{Aj}(\cdot) P[\boldsymbol{r}_{Aj}(\cdot)] \mathcal{G}(\boldsymbol{r}_{Aj}(0))\, \delta \boldsymbol{r}_{Bj}(\cdot) P[\boldsymbol{r}_{Bj}(\cdot)] \times \\
& \delta \left(\boldsymbol{r}_{Bj}(Z_B) - \boldsymbol{r}_{Aj}(Z_A) \right) \times \\
& \prod_{\boldsymbol{r}} \delta \left(1 - \sum_{\kappa=A,B,S} \frac{\hat{\rho}_{\kappa}(\boldsymbol{r})}{\rho_{0\kappa}} \right) \times \\
& \exp \left[-\beta \hat{V} \right] .
\end{aligned}
\tag{2.14}
$$

In this expression $P[\boldsymbol{r}_{\kappa j}(\cdot)]$ denotes any configuration of the $j-th$ chain of type κ. $\delta \boldsymbol{r}_{\kappa j}(\cdot)$ denotes the Wiener Measure, and the kinetic contribution of the solvent molecule or polymer chain is denoted by $\mathcal{Z}_{\kappa}$. The function $\mathcal{G}(\boldsymbol{r}_{Aj}(0))$ is introduced here for the convenience. It describes the a priori probability distribution for the free end of a A type chain. In most cases, it is simply $\mathcal{G} = 1$ everywhere. However, in those cases where, for physical reasons, the chain is localized to a particular interfacial region, it is convenient to use $\mathcal{G}(\boldsymbol{r}_{Aj}(0))$ in the form

$$
\begin{aligned}
\mathcal{G}(\boldsymbol{r}_j(0)) = 0 \text{ if } \boldsymbol{r}_j(0) \notin \text{ interface} \\
0 < \mathcal{G}(\boldsymbol{r}_j(0)) \leq 1 \text{ if } \boldsymbol{r}_j(0) \in \text{ interface}
\end{aligned}
\quad . \tag{2.15}
$$

Thus from all possible conformations of chains, only these which have the A type end of every chain in the interface contribute. This explicit form is used only in the calculations of chapter 5 of this thesis. $\delta(\boldsymbol{r}_{Bj}(Z_B) - \boldsymbol{r}_{Aj}(Z_A))$ assures the connectivity of A and B blocks and the condition that there is no local volume change on mixing is imposed by the expression $\delta(1-\sum\frac{\hat{\rho}_{\kappa}(\boldsymbol{r})}{\rho_{0\kappa}})$ [114]. The potential $\beta\hat{V}$ which appears in Eq. (2.14) is due to the interactions between all components present in the system and interactions with the boundaries. It is a function of the microscopic particle densities which are modeled as

$$\hat{\rho}_S(\boldsymbol{r}) = \sum_{i=1}^{\tilde{N}_S} \delta(\boldsymbol{r}-\boldsymbol{r}_{Si}) \tag{2.16}$$

$$\hat{\rho}_\kappa(\boldsymbol{r}) = \sum_{j=1}^{\tilde{N}_C} \int_0^{Z_\kappa} d\tau\, \delta(\boldsymbol{r}-\boldsymbol{r}_{\kappa j}(\tau)) \;. \tag{2.17}$$

where $\boldsymbol{r}_{\kappa j}(\tau)$ describes the position of monomer τ of type κ in j chain.

In general the interactions between all molecules present in the system are not pairwise additive. However in most of the theoretical models in which the chains are modeled as the equivalent Gaussian chains it is assumed that the binary interactions are sufficient to describe the real polymers in a solution [32]. The two-body interaction potential can be written

$$\begin{aligned} \beta\hat{V} \equiv \hat{W} &= \frac{1}{2}\sum_{\kappa\kappa'=A,B,S} \int d\boldsymbol{r} \int d\boldsymbol{r}' \hat{\rho}_\kappa(\boldsymbol{r}) W_{\kappa\kappa'}(\boldsymbol{r}-\boldsymbol{r}')\hat{\rho}_{\kappa'}(\boldsymbol{r}') + \\ &\sum_{\kappa=A,B,S} \int d\boldsymbol{r} \hat{\rho}_\kappa(\boldsymbol{r}) u_\kappa(\boldsymbol{r}) \;. \end{aligned} \tag{2.18}$$

where $W_{\kappa\kappa'}(\boldsymbol{r}-\boldsymbol{r}')$ defines the potential acting on a particle of type κ at the position $\boldsymbol{r}$ due to a particle of type κ' at the position $\boldsymbol{r}'$, and $u_\kappa(\boldsymbol{r})$ is the potential experienced by component κ due to the surface.

Equations (2.16) and (2.17) express the microscopic particle densities in terms of the individual solvent molecules and chain segments. Since the polymer chains are modeled by continuous Gaussian chains it is essential to transform the microscopic, point-like densities to continuous functions. This can be done through the introduction, for each independent function $\hat{\rho}_\kappa(\boldsymbol{r})$, of a Dirac delta function

$$\prod_{\boldsymbol{r}} \delta\left(1 - \sum_{\kappa=A,B,S} \frac{\hat{\rho}_\kappa(\boldsymbol{r})}{\rho_{0\kappa}}\right) \exp\left[-\hat{W}\right] = \tag{2.19}$$
$$\int \left\{ \prod_{\kappa=A,B,S} \delta\rho_\kappa(\cdot)\delta\left[\rho_\kappa(\cdot) - \hat{\rho}_\kappa(\cdot)\right] \right\} \prod_{\boldsymbol{r}} \delta\left(1 - \sum_{\kappa=A,B,S} \frac{\rho_\kappa(\boldsymbol{r})}{\rho_{0\kappa}}\right) \exp\left[-W(\{\rho_\kappa(\cdot)\})\right] .$$

where $W(\{\rho_\kappa(\cdot)\})$ is defined as in Eq. (2.18) but for continuous $\{\rho_\kappa(\boldsymbol{r})\}$. The physical meaning of the Eq. (2.19) is that with every conformation of the polymer/solvent system there is associated a set of smooth functions which describes the distribution of $\tilde{N}_C$ diblock copolymer chains and $\tilde{N}_S$ solvent molecules present in the system. The next step is the use of the Fourier transform for each Dirac delta function.

$$\delta\left[\rho_\kappa(\cdot) - \hat{\rho}_\kappa(\cdot)\right] = \mathcal{N}_1 \int \delta\omega_\kappa(\cdot) \exp\left[\int d\boldsymbol{r}\omega_\kappa(\boldsymbol{r})[\rho_\kappa(\boldsymbol{r}) - \hat{\rho}_\kappa(\boldsymbol{r})]\right] . \tag{2.20}$$

and

$$\prod_{\boldsymbol{r}} \delta\left(1 - \sum_\kappa \frac{\rho_\kappa(\boldsymbol{r})}{\rho_{0\kappa}}\right) = \mathcal{N}_2 \int \delta\eta(\cdot) \exp\left[\int d\boldsymbol{r}\eta(\boldsymbol{r})\left(1 - \sum_\kappa \frac{\rho_\kappa(\boldsymbol{r})}{\rho_{0\kappa}}\right)\right] . \tag{2.21}$$

where the limits of integration for the fields $\omega_\kappa(\cdot)$ and $\eta(\cdot)$ are $\pm i\infty$.

Transformations of the microscopic densities into continuous functions $\rho_k(\cdot)$, and introduction of the integral representation of the δ functionals leads to the following form of the partition function [115, 116]:

$$\boldsymbol{Z} = \left(\prod_{\kappa=C,S} \frac{\mathcal{Z}_\kappa^{\tilde{N}_\kappa}}{\tilde{N}_\kappa!}\right) \times \int \left[\prod_{\kappa=A,B,S} [\delta\rho_\kappa(\cdot)\delta\omega_\kappa(\cdot)\right] \delta\eta(\cdot) \times$$

$$\left(\prod_{\kappa=C,S} \mathcal{Q}_{\kappa}^{\tilde{N}_{\kappa}}\right) \times \exp\left[\int d\boldsymbol{r}\ \eta(\boldsymbol{r})(1-\sum_{k=A,B,S}\frac{\rho_k(\boldsymbol{r})}{\rho_{0k}})\right] \times \qquad (2.22)$$
$$\exp\left[\sum_{k=A,B,S}\int d\boldsymbol{r}\ \omega_k(\boldsymbol{r})\rho_k(\boldsymbol{r})\right] \times \exp\left[-W[\{\rho_k(\cdot)\}]\right] .$$

where, for solvent

$$\mathcal{Q}_S = \int d\boldsymbol{r}\ \exp[-\omega_S(\boldsymbol{r})] , \qquad (2.23)$$

and for copolymer

$$\begin{aligned} \mathcal{Q}_C &= \int \delta\boldsymbol{r}_A(\cdot)\delta\boldsymbol{r}_B(\cdot)P[\boldsymbol{r}_A(\cdot)]P[\boldsymbol{r}_B(\cdot)]\mathcal{G}(\boldsymbol{r}_A(0)) \times \\ &\exp\left[-\int_0^{Z_A} d\tau\ \omega_A[\boldsymbol{r}(\tau)]\right]\exp\left[-\int_0^{Z_B} d\tau\ \omega_B[\boldsymbol{r}(\tau)]\right] \times \qquad (2.24) \\ &\delta(\boldsymbol{r}_B(Z_B)-\boldsymbol{r}_A(Z_A)) . \end{aligned}$$

One can introduce, in a similar way as in Eq. (2.11), the propagators

$$\begin{aligned} \boldsymbol{Q}_{\kappa}(\boldsymbol{r},\tau|\boldsymbol{r}',0) &= \int \delta\boldsymbol{r}_{\kappa}(\cdot)\delta[\boldsymbol{r}_{\kappa}(\tau)-\boldsymbol{r}]\delta[\boldsymbol{r}_{\kappa}(0)-\boldsymbol{r}'] \times \\ &\exp\left\{-\int_0^{\tau} d\tau'\ \left(\frac{3}{2b_{\kappa}^2}\left|\frac{d\boldsymbol{r}(\tau)}{d\tau}\right|^2+\omega_{\kappa}[\boldsymbol{r}_{\kappa}(\tau')]\right)\right\} . \qquad (2.25) \end{aligned}$$

which satisfy the modified diffusion equation [32]

$$\left[\frac{b_{\kappa}^2}{6}\boldsymbol{\nabla}^2-\omega_{\kappa}(\boldsymbol{r})\right]\boldsymbol{Q}_{\kappa}(\boldsymbol{r},\tau|\boldsymbol{r}',0)=\frac{\partial}{\partial\tau}\boldsymbol{Q}_{\kappa}(\boldsymbol{r},\tau|\boldsymbol{r}',0) . \qquad (2.26)$$

with the initial condition given by Eq. (2.12). With these assumptions the integral of the distribution function, Eq. (2.24) can be written as

$$\mathcal{Q}_C = \int d\boldsymbol{r}\, d\boldsymbol{r}'\, d\boldsymbol{r}''\boldsymbol{Q}_B(\boldsymbol{r},Z_B|\boldsymbol{r}',0)\boldsymbol{Q}_A(\boldsymbol{r},Z_A|\boldsymbol{r}'',0)\mathcal{G}(\boldsymbol{r}''(0)) . \qquad (2.27)$$

Finally, using the Stirling approximation, the partition function can be written as

$$\boldsymbol{Z} = \mathcal{N} \int \prod_{\kappa=A,B,S} \delta\rho_\kappa(\cdot)\delta\omega_\kappa(\cdot)\delta\eta(\cdot) \exp\left[-\mathcal{F}_T[\{\rho_\kappa(\cdot)\},\{\omega_\kappa(\cdot)\},\eta(\cdot)]\right] , \tag{2.28}$$

where $\mathcal{F}_T[\{\rho_\kappa(\cdot)\},\{\omega_\kappa(\cdot)\},\eta(\cdot)]$ is the free energy functional given by

$$\mathcal{F}_T[\{\rho_\kappa(\cdot)\},\{\omega_\kappa(\cdot)\},\eta(\cdot)] = F[\{\rho_\kappa(\cdot)\},\{\omega_\kappa(\cdot)\}] + G[\{\rho_\kappa(\cdot)\},\eta(\cdot)] , \tag{2.29}$$

with

$$\begin{aligned} F[\{\rho_\kappa(\cdot)\},\{\omega_\kappa(\cdot)\}] &= \left[W[\{\rho_\kappa(\cdot)\}] - \sum_{\kappa=A,B,S} \int d\boldsymbol{r}\; \omega_\kappa(\boldsymbol{r})\rho_\kappa(\boldsymbol{r})\right] + \\ &\quad \sum_{\kappa=C,S} \tilde{N}_\kappa \left\{\ln \frac{\tilde{N}_\kappa}{\mathcal{Z}_\kappa \mathcal{Q}_\kappa} - 1\right\} & (2.30) \\ G[\{\rho_\kappa(\cdot)\},\eta(\cdot)] &= \int d\boldsymbol{r}\; \eta(\boldsymbol{r}) \left[\sum_{\kappa=A,B,S} \frac{\rho_\kappa(\boldsymbol{r})}{\rho_{0\kappa}} - 1\right] . & (2.31) \end{aligned}$$

To complete the presentation, the expressions for the average density distribution of each component are needed. Using the partition function Eq. (2.14), the density of component κ can be expressed as

$$\begin{aligned} \langle\hat{\rho}_\kappa(\boldsymbol{r})\rangle &= \frac{1}{\boldsymbol{Z}} \left(\prod_{\kappa=C,S} \frac{\mathcal{Z}_\kappa^{\tilde{N}_\kappa}}{\tilde{N}_\kappa!}\right) \int (\prod_{i=1}^{\tilde{N}_S} d\boldsymbol{r}_{Si}) \times \\ &\quad \int \prod_j^{\tilde{N}_C} \delta\boldsymbol{r}_{Aj}(\cdot) P[\boldsymbol{r}_{Aj}(\cdot)] \mathcal{G}(\boldsymbol{r}_{Aj}(0))\, \delta\boldsymbol{r}_{Bj}(\cdot) P[\boldsymbol{r}_{Bj}(\cdot)] \times & (2.32) \\ &\quad \delta\left(\boldsymbol{r}_{Bj}(Z_B) - \boldsymbol{r}_{Aj}(Z_A)\right) \times \\ &\quad \hat{\rho}_\kappa(\boldsymbol{r}) \times \\ &\quad \prod_{\boldsymbol{r}} \delta\left(1 - \sum_{\kappa=A,B,S} \frac{\hat{\rho}_\kappa(\boldsymbol{r})}{\rho_{0\kappa}}\right) \times \\ &\quad \exp\left[-\beta\hat{V}\right] . \end{aligned}$$

Performing the same transformations of variables for this expression as were done for the partition function, it can be shown [116] that, for solvent, the density is

$$\begin{aligned}\langle\hat{\rho}_S(\boldsymbol{r})\rangle &= \frac{\mathcal{N}}{\boldsymbol{Z}}\int[\prod_{\kappa=A,B,S}\delta\rho_\kappa(\cdot)\delta\omega_\kappa(\cdot)]\delta\eta(\cdot)\frac{\bar{N}_S}{\mathcal{Q}_S}\frac{\delta\mathcal{Q}_S}{\delta\omega_S(\boldsymbol{r})} \\ &\quad \exp\left[-\mathcal{F}_T[\{\rho_\kappa(\cdot)\},\{\omega_\kappa(\cdot)\},\eta(\cdot)]\right] . \end{aligned} \tag{2.33}$$

and for each block of copolymer ($\kappa = A, B$)

$$\begin{aligned}\langle\hat{\rho}_\kappa(\boldsymbol{r})\rangle &= \frac{\mathcal{N}}{\boldsymbol{Z}}\int[\prod_{\kappa'=A,B,S}\delta\rho_{\kappa'}(\cdot)\delta\omega_{\kappa'}(\cdot)]\delta\eta(\cdot)\frac{\bar{N}_C}{\mathcal{Q}_C}\frac{\delta\mathcal{Q}_C}{\delta\omega_\kappa(\boldsymbol{r})} \\ &\quad \exp\left[-\mathcal{F}_T[\{\rho_{\kappa'}(\cdot)\},\{\omega_{\kappa'}(\cdot)\},\eta(\cdot)]\right] . \end{aligned} \tag{2.34}$$

2.3 Mean Field Approximation

To obtain the free energy of the system and the spatial distribution of the densities, one has to evaluate Eqs. (2.28), (2.33), and (2.34). Since the equilibrium state is the state with the minimum of free energy, these functionals can be approximated by the saddle point technique [123, 124]. Let the corresponding fields which minimize the free energy functional, or in other words contribute the most to the partition function, be denoted by $\rho_\kappa^0(\cdot)$. Then the free energy, partition function and density distributions reduce to

$$\mathcal{F}_T \rightarrow \mathcal{F}_T[\{\rho_\kappa^0(\cdot)\},\{\omega_\kappa^0(\cdot)\},\eta^0(\cdot)] \tag{2.35}$$

$$\boldsymbol{Z} \rightarrow \boldsymbol{Z}^0 \propto \exp\{-\mathcal{F}_T[\{\rho_\kappa^0(\cdot)\},\{\omega_\kappa^0(\cdot)\},\eta^0(\cdot)]\} \tag{2.36}$$

$$\langle\hat{\rho}_S(\boldsymbol{r})\rangle \rightarrow -\frac{\bar{N}_S}{\mathcal{Q}_S}\frac{\delta\mathcal{Q}_S}{\delta\omega_S(\boldsymbol{r})}\bigg|_0 \tag{2.37}$$

$$\langle \hat{\rho}_\kappa(\boldsymbol{r}) \rangle \quad \rightarrow \quad -\frac{\tilde{N}_C}{\mathcal{Q}_C} \frac{\delta \mathcal{Q}_C}{\delta \omega_\kappa(\boldsymbol{r})}\bigg|_0 \qquad \kappa = A, B \; . \tag{2.38}$$

To find the saddle point, $\mathcal{F}_\mathcal{T}$ has to be minimized with respect to each $\rho_\kappa(\boldsymbol{r})$, $\omega_\kappa(\boldsymbol{r})$ and $\eta(\boldsymbol{r})$ subject to the constraint of conservation of particle number for each component in the system

$$\int d\boldsymbol{r} \langle \rho_\kappa(\boldsymbol{r}) \rangle = N_\kappa \quad \kappa = S, A, B \; , \tag{2.39}$$

where for solvent $\tilde{N}_S = N_S$, $\tilde{N}_A = N_C Z_A$ for the A block, and $\tilde{N}_B = N_C Z_B$ for the B block. Proceeding with the minimization, the only part of $\mathcal{F}_\mathcal{T}$ which depends on the field $\eta(\boldsymbol{r})$, is G and this minimization gives

$$\sum_{\kappa=A,B,S} \frac{\rho_\kappa^0(\boldsymbol{r})}{\rho_{0\kappa}} = 1 \; , \tag{2.40}$$

and hence

$$G = 0 \; . \tag{2.41}$$

so that

$$\mathcal{F}_\mathcal{T}^0 = F^0 \; . \tag{2.42}$$

Minimization with respect to to the field $\omega_\kappa(\boldsymbol{r})$ yields

$$\rho_\kappa^0(\boldsymbol{r}) + \frac{\tilde{N}_\kappa}{\mathcal{Q}_\kappa} \frac{\delta \mathcal{Q}_\kappa}{\delta \omega_\kappa(\boldsymbol{r})} = 0 \; . \tag{2.43}$$

Comparison of Eq. (2.43) with Eqs. (2.37) and (2.38) gives the very important result that the saddle point values of ${\rho^0}_\kappa(\boldsymbol{r})$, which are what can be calculated, are equal to the equilibrium density distributions $\langle \hat{\rho}_k(\boldsymbol{r}) \rangle$ in this approximation, and the constraint of Eq. (2.39) can be applied as

$$\int d\boldsymbol{r}\,\rho^0_\kappa(\boldsymbol{r}) = N_\kappa \quad \kappa = S, A, B\,. \tag{2.44}$$

Minimization gives a set of equations for every component, connecting the interaction energy, densities and self-consistent potentials

$$\begin{aligned} \rho_\kappa(\boldsymbol{r}) + \frac{\bar{N}_\kappa}{\mathcal{Q}_\kappa}\frac{\delta \mathcal{Q}_\kappa}{\delta\omega_\kappa(\boldsymbol{r})} &= 0\,, & (2.45)\\ \frac{\delta W}{\delta\rho_\kappa(\boldsymbol{r})} - \omega_\kappa(\boldsymbol{r}) + \frac{\eta(\boldsymbol{r})}{\rho_{0\kappa}} - \lambda_\kappa &= 0\,, & (2.46) \end{aligned}$$

where λ_κ are the Lagrange multipliers associated with Eq. (2.44), and the superscripts can be dropped. Equations (2.45) and (2.23) yield

$$\rho_S(\boldsymbol{r}) = \frac{\bar{N}_S}{\mathcal{Q}_S}\exp[-\omega_S(\boldsymbol{r})]\,. \tag{2.47}$$

In order to obtain expressions for the densities of each block, the functional derivatives $\frac{\delta\mathcal{Q}_C}{\delta\omega_A(\boldsymbol{r})}$ and $\frac{\delta\mathcal{Q}_C}{\delta\omega_B(\boldsymbol{r})}$ have to be evaluated. Following the derivation presented in Ref. [116], it can be shown that

$$\begin{aligned} \rho_A(\boldsymbol{r}) \;=\; & \frac{\bar{N}_C}{\mathcal{Q}_C}\int_0^{Z_A} d\tau \left\{ \int d\boldsymbol{r}'\,d\boldsymbol{r}''\,d\boldsymbol{r}'''\boldsymbol{Q}_A(\boldsymbol{r},\tau|\boldsymbol{r}',0)\mathcal{G}(\boldsymbol{r}') \right.\\ & \left. \boldsymbol{Q}_A(\boldsymbol{r}'',(Z_A-\tau)|\boldsymbol{r},\tau)\boldsymbol{Q}_B(\boldsymbol{r}'',Z_B|\boldsymbol{r}''',0) \right\}\,. \end{aligned} \tag{2.48}$$

Similarly, the B-block density distribution is given by

$$\begin{aligned} \rho_B(\boldsymbol{r}) \;=\; & \frac{\bar{N}_C}{\mathcal{Q}_C}\int_0^{Z_B} d\tau \left\{ \int d\boldsymbol{r}'\,d\boldsymbol{r}''\,d\boldsymbol{r}'''\boldsymbol{Q}_A(\boldsymbol{r}'',Z_A|\boldsymbol{r}',0)\mathcal{G}(\boldsymbol{r}') \right.\\ & \left. \boldsymbol{Q}_B(\boldsymbol{r},\tau|\boldsymbol{r}'',0)\boldsymbol{Q}_B(\boldsymbol{r}''',(Z_B-\tau)|\boldsymbol{r},\tau) \right\}\,. \end{aligned} \tag{2.49}$$

The potential energy, Eq. (2.18), is very general. It is useful to express it in terms of Flory interaction parameters [24] and the volume fractions of the components. To do so, a symmetric form of the potential energy [108], which vanishes for interaction between like molecules, is introduced

$$U_{\kappa\kappa'}(\boldsymbol{r}) = W_{\kappa\kappa'}(\boldsymbol{r}) - \frac{1}{2}\left(W_{\kappa\kappa'}(\boldsymbol{r})\rho_{0\kappa}^2 + W_{\kappa\kappa'}(\boldsymbol{r})\rho_{0\kappa'}^2\right) . \tag{2.50}$$

Equation (2.18) can be written as

$$\begin{aligned} W &= \frac{1}{2}\sum_{\kappa=A,B,S} W_{\kappa\kappa'}\rho_{0\kappa}N_\kappa + \\ &\quad \frac{1}{2}\sum_{\kappa\kappa'}\int d\boldsymbol{r}\, d\boldsymbol{r}'\rho_\kappa(\boldsymbol{r})U_{\kappa\kappa'}(\boldsymbol{r}-\boldsymbol{r}')\rho_{\kappa'}(\boldsymbol{r}') + \\ &\quad \sum_{\kappa=A,B,S}\int d\boldsymbol{r}\rho_\kappa(\boldsymbol{r})u_\kappa(\boldsymbol{r}) . \end{aligned} \tag{2.51}$$

where

$$W_{\kappa\kappa'} = \int d\boldsymbol{r} W_{\kappa\kappa'}(\boldsymbol{r}) \tag{2.52}$$

and is measure of the overall strength of each interaction. Now assuming $U_{\kappa\kappa'}(\boldsymbol{r}-\boldsymbol{r}')$ to be of short range and performing a gradient expansion [108], the potential can be written in the following form

$$\begin{aligned} W &= \frac{1}{2}\sum_{\kappa=A,B,S} W_{\kappa\kappa}\rho_{0\kappa}N_\kappa + \\ &\quad \frac{1}{2}\rho_{ref}\sum_{\kappa\kappa'}\chi_{\kappa\kappa'}\int d\boldsymbol{r}\left(\phi_\kappa(\boldsymbol{r})\phi_{\kappa'}(\boldsymbol{r}) - \frac{\sigma^2}{6}\nabla\phi_\kappa(\boldsymbol{r})\nabla\phi_{\kappa'}(\boldsymbol{r})\right) + \\ &\quad \sum_{\kappa=A,B,S}\int d\boldsymbol{r}\rho_{0\kappa}\phi_\kappa(\boldsymbol{r})u_\kappa(\boldsymbol{r}) . \end{aligned} \tag{2.53}$$

Flory parameters [24] are defined as [116]

$$\chi_{\kappa\kappa'} = \frac{\rho_{0\kappa}\rho_{0\kappa'}}{\rho_{ref}}U_{\kappa\kappa'} . \tag{2.54}$$

where

$$U_{\kappa\kappa'} = \int d\boldsymbol{r} U_{\kappa\kappa'}(\boldsymbol{r}). \tag{2.55}$$

$$\sigma^2 = \frac{\int d\boldsymbol{r}|\boldsymbol{r}|^2 U_{\kappa\kappa'}(\boldsymbol{r})}{U_{kk'}} . \tag{2.56}$$

The reference density used to define Flory interaction parameters is usually taken to be the density of pure solvent present in the system, ρ_{0S}. The parameter σ is the effective range of the interaction and, in most calculations, is taken to be $\sigma^2 \simeq b^2$, where b is the average of the statistical segment lengths. $\phi_\kappa(\boldsymbol{r})$ is the local volume fraction and is defined as

$$\phi_\kappa(\boldsymbol{r}) \equiv \frac{\rho_\kappa(\boldsymbol{r})}{\rho_{0\kappa}} . \tag{2.57}$$

The self-consistent potentials can be evaluated through Eq. (2.46), using the expression for the potential energy, Eq. (2.53). The result is

$$\omega_\kappa(\boldsymbol{r}) = \frac{\eta(\boldsymbol{r})}{\rho_{0\kappa}} + \frac{\rho_{0S}}{2\rho_{0\kappa}} \sum_{\kappa'} \chi_{\kappa\kappa'} \left[\phi_{\kappa'}(\boldsymbol{r}) - \frac{\sigma^2}{6} \boldsymbol{\nabla}^2 \phi_{\kappa'}(\boldsymbol{r})\right] + \frac{1}{\rho_{0\kappa}} u_\kappa(\boldsymbol{r}) - \lambda_\kappa . \tag{2.58}$$

The field $\eta(\boldsymbol{r})$ and unknown Lagrange multipliers can be eliminated. To eliminate the Lagrange multipliers λ_κ, one can require that $\omega_\kappa(\boldsymbol{r}) = 0$ in a pure solvent region. Eq. (2.47) yields

$$\omega_S(\boldsymbol{r}) = \ln\left(\frac{N_S}{\mathcal{Q}_S \rho_S(\boldsymbol{r})}\right) . \tag{2.59}$$

Now, in a bulk phase, only solvent is present, $\rho_S^b = \rho_{0S}$ and the self-consistent potential for solvent has to be constant, which can be set zero. This in turn gives

$$\omega_S(\boldsymbol{r}) = \ln\left(\frac{1}{\phi_S(\boldsymbol{r})}\right) \tag{2.60}$$

Because of the incompressibility assumption, Eq. (2.40), only $\omega_A(\boldsymbol{r})$ and $\omega_B(\boldsymbol{r})$ are needed and the density distribution of the solvent can be obtain through

$$\phi_S(\boldsymbol{r}) = 1 - \phi_A(\boldsymbol{r}) - \phi_B(\boldsymbol{r}) \,. \tag{2.61}$$

Thus, Eq. (2.58) evaluated for solvent, and Eq. (2.59) are sufficient to determine the field $\eta(\boldsymbol{r})$.

Finally the free energy in the mean field approximation can be written as

$$\begin{aligned} F[\{\rho_\kappa(\cdot)\},\{\omega_\kappa(\cdot)\}] &= W[\{\rho_\kappa(\cdot)\}] - \sum_{\kappa=A,B,S} \int d\boldsymbol{r}\, \omega_\kappa(\boldsymbol{r})\rho_\kappa(\boldsymbol{r}) + \\ & \sum_{\kappa=C,S} \tilde{N}_\kappa \left\{ \ln \frac{\tilde{V}_\kappa}{\mathcal{Z}_\kappa \mathcal{Q}_\kappa} - 1 \right\} \,. \end{aligned} \tag{2.62}$$

where $W[\{\rho_\kappa(\cdot)\}]$ is given by Eq. (2.53).

The details of the calculations, as well as the model of the interactions with the surface, will be discussed in the following chapters.

2.4 Summary - Self Consistent Mean Field Theory

To summarize, the theoretical approach, presented above, is based on the following assumptions:

- Polymer chains in bulk are described by continuous Gaussian random walks [32, 118, 119].
- The local volume fractions of all components sum locally to unity everywhere. This condition is introduced assuming no volume change upon mixing; it is

equivalent to assuming incompressibility [108].

- Effective interactions between the components are two-body, can be expressed in terms of Flory parameters and a finite range of interactions which is on order of a statistical segment length of a polymer [24, 108].
- Mean field approximation - the density fluctuations about the most probable conformation are neglected.

These general assumptions result in equations for the density profiles of every component present in the system and a free energy expression written in terms of the densities and interaction parameters.

The profiles for both copolymer blocks are calculated using Eqs. (2.48) and (2.49), and the density distribution of solvent is determined using Eq. (2.61). To obtain the density distributions for copolymer, one has to solve the modified diffusion equation

$$\left[\frac{b_\kappa^2}{6}\boldsymbol{\nabla}^2 - \omega_\kappa(\boldsymbol{r})\right] \boldsymbol{Q}_\kappa(\boldsymbol{r}, \tau|\boldsymbol{r}', 0) = \frac{\partial}{\partial\tau}\boldsymbol{Q}_\kappa(\boldsymbol{r}, \tau|\boldsymbol{r}', 0) \ . \tag{2.63}$$

for the propagators $\boldsymbol{Q}_\kappa(\boldsymbol{r}, \tau|\boldsymbol{r}', 0)$ subject to geometry-dependent initial and boundary conditions. The potentials $\omega_\kappa(\boldsymbol{r})$ which modify the diffusion equations include enthalpic interactions between the molecules, written in terms of Flory parameters, as well as interactions with the surface and terms arising from the condition that there is no volume change upon mixing.

The problem has to be solved self-consistently. To solve the diffusion equations, potentials are needed which depend on the densities, and the densities are determined through solution of the diffusion equations.

Chapter 3

Properties of Uncompressed Polymer Brushes

3.1 Introduction

In this chapter the properties of polymer brushes in good and Θ solvents are investigated (the system is schematically presented in figure 1.1b). The brush height, general shape of the density profile, including depletion layer, location of the maximum and tail region are investigated. The free energy of the brush and its dependence on the degree of polymerization of the dangling block and surface concentration are also probed. One of the purposes of this chapter is to provide a quantitative comparison of the numerical, SCF theory with the experiments of Kent *et al.* [1, 2]. In these experiments the properties of the polymer brush in a good solvent were investigated. For this comparison comprehensive numerical calculations were performed. For the calculations, the statistical segment length of the dangling block, b, the densities of pure materials ρ_{0S} and ρ_{0B}, the degrees of polymerization, Z, and the surface coverages, Σ, were chosen to agree as closely as possible with the experimental values. To investigate the free energy of the brush in a good solvent and make a comparison of the numerical SCF theory with the analytic picture of MWC [29, 33], model calculations for a polymer brush in a good solvent were performed. Similarly, model calculations were performed in order to compare the properties of the polymer brush in a Θ solvent with the analytic pictures of Shim and Cates [40] and Zhulina *et al.* [42, 43]. Similar calculations to those presented in this chapter were performed by Whitmore and Noolandi [64], however in the work presented here more detailed analysis of the numerical results and comparison with the experimental data are presented. The free energy and its dependence on the degree of polymerization and surface coverage as well as the quality of the solvent are also probed.

3.2 Details of the Numerical SCF formalism

The experiments of Kent *et al.* [1, 2] were performed on poly(dimethylsiloxane-*block*-styrene) copolymer (PDMS-PS) spread as a monolayer at the free surface of ethyl benzoate (EB). In this system the PDMS (A-block) lies flat on top of the EB, with the PS (B-block) dangling into the EB which is a good solvent for PS. All the A-B joints lie in a very narrow interphase region of width a, estimated by Kent [1] to be on the order of 1 nm for all samples. For the calculations, therefore, it has been and assumed that all the joints are randomly distributed throughout this interphase of width $a = 1$ nm. As well, the system is assumed to be translationally invariant parallel to the surface, and the problem becomes one dimensional.

There are three density profiles to determine, for the solvent and for the A and B blocks. The surface, $x = 0$, is defined as the plane at which the solvent and B-block densities reach zero. The interphase is thus the layer through which the volume fraction of the solvent and B-block together, $\phi_B(x) + \phi_S(x)$, rises from zero to unity, and $\phi_A(x)$ falls from unity to zero. In this chapter the dangling, B-block is of prime interest, and the SCF theory is not used to determine the density of A-block. Instead, the volume fraction $\phi_A(x)$ is represented by a simple, standard form

$$\phi_A(x) = 1 - \tanh^2\left(\frac{x}{l}\right), \qquad x \geq 0 . \tag{3.1}$$

with the parameter l chosen so that $\phi_A(x)$ falls effectively to zero over the interphase width of 1 nm: it has been chosen $l^{-1} = 3\ \mathrm{nm}^{-1}$, so that $\phi_A = 0.01$ at $x = a = 1$ nm.

To determine the density of dangling B block it is useful to introduce the integral representation of the propagators given by Eq. (2.25), where the integration is performed over all starting positions [108]. The first propagator is defined as

$$q_0(\boldsymbol{r}, \tau) = q_0(x, \tau) = \int d\boldsymbol{r}'\, \boldsymbol{Q}_B(\boldsymbol{r}, \tau|\boldsymbol{r}', 0) . \tag{3.2}$$

and the second propagator is defined as

$$q_1(\boldsymbol{r}, \tau) = q_1(x, \tau) = \int d\boldsymbol{r}'\, d\boldsymbol{r}''\, \boldsymbol{Q}_A(\boldsymbol{r}'', Z_A|\boldsymbol{r}', 0)\mathcal{G}(\boldsymbol{r}')\boldsymbol{Q}_B(\boldsymbol{r}, \tau|\boldsymbol{r}'', 0) . \tag{3.3}$$

In this calculation, the role of the A-block is to anchor the dangling block to the interface, and there is no need to calculate $\boldsymbol{Q}_A$. Since the dependences on $\boldsymbol{r}$ and τ appear only in a single propagator $\boldsymbol{Q}_\kappa$, the propagators q_i also satisfy the diffusion equation

$$\left[-\frac{b^2}{6}\frac{\partial^2}{\partial x^2}+\omega(x)\right]q_i(x,\tau)=-\frac{1}{Z}\frac{\partial}{\partial t}q_i(x,\tau)\ . \tag{3.4}$$

with the variable τ having been mapped onto interval $[0,1]$. These propagators have a simple physical interpretation. The first, $q_0(x,\tau)$, is proportional to the probability that a B chain of length τ ends at x given that it starts somewhere in the system, while $q_1(x,\tau)$ is proportional to the probability that a B chain of length τ ends at x given that it starts in the interface.

In addition to satisfying the diffusion equation, the propagators satisfy appropriate boundary and initial conditions. Since $\phi_A(x)=0$ at the upper edge of the interphase region, one boundary condition is

$$q_i(0,\tau)=0\ . \tag{3.5}$$

As well, the chains can extend only a finite distance into the solvent, which implies

$$q_i(\infty,\tau)=0\ , \tag{3.6}$$

for the other boundary condition. In practice, this condition is applied at a finite distance, which is chosen to be large enough as to have no effect on the brush.

The initial condition for q_1 follows from the assumption that the A-B joints are randomly distributed throughout the interphase of width a. This implies

$$q_1(x,0)\ =\ \begin{cases}1, & 0<x\le a\\ 0, & x>a\ .\end{cases} \tag{3.7}$$

Since the free end of the dangling block is not localized, the initial condition for q_0 is

$$q_0(x, 0) = 1, \quad x > 0 . \tag{3.8}$$

With this choice of propagators, the integral of distribution function Eq. (2.27) becomes

$$Q = \int_0^\infty dx \, q_1(x, 1) , \tag{3.9}$$

and the density of the dangling B block, Eq. (2.49), can be written

$$\phi_B(x) = \frac{Z_B}{\Sigma \rho_{0B} Q} \int_0^1 d\tau q_1(x, \tau) q_0(x, Z - \tau) . \tag{3.10}$$

where the average area per grafted chain, Σ, was introduced. For large values of Σ the lateral averaging introduced in the one dimensional model causes the polymer-polymer interactions to be undercounted. Thus, if the average area per grafted chain is large and the chains are in the mushroom regime the model is not expected to be a good description of the real system.

The potential $\omega(x)$ which modifies the diffusion equation in a general form is given by Eq. (2.58), and includes enthalpic interactions and terms arising from the condition that there is no volume change upon mixing, Eq. (2.61). After determination of the field $\eta(r)$ and the Lagrange multiplier λ, $\omega(x)$ can be written for the one dimensional case as

$$\begin{aligned} \omega(x) \;=\; & \frac{\rho_{ref}}{\rho_{oB}} \left\{ \chi_{BS} \left[\phi_S(x) - \phi_S^b - (\phi_B(x) - \phi_B^b) + \frac{\sigma^2}{6} \nabla^2 (\varphi_S(x) - \phi_B(x)) \right] + \right. \\ & \left. (\chi_{AB} - \chi_{AS}) \left[\phi_A(x) - \phi_A^b + \frac{\sigma^2}{6} \nabla^2 \phi_A(x) \right] \right\} + \end{aligned} \tag{3.11}$$

$$\frac{\rho_{0S}}{\rho_{0B}} \ln \frac{\phi_S^b}{\phi_S(x)} + u_B(x) - \frac{\rho_{0S}}{\rho_{0B}} u_S(x) \ .$$

where an additive constant has been chosen so that $\omega(x) \to 0$ far away from the surface, where $\phi_S^b = 1$. Since the experiments suggested there was little evidence of any particular affinity of the B-block for the surface, both χ_{AB} and χ_{SA} should be positive and of comparable magnitude. For convenience, $\chi_{AB} = \chi_{SB}$ has been used. Similarly the effective external potential acting on the B-block of copolymer, $u_B(x) - [\rho_{0S}/\rho_{0B}]u_S(x)$, is negligible. With this choice, the potential can be written

$$\omega(x) = \frac{\rho_{0S}}{\rho_{0B}} \left\{ \ln \frac{1}{\phi_S(x)} + \chi_{SB} \left[\phi_S(x) - \phi_B(x) - 1 + \frac{\sigma^2}{6} \left(\phi_S''(x) - \phi_B''(x) \right) \right] \right\} . \quad (3.12)$$

where χ_{SB} has been defined using the solvent for the reference density. The parameter σ^2 characterizes the effective range of the interactions, and was chosen to be equal to b^2, where b is the statistical segment length of the B-block. The direct contact with the analytic SCF theory can be made by assuming that $\phi_B(x)$ is small everywhere and the gradient corrections can be neglected. Expanding the logarithm appearing in the expression for the potential, Eq. (3.12), and ignoring the cross terms of the form $\phi_A(x)\phi_B(x)$ because there is very little overlap of A and B polymer densities, the potential has the form

$$\begin{aligned} \omega(x) \ \simeq \ & \omega_0 + \frac{\rho_{0S}}{\rho_{0B}} \left\{ \ln \left(\frac{1}{1 - \phi_A(x)} \right) - \chi_{SB}\phi_A(x) + (1 - 2\chi)\phi_B(x) + \right. \\ & \left. \frac{1}{2}\phi_B(x)^2 + \ldots \right\} . \end{aligned} \quad (3.13)$$

This $\omega(x)$ diverges logarithmically at the surface, so the polymer density goes to zero there. The analytic SCF theory, which ignores the depletion region, does not have such terms in the potential and the density remains finite, in fact a maximum. Hence, to obtain the analytic limit, these terms are dropped from this expression. The width of the anchoring region is also set to zero. The resulting potential

$$\omega(x) \simeq \omega_0 + \frac{\rho_{0S}}{\rho_{0B}} \left\{ (1 - 2\chi_{SB})\phi_B(x) + \frac{1}{2}\phi_B(x)^2 + \ldots \right\} . \tag{3.14}$$

is equivalent to the analytic potential if $\rho_{0S}/\rho_{0B}(1 - 2\chi_{SB})$ is identified as a binary polymer-polymer interaction (excluded volume parameter).

Finally, to determine the density profile of the solvent, Eq. (2.61) is used and $\phi_S(x)$ at any point is given by

$$\phi_S(x) = 1 - \phi_A(x) - \phi_B(x) . \tag{3.15}$$

For a given system, which is specified by the values for a, Z, Σ, ρ_{0B}, ρ_{0A}, ρ_{0S}, b and χ_{SB}, a self-consistent solution has to be obtained for the problem specified by Eqs. (3.1) to (3.15). This is done via an iterative procedure discussed in more detail in Appendix A.

Typical density profiles of both blocks are shown in figure 3.1. For the A block, $\phi_A(x)$ decreases smoothly from unity at the surface to zero over the thickness of the interface region, according to Eq. (3.1). For the B block, $\phi_B(x)$ rises from zero at the surface to its maximum value ϕ_m, and then decreases smoothly to zero in the extended region. In all calculations, the maximum is located well beyond the point at which the density of the A-block vanishes, and so this initial region between the surface and the ϕ_m can be identified as a depletion layer. Throughout the main body

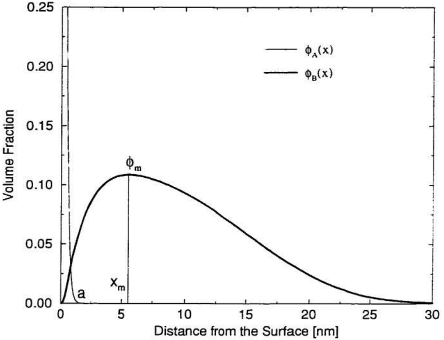

Figure 3.1: Calculated polymer profiles for the 10-40 PDMS-PS polymer at $\Sigma = 40$ nm^2, which corresponds to $\sigma^* = 3.2$. The profile of the PDMS block is represented by $\phi_A(x)$, which decreases from unity at the surface to zero over a distance of 1 nm, according to Eq. (3.1). All the PDMS-PS joints are located in this layer. The profile of the dangling PS block is represented by $\phi_B(x)$. Its maximum volume fraction, which is located at x_m, is denoted by ϕ_m.

of the profile, the density decreases monotonically, qualitatively as a parabola, and then evolves into an exponential-like tail near the tip.

The free energy of the brush is also of interest. To determine this quantity Eq. (2.62) is used. This expression however, contains some terms which are independent of the configuration of the system, as well as, the terms which can be attributed to the adsorbed A-block. Thus to calculate the free energy of the brush, these terms have to be subtracted from the Eq. (2.62). The result, expressed as the brush free energy per unit area, can be written

$$\begin{aligned}\frac{E_0}{\rho_{0S}k_BT} &= \int_0^\infty dx \left\{ \phi_S(x)\ln\phi_S(x) + \phi_B(x) - \chi\phi_B^2(x) - \frac{\rho_{0B}}{\rho_{0S}}\omega(x)\phi_B(x) \right\} \\ &\quad - \frac{1}{\Sigma\rho_{0S}}\ln Q\,. \end{aligned} \tag{3.16}$$

Each term appearing here can be interpreted physically. It can readily be shown that the calculated density distribution for the dangling block remains unchanged upon addition of a constant, ω^m, to the self-consistent potential of Eq. (3.12), so that one can set

$$\int_0^\infty dx\,\omega(x)\,\phi_B(x) = 0\,. \tag{3.17}$$

With this choice, the free energy per unit area can be written

$$\frac{E_0}{\rho_{0S}k_BT} = \int_0^\infty dx \left\{ \phi_S(x)\ln\phi_S(x) + \phi_B(x) - \chi\phi_B^2(x) \right\} - \frac{1}{\Sigma\rho_{0S}}\ln Q\,. \tag{3.18}$$

Using the incompressibility condition, the logarithmic term $\ln\phi_S(x)$ can be expanded in powers of $\phi_A(x) + \phi_B(x)$. Part of the result depends only on $\phi_A(x)$ which is subtracted from E_0 since, it is not the part of the brush energy. Neglecting terms due to the very small A-B overlap, the result can be written as

$$\frac{E(D)}{\rho_{0S}k_BT} = \int_0^\infty dx \left[\frac{1}{2}(1-2\chi)\phi_B^2(x) + \frac{1}{6}\phi_B^3(x)\right] - \frac{1}{\Sigma\rho_{0S}}\ln Q\,. \tag{3.19}$$

If the term with Q is interpreted as the elastic stretching, then the terms appearing in the integral are equivalent to the interaction energy in the mean field picture as was discussed in the Introduction, and Eq. (3.19) is the free energy of the brush.

3.3 Polymer Brush in a Good Solvent

In this section, numerical results for PDMS-PS at the EB/air interface are presented and analyzed. In order to make a comparison with the experimental data of Kent *et al.* [1, 2] calculations were performed for five polymers, with Z ranging from 280 to 3,100. For each Z, up to 22 different surface densities were examined. The overall range in Σ was from on the order of 10 to 1000 nm^2 per chain, corresponding to σ^* ranging from 0.4 to almost 12. These data are included in Table 3.1. The calculations reported here were performed for all these data. As noted, the model is not expected to be reliable for $\sigma^* \lesssim 1$, and this will be discussed in what follows. The other system characteristics which enter the formalism are $\rho_{0B} = 6.20$ nm^{-3} for PS [125] and $\rho_{0S} = 4.21$ nm^{-3} for EB [126]. Since the observed radius of gyration of PS in EB is very similar to that in toluene (TOL) [127], the measured PS-TOL interaction parameter, i.e., $\chi_{SA} = 0.44$ was used. For the same reason, $b = 0.71$ nm was chosen for the statistical segment length. In the experimental analysis, Kent *et al.* [1, 2] used[128]

$$R_g = 0.0117 M_w^{0.595} , \tag{3.20}$$

for the radius of gyration R_g of an isolated PS, where M_w is the (weight averaged) molecular weight, and so the same expression was used to obtain σ^* for each Σ. It is important to recognize, however, that the use of this expression is not fundamental to the results presented here, but it does provide a useful way of analyzing them and comparing them directly with the presentation of the experiments.

Table 3.1: Polymers, free radii of gyration, R_g, and reduced surface coverage, σ^* used in the calculations. The polymers are labeled by the block molecular weights, in kg/mol, of the PDMS and PS blocks respectively. The values of σ^* were derived from parabolic density profiles fitted to the neutron reflectivity curves [1, 2].

M_w $4-30$	10-40	4.5-60	21-169	28-330
R_g 5.40 nm	6.40 nm	8.15 nm	15.01 nm	22.48 nm
σ^*	σ^*	σ^*	σ^*	σ^*
3.18	1.30	1.30	0.65	1.00
3.32	1.70	1.73	2.24	2.27
3.49	2.60	1.96	2.71	3.17
3.67	2.80	2.28	5.51	3.97
3.78	3.00	2.52	6.10	5.10
3.99	3.40	2.73	8.27	5.71
4.03	3.60	3.08	8.48	6.86
4.18	4.00	3.44	9.79	8.21
4.20	4.10	4.43	10.41	8.28
4.52	4.20	4.44	10.49	11.03
		4.66	10.67	11.39
		5.32	10.76	
		6.11		
		7.05		
		7.15		
		7.26		
		7.42		
		7.84		
		8.10		
		8.19		
		8.36		
		8.79		

The numerical results in this thesis are often presented in the form of the approximate power law dependences on the surface coverage and the degree of polymerization or the radius of gyration, R_g, of the dangling B-block of the copolymer. In the most of cases the calculated uncertainties in the values of exponents were determined to be on the order of ±0.02.

Figure 3.2 shows the profiles for the B-block for a particular polymer, 10-40 PDMS-PS, for different coverages. There is no qualitative change with coverage; quantitatively, both the maximum volume fraction and the brush thickness increase. These profiles are typical of all our calculations; the main body of the profile is quasi-parabolic, but there are also depletion and tail-like regions.

3.3.1 Thickness of the Brush

In the analytic theories of ADG [7, 28] and MWC [29], the thickness of the brush is defined as the distance from the surface to the point at which the density of the polymer becomes zero. However, because of the smooth vanishing of the numerical profile in the tail region (see figures 3.1 and 3.2), its total thickness is difficult to define, and it is more convenient to use its root-mean-squared thickness, x_{rms}. It is defined as

$$x_{rms} = \sqrt{\frac{\int_0^\infty dx\ \phi_B(x)\, x^2}{\int_0^\infty dx\, \phi_B(x)}}\ . \tag{3.21}$$

In both the ADG and MWC theories, $x_{rms} \propto h^*$ in the asymptotic limit, so x_{rms} would also scale as $Z\sigma^{1/3}$.

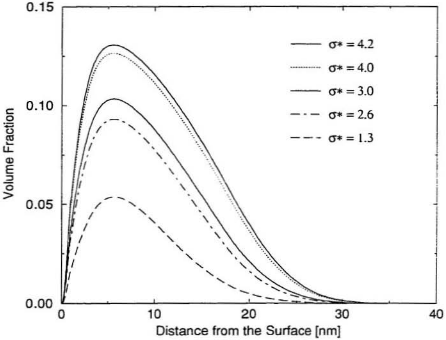

Figure 3.2: Calculated profiles for the PS block of the 10-40 PDMS-PS polymer, as in figure 3.1, for different values of σ^*.

The calculated values of x_{rms} are shown in figure 3.3. From this figure, one can conclude that x_{rms} increases with increasing molecular weight and surface coverage, σ^*. In fact, all the results fall very close to a single curve, which is nearly a straight line on this log-log plot for $\sigma^* \gtrsim 2$. This implies an approximate power law dependence for this range of σ^*. The best fit to these points gives

$$\begin{aligned} x_{rms} &\propto R_g^{0.87}\sigma^{*\,0.24} \\ &\propto Z^{0.81}\sigma^{0.24}, \end{aligned} \tag{3.22}$$

where $\sigma = \Sigma^{-1}$ and the uncertainties in the values of powers are ±0.02. The fit-

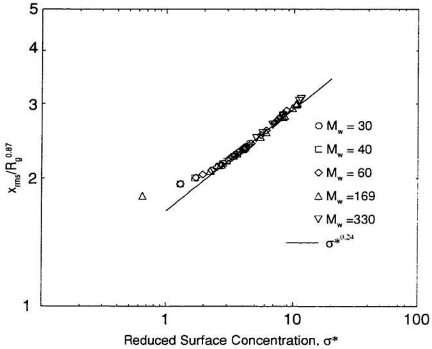

Figure 3.3: All the calculated values of the *rms* thickness of PS block, x_{rms}, as a function of R_g and σ^*. The straight line and the powers of R_g and σ^* represent the best fit to the points satisfying $\sigma^* \geq 2$. The units are nanometers for x_{rms} and R_g, and kg/mole for the PS molecular weights.

ted dependences of Eq. (3.22) are significantly weaker than those predicted for the asymptotic limit, especially the dependence on Z.

Although there is no qualitative difference in the general shape of the profiles for low and high coverage, the cases corresponding to $\sigma^* \lesssim 2$ are clearly in a different regime. The calculated values of x_{rms} deviate from the scaling found for larger σ^*, and the deviation becomes more pronounced with decreasing σ^*. In the limit of very small σ^*, the brush thickness tends to be independent of σ^*. This is expected for the mushroom regime, but these SCF predictions for this regime should not be considered as quantitative. What is of interest, however, is that the deviation from power law behavior begins around $\sigma^* \simeq 2$ for all molecular weights. This is the reason that in all subsequent fits, results for low coverage are not included in analysis, and only results for $\sigma^* \geq 2$ are considered.

The results shown in figure 3.3 fall close to the power law of Eq. (3.22). There is, however, some variation in these powers which can be extracted by fitting them to different ranges of σ^*. As just discussed, the behavior at very low coverages approaches that of the mushroom regime. For $\sigma^* \in [2, 4]$ the scaling strengthens to $x_{rms} \propto Z^{0.76\pm0.02} \sigma^{*\,0.21\pm0.02}$, reaching $x_{rms} \propto Z^{0.87\pm0.02} \sigma^{*\,0.29\pm0.02}$ for $\sigma^* \in [10, 12]$. This variation in the extracted powers is consistent with a picture of a continuous evolution from the mushroom regime towards the asymptotic brush regime.

3.3.2 Shape of the Density Profiles

To characterize the shape of the profiles near the surface, the maximum polymer volume fraction, ϕ_m, and its distance from the surface, x_m, are considered. As was the case for x_{rms}, all the calculated values of ϕ_m fall very close to a single curve, as is illustrated in figure 3.4. For $\sigma^* \gtrsim 2$, results fall on a straight line, described by

$$\begin{aligned} \phi_m &\propto R_g^{-1.20} \sigma^{*\,0.68} \\ &\propto Z^{0.10} \sigma^{0.68} \,. \end{aligned} \qquad (3.23)$$

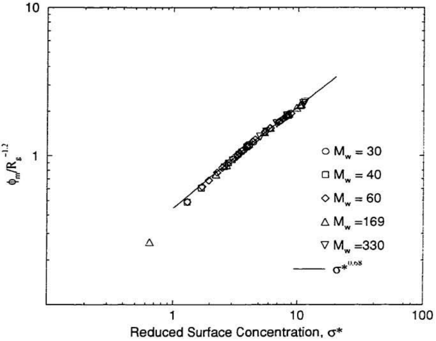

Figure 3.4: All the calculated values of the maximum volume fraction of the PS block, ϕ_m, as a function of R_g and σ^*. The straight line and the powers of R_g and σ^* represent the best fit to the points satisfying $\sigma^* \geq 2$. The units are the same as in figure 3.3.

The values of 0.10±0.02 and, in particular, 0.68±0.02 are quite close to the corresponding values of 0 and 2/3 predicted by the ADG and MWC theories.

As is qualitatively apparent from figure 3.2, the location of the maximum, x_m, is a slowly varying function of σ. Figure 3.5 quantifies this dependence. In all cases, x_m is on the order of R_g and is weakly dependent on σ^*, and these dependences fall very close to a single relation. Once again, fitting all the results for $\sigma^* \geq 2$ results in

$$x_m \propto R_g^{0.81} \sigma^{*\,-0.04}$$

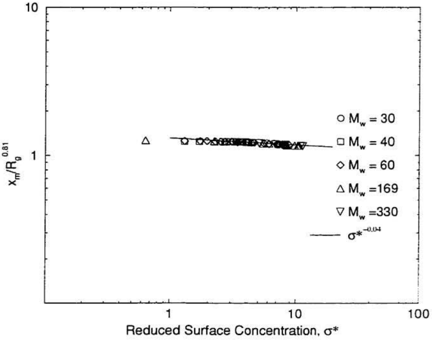

Figure 3.5: All the calculated values of the position of the maximum in the volume fraction of the PS block, x_m, as a function of R_g and σ^*. The straight line and the powers of R_g and σ^* represent the best fit to the points satisfying $\sigma^* \geq 2$. The units are the same as in figure 3.3.

$$\propto \; Z^{0.43}\sigma^{-0.04} \, , \tag{3.24}$$

with the uncertainties of ±0.02 in the values of powers. This cannot be compared with the theory of MWC [29] which neglects the depletion layer. It can be compared with the theory of ADG [7, 28] in which x_m corresponds to the distance at which the plateau value is reached, which scales as $\sigma^{-1/2}$. Thus there are two quite different pictures here: the numerical SCF theory predicts that the location of the maximum is controlled by R_g and is almost independent of σ, whereas the ADG theory predicts

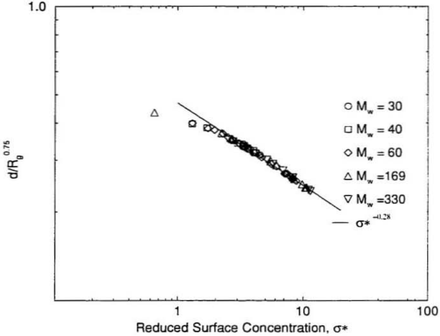

Figure 3.6: All the calculated values of the position of the half-maximum in the volume fraction of the PS block, d, as a function of R_g and σ^*. The straight line and the powers of R_g and σ^* represent the best fit to the points satisfying $\sigma^* \geq 2$. The units are the same as in figure 3.3.

the opposite. The numerical results are qualitatively consistent with the observations of Cosgrove [129] and the Monte Carlo studies of Chakrabarti and Toral [92].

Although the location of the maximum, x_m, is one characterization of the thickness of the depletion layer, it is not the only one. One can also define the distance from the surface at which the volume fraction reaches one half of its maximum value before reaching its peak value. This distance is denoted by d, and exhibited in figure 3.6. Once again, the results can be approximated by a single curve which becomes a straight line on this plot for all $\sigma^* \gtrsim 2$. The best fit for this line (with the uncertainties of ± 0.02) is

$$\begin{aligned} d &\propto R_g^{0.75} \sigma^{*\,-0.28} \\ &\propto Z^{0.12} \sigma^{-0.28} . \end{aligned} \tag{3.25}$$

This scaling is closer to the ADG prediction of $Z^0 \sigma^{-0.5}$, and quite different from that for x_m, Eq. (3.24). This latter difference reflects the changes in the shape of the density profiles in the depletion region, and indicates that the behavior of the thickness of the depletion layer depends on how it is defined.

3.3.3 Detailed Experimental Comparison

Kent *et al.*[1, 2] carried out neutron reflectivity experiments for the system described in section 3.2 using two sets of apparatus, the DESIR and SPEAR reflectometers at Saclay and Los Alamos, respectively. A large range of wavevector was available at SPEAR ($q = 4\pi \sin(\theta/\lambda)$ up to 0.12 Å^{-1}), allowing for a detailed study of the density profiles, by fitting the reflectivity data to a variety of functional forms. They examined pure parabolas, parabolas with depletion layers and exponential tails, different Gaussian forms, the error function and variable exponent forms. They concluded that a depletion layer and smooth tail were required to fit the curves, and that the best-fit profiles were very similar for all the functional forms with these included.

A detailed analysis was exhibited for the 4.5-60 polymer at a pressure of 2.7 dyn/cm, corresponding to $\sigma^* = 5.3$, determined by fitting a variable exponent model of the profile. They found that the density rose from a very low value at the surface to a maximum, after which it decreased smoothly to zero. The value of the maximum PS volume fraction depended very weakly on the function used in the fit, with ϕ_m ranging from about 0.115 to 0.125. Its location varied somewhat more, from about 4.4 nm to 7 nm. This greater variation may be due to fact that the different functional forms had different shapes in the depletion regions; as implied by the above analysis, the thickness of this layer is sensitive to its detailed description. They performed a similar analysis for coverages at $\sigma^* = 3.7$ to 5.4, and concluded that the thickness of the depletion layer was independent of the surface density in this range, also in agreement with result of Eq. (3.24).

For $\sigma^* = 5.3$, the SCF profile peaks at $x_m = 6.6$ nm with a value of $\phi_m = 0.12$, and is shown in figure 3.7. Both of these are within the ranges of the experimental fits. The rest of the profile, including the body of the profile and the smooth tail, are in good agreement with the fits; at any position x, the calculated and experimental profiles agreed to within $|\Delta\phi(x)| \leq 0.005$, and they both vanished at about 45 nm.

In determining the brush thickness, Kent *et al.* [1] found that the value of the brush thickness was the same for a simple parabola as for the more complex shapes, and they also concluded that the scaling dependences on σ were virtually the same. For consistency, therefore, they used fitted parabolas to determine the dependences of the thickness on molecular weight and surface density. They fitted all data to the

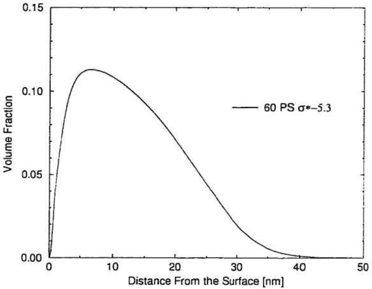

Figure 3.7: Calculated density profile for the dangling block of 4.5-60 PDMS-PS copolymer with $\Sigma = 39.4$ nm^2, which corresponds to $\sigma^* \simeq 5.3$.

form

$$\phi(x) = \phi_m \left[1 - \left(\frac{x}{h^*}\right)^2\right] . \tag{3.26}$$

with ϕ_m and h^* being the fitting parameters and presented most of their results in terms of h^*. In order to compare those results with the SCF calculation, in the following analysis the experimentally obtained values are converted to the *rms* thicknesses which, for parabolas, are related to h^* by

$$x_{rms} = \frac{h^*}{\sqrt{5}} . \tag{3.27}$$

In the rest of this section the experimental results obtained using Eq. (3.27) are compared with the calculated theoretical values.

The analysis of the results by Kent *et al.* showed that the brush thickness was constant to within experimental error for small σ^*, with the onset of stretching occurring at $\sigma^* \simeq 2$. This is the same threshold at which our power laws begin to be applicable, as seen in figures 3.3 - 3.6. For $\sigma^* \gtrsim 2$, the measured brush thicknesses could all be described reasonably by a simple linear function of σ^*.

$$\frac{x_{rms}}{R_g} = A + B\sigma^* , \tag{3.28}$$

with $A = 1.38$ and $B = 0.076$. In figure 3.8, the experimental data (open symbols) and this linear fit to them (solid line) are shown, as well as corresponding calculated values (filled symbols). These theoretical results exhibit a similar quasi-linear dependence on σ^*, although they do not all fall as close to one line as the experimental points do. Taken individually, however, the theoretical results for each polymer are very close to linear in σ^*. In Table 3.2, the results of fits to the straight line, Eq. (3.28), are presented for each polymer and for $\sigma^* \geq 2$. In all cases, the values of the intercept A, determined with the uncertainty of the order on ± 0.001, are very close to the value for the experimental data, but the slopes B, determined with the uncertainty of the order on ± 0.0005 vary over a factor of about 2. For $\sigma^* \lesssim 2$, the experimental values tend to a common value of about 1.5 R_g. Our calculated values at $\sigma^* = 2$ are all in the range of 1.47 R_g to 1.67 R_g, in agreement with the experiments. They are slightly higher than the values of about 1.43 obtained by Sorensen and Kovacs in MC simulations of chains with up to 73 units. For smaller σ^*, the lateral averaging inherent in the SCF calculation causes the polymer-polymer interactions to be undercounted and,

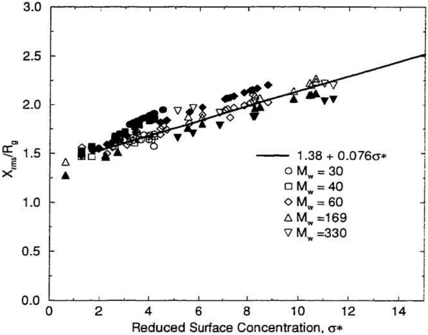

Figure 3.8: Comparison of the measured and calculated *rms* thicknesses, as defined by Eqs. (3.21) and (3.27), for the theoretical (filled symbols) and experimental values (open symbols), respectively. For $\sigma^* \geq 2$, all the experimental points can be well represented by a single linear dependence on σ^*, which is shown by the solid line.

furthermore, there should be swelling effects that are not included here. For these reasons, and as is the case for the fit to the experimental points, the linear relation cannot be extrapolated to smaller σ^*, and the values of the intercept, A, are not to be interpreted as applicable to very low coverage.

Although both the experimental and theoretical results can be reasonably described by linear functions of σ^*, they can be better described by power laws. Kent

Table 3.2: Coefficients, $A \pm 0.001$ and $B \pm 0.0005$, of the linear fit, Eq. (3.28). The first line is for the fit to all the experimental points, and the others are the fits to the theoretical values for each polymer. All fittings were done for $\sigma^* \geq 2$, and should not be extrapolated to smaller σ^*.

PDMS-PS Polymer	A	B
Experiment, all	1.38	0.076
4-30	1.44	0.113
10-40	1.40	0.110
4.5-60	1.40	0.093
21-169	1.32	0.076
28-330	1.36	0.062

et al.[2] found the best fit to their results to be

$$x_{rms} \propto M_w^{0.86} \sigma^{0.22} . \tag{3.29}$$

for all $\sigma^* \geq 2$. The values of these powers, 0.86 ±0.02 and 0.22 ±0.02, correspond directly to the theoretical values of 0.81 and 0.24, respectively, displayed in Eq. (3.22). Figure 3.9 shows all the experimental and the corresponding theoretical values plotted according to Eq. (3.29). The theoretical values are scattered about this line, as expected due to the small differences in the powers. For ease of comparison, the theoretical values are shown in this format according to Eq. (3.22) in figure 3.10. It can be recalled from section 3.3.1 that, in spite of the minimal scatter on figure 3.10, small variations in the values of the exponents with σ^* could be extracted from the theoretical values. Experimentally, changes were observed at small σ^*, but no strengthening relative to the overall dependence was detected for $\sigma^* \geq 10$.

In order to determine if the small differences between the experimental and the-

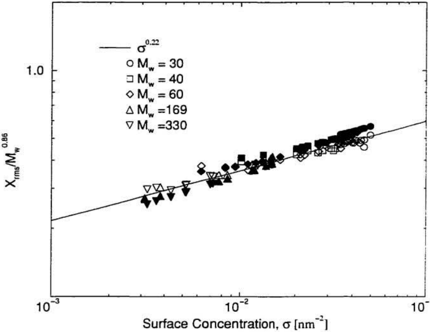

Figure 3.9: Measured (open symbols) and calculated (filled symbols) *rms* brush thicknesses, plotted according to the power law fit to the experimental data, Eq. (3.29), which is shown as the solid line. The units are the same as in figure 3.3.

oretical results discussed throughout this section are due to the treatment of the depletion layer and tail regions in the experiments. Kent analyzed six of the SCF profiles, three for each of the 4-30 and the 28-330 polymers. He first calculated the corresponding reflectivity curves and then fitted parabolas in the same manner as was done with the experimental reflectivity curves. The resulting values of the brush thickness for the 4-30 polymer fell very close to the single line obtained experimentally, shown on figure 3.8, but the values for the 28-330 polymer were moved somewhat further below. Together, these imply that the existence of separate linear

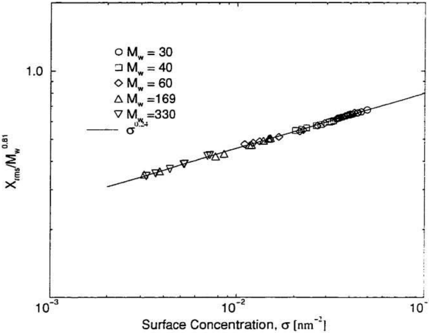

Figure 3.10: Calculated *rms* brush thicknesses for all the points satisfying $\sigma^* \geq 2$. plotted according to the best fit to them, Eq. (3.22), which is shown as the solid line. This relation provides a very good description of all these points. The units are the same as in figure 3.3.

relations, Eq. (3.28), for each polymer in the theoretical results, but a single one for the experimental results, as well as the small differences in the values of the fitted powers, cannot be explained by the treatment of the data.

3.3.4 Numerical and Analytic SCF Theory

The experimental brush thicknesses of Kent *et al.* were analyzed in terms of the parabolic profiles of MWC, so it is interesting to make a direct comparison between the numerical results and the analytic theory. As discussed in section 1.2.2. for highly stretched polymer brushes in good solvent, the analytic SCF theory of MWC predicts a parabolic profile described by Eq. (1.18) with the thickness of the brush given by Eq. (1.19). The parameter v appearing in these equations is related to the statistical segment length via [36]

$$\langle \boldsymbol{R}^2 \rangle = \frac{3Z}{v} \ . \tag{3.30}$$

where R is end-to-end distance of a free chain. Since, in the notation used in this thesis,

$$\langle \boldsymbol{R}^2 \rangle = Zb^2 \ , \tag{3.31}$$

where b is statistical segment length, one has the correspondence $v = 3/b^2$. Thus using Eqs. (3.30) and (3.31) and expressing the thickness of the parabolic profile in terms of the root-mean-squared thickness, h_{rms}, the profile of MWC can be written

$$\phi(x) \ = \ \frac{3}{4}\left(\frac{2\pi^2}{wb^2}\right)^{1/3} \Sigma^{-2/3}\left[1 - \frac{1}{5}\left(\frac{x}{h_{rms}}\right)^2\right] \tag{3.32}$$

$$h_{rms} \ = \ \frac{1}{\sqrt{5}}\left(\frac{4wb^2}{\pi^2}\right)^{1/3} Z\Sigma^{-1/3} \ . \tag{3.33}$$

Once again using Eqs. (3.30) and (3.31), the free energy per chain in the analytic SCF theory can be written as

$$F_c = \frac{9}{10}\left(\frac{\pi^2}{4b^2}\right)^{1/3} w^{2/3} Z\Sigma^{-2/3} \ . \tag{3.34}$$

The excluded volume parameter, w, can be expressed in terms of the Flory interaction parameter as

$$w = \frac{1}{\rho_{0B}}(1 - 2\chi) \ . \tag{3.35}$$

In order to probe these scaling relations, model calculations with Z ranging from 200 to 1000 were performed. All the pure component densities were chosen so $\rho_{0S} = \rho_{0B} = 1$ nm^{-3}. Furthermore, the segment statistical length was set to $b = 1$ nm and the value of the solvent-polymer interaction parameter χ was 0.4, which corresponds to $w = 0.2$. Since these are model calculations for polymer in good solvent, the reduced surface concentration σ^*, was calculated using

$$R_g^2 = \frac{1}{6} Z^{2\nu} . \tag{3.36}$$

where $\nu = 3/5$ [39]. All parameters are summarized in Table 3.3.

The parabolic and numerical profiles for $Z = 600$ and $\Sigma = 100$ nm^2 are presented in Figure 3.11. The maximum volume fraction is significantly lower in the numerical profile than in the theoretical one and the numerical profile extends farther from the surface. The depletion region alone does not account for the difference.

As is apparent from Eq. (3.32), the MWC theory predicts that the maximum polymer volume fraction, ϕ_m, is independent of the degree of polymerization of the grafted block. For the choice of parameters used here, it would satisfy

$$\phi_m = 3.466 \Sigma^{-2/3} . \tag{3.37}$$

By comparison, the best power law fit to the numerical results is

$$\phi_m = 1.709 Z^{0.06} \Sigma^{-0.63} . \tag{3.38}$$

with the uncertainties ±0.001 in the constant and ±0.02 in the values of powers. The quantitative comparison of the two approaches is presented in figure 3.12. First, the

Table 3.3: Degree of polymerization of dangling block Z. Σ and reduced surface coverage, σ^* used in the model calculations, good solvent.

Z	Σ [nm]^2	σ^*
200	100.0	3.02
	50.0	6.04
	25.0	12.09
	15.0	20.14
400	250.0	2.78
	125.0	5.55
	62.5	11.11
	31.25	22.21
600	400.0	2.82
	200.0	5.65
	100.0	11.29
	50.0	22.58
800	550.0	2.90
	275.0	5.80
	137.5	11.60
	68.75	23.20
1000	720.0	2.90
	360.0	5.79
	180.0	11.58
	90.0	23.16

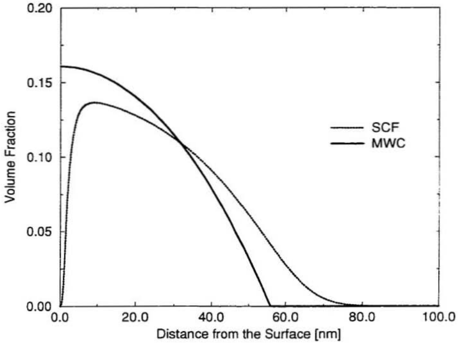

Figure 3.11: Parabolic and numerical profiles for $Z = 600$ and $\Sigma = 100$ nm^2.

powers of 0.06 ± 0.02 for Z and -0.63 ± 0.02 for Σ are consistent with the results for the PDMS-PS/EB system. Eq. (3.23). The scaling relations are also in very good agreement with the prediction of the analytic theory. however the numerical values are about 20% smaller than those proposed by MWC theory. The numerical values are closer to the analytic prediction for higher degree of polymerization and the deviation from analytic picture becomes more pronounced for shorter chains.

Turning to the brush thickness, the direct comparison of the numerical results with the analytic prediction of Eq. (3.33) is presented in figure 3.13. The best fit to

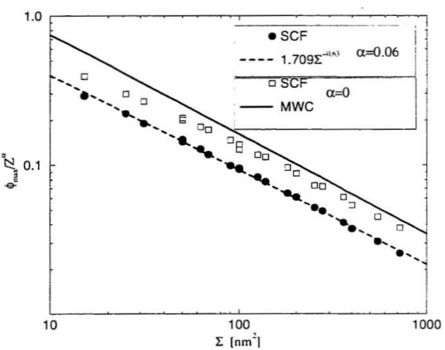

Figure 3.12: All the calculated values of the maximum volume fraction of polymer as a function of Σ and Z for numerical SCF theory, good solvent. Open symbols show numerical values and the solid line is the prediction of MWC theory Eq. (3.37). Closed circles are the numerical values scaled by $Z^{0.06}$. The dashed line is the best fit, Eq. (3.38).

the numerical results gives

$$x_{rms} = 0.526 Z^{0.86} \Sigma^{-0.30} . \tag{3.39}$$

with the uncertainties ±0.001 in the constant and ±0.02 in the values of powers. The filled circles are numerical results and the dashed line represents the line of best fit. The open squares show the numerical results scaled by Z^1 and the solid line is the prediction of MWC. Once again, these numerical results are in a good agreement

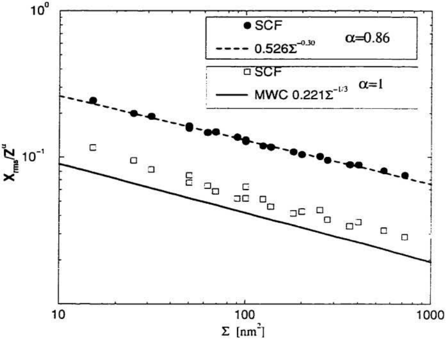

Figure 3.13: All the calculated values of the x_{rms} as a function of Σ and Z for numerical SCF theory, good solvent. Open symbols show numerical values scaled by Z^1. The solid line is the prediction of MWC theory Eq. (3.37). Closed circles are the numerical values scaled by $Z^{0.86}$. The dashed line is the best fit, Eq. (3.39).

with the corresponding results for the PDMS-PS/EB system, Eq. (3.22). The slightly greater power of Σ is consistent with the picture of a continuous evolution from the mushroom towards the asymptotic brush regime, since in this case larger values of σ^* have been included. Although the linear scaling (open symbols) describes the data reasonably well, it is clear that the significantly weaker scaling of Eq. (3.39) provides a better fit. An important conclusion which can be drawn from this comparison is that a careful analysis of data is needed to extract scaling powers, in order to see if the data really support Z^1 scaling.

Finally the free energy per chain is directly compared with the analytic theory of MWC. To calculate the free energy per chain, the values obtained through Eq. (3.18) have to be multiplied by Σ. Calculating the free energy per chain using Eq. (3.18) and looking for the best fit, it was found

$$F_c = 0.789 Z^{0.92} \Sigma^{-0.66} \,. \tag{3.40}$$

with the uncertainties ± 0.001 in the constant and ± 0.02 in the values of powers. The MWC theory predicts

$$F_c = 0.416 Z \Sigma^{-2/3} \,. \tag{3.41}$$

The power of 0.92 ± 0.02 is approaching the MWC value of unity, and the value 0.66 ± 0.02 is essentially in perfect agreement. The quantitative comparison of the two approaches is presented in figure 3.14. Again, the fit to the power 0.92 ± 0.02 is noticeably better than the linear Z dependence. As well, the numerical SCF results are about 10% larger than the analytic predictions.

In summary, the numerical SCF theory predicts brushes in which the maximum polymer density is about 20% less, the rms thickness is about 50% greater and the energy is about 25% greater, than those predicted by analytic SCF theory. The scaling relations reveal that R_g remains an important length scale [80].

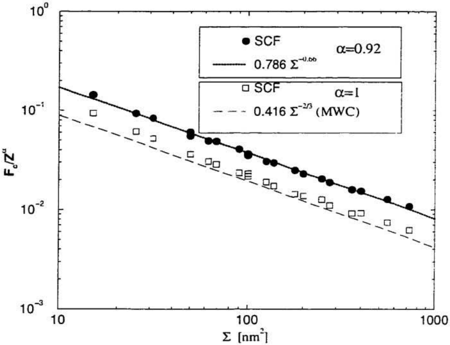

Figure 3.14: Free Energy per chain as a function of degree of polymerization Z, and surface coverage Σ in a good solvent. Open squares are the numerical values scaled by Z^1. The dashed line represents Eq. (3.41). Filled circles are the calculated values scaled according to Eq. (3.40), dotted line represents the line of the best fit.

3.4 Polymer Brush in a Θ Solvent

In this section, direct comparison of numerical SCF theory with the analytic theory of polymer brushes in Θ solvent developed by Shim and Cates [40] and by Zhulina *et al.* [42, 43] is presented. As in the previous section, the shape of the density profile, thickness of the brush and the free energy are analyzed. The values of parameters which enter the formalism are the same as in section 3.3.4, except that the Flory interaction parameter is $\chi = 0.5$, and the radius of gyration of the free

Table 3.4: Degree of polymerization of dangling block Z. Σ and reduced surface coverage, σ^* used in the model calculations, Θ solvent.

Z_A	Σ [nm]^2	σ^*
200	25.0	4.19
	15.0	6.98
	10.0	10.47
400	62.5	3.35
	31.25	6.70
	15.625	13.40
600	100.0	3.14
	50.0	6.28
	25.0	12.57
800	137.5	3.05
	68.75	6.09
	34.375	12.19
1000	180.0	2.91
	90.0	5.82
	45.0	11.64

chain is determined according to Eq. (3.36) with $\nu = 1/2$ [39]. All parameters are summarized in Table 3.4.

3.4.1 Characteristics of the Density Profile

Typical density profiles are shown in figure 3.15. Similar to the case of a good solvent, $\phi(x)$ rises from zero at the surface to its maximum value, ϕ_m, and then decreases smoothly to zero, but less rapidly than in case of a good solvent. The tail region is not as extended, and the body of the profile is more compact. Overall, the chains in a brush tend to be less stretched than in a good solvent conditions.

In the formalism presented by Shim and Cates [40], the density profiles are calcu-

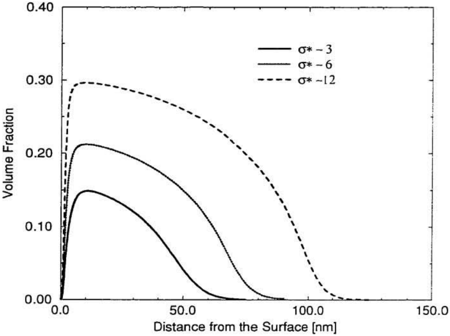

Figure 3.15: Calculated profiles for the dangling block with $Z = 800$ for different values of σ^*, Θ solvent.

lated numerically while in the work of Zhulina *et al.* [42, 43] the closed form expression is presented for Θ solvent. The density profiles of Zhulina *et al.* satisfy

$$\phi(x) = (12)^{1/4} b \Sigma^{-1/2} \left[1 - \left(\frac{x}{h}\right)^2\right]^{1/2} \tag{3.42}$$

$$h = \frac{4}{\pi}\left(\frac{1}{12}\right)^{1/4} b^2 \Sigma^{-1/2} Z\,, \tag{3.43}$$

where b is the statistical segment length and third virial coefficient was explicitly set to unity. For the Θ solvent the excluded volume parameter, Eq. (3.35) gives $w = 0$. The formal comparison between the numerical and elliptic profile of Eq. (3.42) is

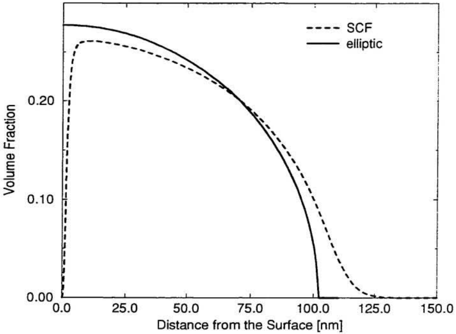

Figure 3.16: Formal comparison of the elliptic (solid line) and numerical profile (dashed line) for Z=1000 and $\sigma = 45$ nm^2 ($\sigma^* \approx 12$).

presented in figure 3.16. The overall agreement is very satisfactory, however, once again there is small depletion layer and smooth tail region.

As in the case of good solvent, a direct comparison of the analytic theory prediction with the numerical SCF calculation for the maximum volume fraction of polymer, ϕ_m, is possible. According to the analytic theory ϕ_m does not depend on the degree of polymerization and scales as $\Sigma^{-1/2}$. The best fit to the numerical SCF values gives

$$\phi_m = 1.448 Z^{0.02} \Sigma^{-0.49} , \tag{3.44}$$

with the uncertainties ±0.001 in the constant and ±0.02 in the values of powers.

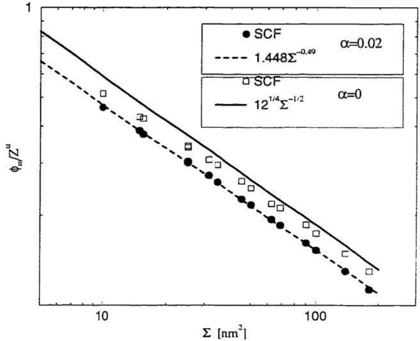

Figure 3.17: All the calculated values of the maximum volume fraction of polymer as a function of Σ and Z for numerical SCF theory, Θ solvent. Open symbols show numerical values, solid line is the prediction of theory Eq. (3.42). Closed circles are the numerical values scaled by $Z^{0.02}$. The dashed line is the best fit Eq. (3.44).

The quantitative comparison of the two approaches is presented in figure 3.17. The agreement in powers is very good and the numerical values (open squares) are very close to the analytic prediction specially for high values of Z and Σ. It has to be noted, however, that with the increasing Σ the reduced surface concentration decreases and the chains become more isolated and are no longer obliged to stretch away from the grafting surface. Furthermore, even for stretched chains the grafting density has to be high enough to suppress the lateral instability due to fluctuations tangential to the grafting plane [48]. Thus, it is important to determine the lower limit of the brush regime for the collection of end-grafted chains in a Θ solvent. In order to do so, some additional calculations were performed for all five values of Z, with σ^* varying between range [1.5, 2.5] and the functional dependence of the x_{rms} was investigated. Using only those values of Z and Σ for which the reduced surface concentration $\sigma^* \geq 3$ and looking for the best fit, it was found that

$$x_{rms} = 0.543 Z^{0.93} \Sigma^{-0.47} \tag{3.45}$$

$$x_{rms} = 1.678 R_g^{0.92} \sigma^{*\,0.47} , \tag{3.46}$$

with the uncertainties ±0.001 in the constants and ±0.02 in the values of powers. The calculated values of x_{rms} plotted according to Eq. (3.46) are shown in figure 3.18. As in the case of the polymer brush in a good solvent, the calculated values of x_{rms} deviate from the scaling found for larger values of σ^*, and this deviation begins at about $\sigma^* \simeq 3$.

For the elliptic profile, the x_{rms} thickness is simply $x_{rms} = h/2$ which, using Eq. (3.43), leads to

$$x^e_{rms} = 0.342 Z \Sigma^{-1/2} . \tag{3.47}$$

The direct comparison of the numerical results, Eq. (3.45), with the prediction of Eq. (3.47) is presented in figure 3.19. The filled circles are numerical results and a dashed line represents the line of best fit. The open squares show the numerical results scaled by Z^1 (linear in Z) and the solid line is the prediction of the analytic

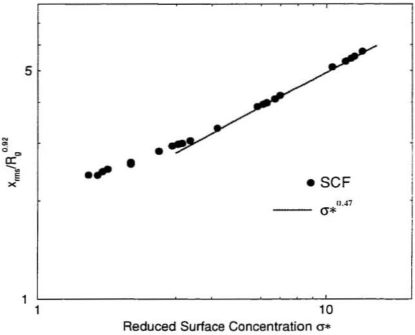

Figure 3.18: All the calculated values of the rms thickness as a function of R_g and σ^*. The straight line is the best fit to the points satisfying $\sigma^* \gtrsim 3$. Eq. (3.46).

theory. The scaling relation obtained from the best fit is very close to the analytic prediction, but the numerical prefactor is larger. This larger value is consistent with the density profiles of figure 3.16: the numerical profiles exhibit a depletion layer and tail region, ϕ_m is smaller, and these lead to a larger value of the *rms* thickness.

3.4.2 Free Energy of the Brush

In the work of Zhulina *et al.* [42, 43] and Halperin [41] the equilibrium structure of the grafted polymer layer is determined by the minimization of its conformational

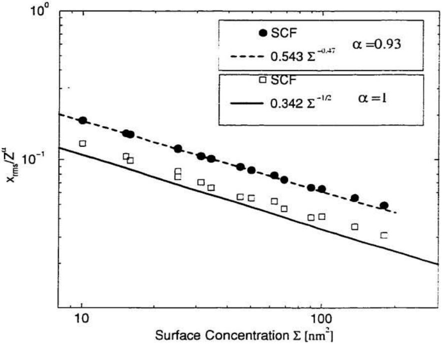

Figure 3.19: All the calculated values of the x_{rms} as a function of Σ and Z for numerical SCF theory, Θ solvent. The dashed line is the best fit Eq. (3.45). Open symbols show numerical values scaled by Z^1. The solid line is the prediction of the analytic theory Eq. (3.47).

free energy, which includes the contribution of elastic stretching in the layer. and volume (ternary) interactions

$$F_c = F_{el} + F_{int} \ . \tag{3.48}$$

Halperin [41] assumed a uniform distribution throughout the layer which is equivalent to the step function model of Alexander and de Gennes [7, 28]. In the approach of Zhulina *et al.* [42, 43] this energetic balance is done locally and the model is essentially an extension of the analytic theory of MWC [29]. The free energy per chain in

Zhulina's approach can be expressed as

$$F_c = \frac{1}{2}(3)^{1/2} b^2 Z \Sigma^{-1} , \tag{3.49}$$

where once again, the third virial coefficient was set explicitly to unity. This can be directly compared with the numerical SCF calculations. Calculating the free energy per chain using Eq. (3.18), and looking for the best fit, it was found

$$F_c = 0.935 Z^{1.00} \Sigma^{-1.02} , \tag{3.50}$$

with the uncertainties ±0.001 in the constant and ±0.02 in the values of powers. The numerical prefactor in Eq. (3.49) is equal 0.866. The numerical calculation are in excellent agreement with the analytic prediction. The scaling exponents are equal to within the uncertainty of ±0.02, but numerical prefactors differ by less than 10%. Comparison of the two approaches is presented in figure 3.20.

3.5 Summary

In this chapter, numerical SCF calculations were discussed and compared with recent experimental data of Kent *et al.* [1, 2], as well with the predictions of the scaling theory of Alexander [28] and de Gennes [7], the asymptotic SCF theory of Milner, Witten and Cates [29] for polymer brushes in a good solvent, and the analytic theory of Zhulina *et al.* [42, 43] for the Θ solvent case.

In keeping with the experimental situation, it was assumed that one of the copolymer blocks lies flat on the surface and the other dangles into the solution. The in-

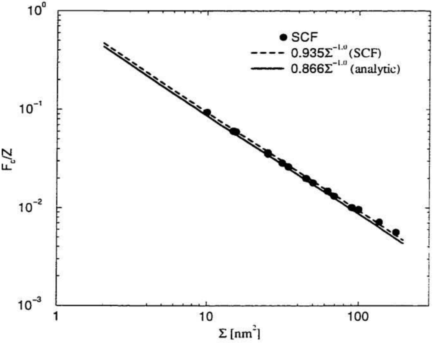

Figure 3.20: Free Energy per chain as a function of degree of polymerization Z, and surface coverage Σ in a Θ solvent. Filled circles are the calculated values scaled according to Eq. (3.50), dashed line represents the line of the best fit. The solid line is the analytic prediction of Eq. (3.49).

terphase region was assumed to contain all the A-B joints was taken to be 1 nm thick [130] for the comparison with the experiments and 2 nm thick for the model calculations. This model can be applied to the dangling block of adsorbed copolymers or to end-grafted polymers through the choice of the thickness of the interphase, and the modeling of the B block.

In the good solvent case, calculated density profiles all contain depletion layers, which are analyzed in terms of the location of the maximum and the half-maximum.

In all cases, the scaling of the maximum volume fraction with Z and σ was similar to the predictions for the asymptotic limit. However, the position of the maximum was on the order of R_g and only weakly dependent on the surface density. This contrasts with the prediction of the scaling theory that it would be independent of molecular weight and vary as $\sigma^{-1/2}$, but it is in accord with the experimental observations for this regime. The position of the *half*-maximum did vary with the surface density, but not as strongly as predicted by the scaling theory. These qualitative differences in the dependences of the location of the full and half maxima reflect changes in the detailed shapes of the profiles in this region, which suggests that the experimental characterizations of the depletion layer may need to include a careful specification of how the thickness is defined. This is consistent with the findings of Kent *et al.* [2] who found values of from 4.4 to 7 nm for the location of the maximum, depending on the assumed shape of the depletion layer. The SCF calculations yielded a value of 6.6 nm for this case, which is within this range.

The existence of a depletion layer in these results contrasts with some other cases in which there is no such layer. This can be explained by differences in the polymer/surface affinities. In the first cases, the chains are end-grafted or the surface is covered by the other block of the copolymer, so that the surface is strongly repulsive, there is no adsorption of the monomers along the chain and a depletion layer forms. In the others, the monomers along the chain can adsorb at the interface, filling in the depletion layer. Thus the interactions between the monomers and the surface can lead to different forms of the density profiles [129]. This effect will be discussed in chapter 5.

Beyond the maximum, the density decreases smoothly and reaches zero in an extended tail. This is consistent with the neutron reflectivity data, which could be fitted only if both depletion and tail regions are included. One might have expected that fluctuation effects and inhomogeneities parallel to the surface, both of which are ignored in the calculations, would have introduced discrepancies at the tip of the brush where the polymer densities are very low and vanishing. In fact, the calculated and fitted profiles agreed very well everywhere, even in the tail.

The numerical results were analyzed in terms of the approximate power law dependences, and for all cases the uncertainties in the values of powers were on the order of ±0.02.

It was found that the thickness of the brush could be described well by a single function for all polymers, which could be described by a simple power law over the range $2 \lesssim \sigma^* \lesssim 12$. The lower cutoff in this range is consistent with the experimentally observed onset of stretching, although the SCF calculation does not apply below this limit. Over this range, a best fit for this scaling was found to be $x_{rms} \propto {Z_A}^{0.81} \sigma^{0.24}$, which compares well with the experimental result of $x_{rms} \propto {Z_A}^{0.86} \sigma^{0.22}$. The experimental results for this range could also be described by $x_{rms}/R_g = A + B\sigma^*$, a form rather different from a power law. A similar result for each polymer was found, with nearly equal values of A, and similar but varying slopes, B.

One general conclusion that can be drawn from the first part of the study presented above is that there are, roughly speaking, three regimes of stretching. The first is characterized by $\sigma^* \lesssim 2$, and it corresponds to the mushroom regime. For $2 \lesssim \sigma^* \lesssim 20$, the polymers begin to stretch away from the surface. This stretching approaches the asymptotic limit beyond about $\sigma^* \gtrsim 20$, the third regime. It is important to note that, except for brushes formed by grafting from semi-dilute and concentrated solutions, virtually all experiments in a good solvent fall in the regime $\sigma^* \lesssim 15$, so do not correspond to the asymptotic regime.

The good agreement of numerical SCF calculations with the experimental data and some discrepancies with the analytic predictions of MWC motivated the next part of the study in which detailed quantitative comparison between analytic and numerical SCF theories was performed. Although many experimental data were analyzed in terms of the parabolic profile, it was found that numerically generated profiles extend farther than those predicted by the MWC theory, and the thickness of the grafted layer is about 50% thicker and the maximum volume fraction of polymer is about 20% lower than in the parabolic profile. The power law dependence of the stretching on the degree of polymerization is significantly weaker, although it tends toward the asymptotic values predicted by analytic theory as σ^* reaches ~ 20. The free energy of the brush obtained through numerical calculations is about 25% higher than predicted by the analytic theory.

The numerical SCF theory was also compared with the analytic predictions for the polymer brush in Θ solvent. The agreement between analytic and numerical theory is significantly better than in the case of a good solvent. The main reason for the very good agreement between the numerical and analytical approach is that in the Θ solvent the binary interaction disappears and only the ternary interaction forces the chains to stretch away from the surface. The numerical calculation suggests that the threshold for stretching is slightly bigger than for the brush in a good solvent and appears at $\sigma^* \gtrsim 3$.

Chapter 4

Compression of the Polymer Brushes

4.1 Introduction

In this chapter the properties of polymer brushes immersed either in a good or a Θ solvent and compressed normal to the grafting surface are discussed. For each case, the density profile, root mean squared thickness and free energy of the compressed brush, as functions of the degree of polymerization and surface coverage, are calculated and presented in the form of approximate power law dependences.

In most experimental studies on the compression of the polymer brushes, the Israelachvili technique is used [131, 132] in which two opposing brushes are brought together in an orthogonal cross-cylinder configuration. This is done to avoid the difficulty of achieving parallel alignment of two flat plates separated by a distance on the order of a hundred nanometers. Therefore, as mentioned in chapter 1, the force, F, as a function of separation is expressed in terms of $F(D)/R$ where R is the geometric mean of the radii of curvature of cylinders used in the Israelachvili force apparatus.

and D is the distance of the closest approach. Within the Deryaguin approximation [65], this is directly related to the free energy per unit area via Eq. (1.28), which is

$$\frac{F(D)}{R} = 2\pi \left(E(D) - E(\infty) \right) ,$$

where $E(D)$ is the free energy per unit area of the system at separation D and $E(\infty) = E_0$ is the free energy per unit area when the brushes attached to the opposite surfaces do not overlap. The free energy per unit area is a geometry independent quantity, hence in the theoretical description of compression, the flat parallel plates immersed in a solvent are considered.

In the analytic theories for polymer brushes in a good solvent, the free energy of the brush during compression can be expressed in terms of a free energy of the uncompressed brush, and some universal function of the reduced distance, $u = D/(2h)$, where D is the distance between the plates with end-grafted chains and h is the thickness of the uncompressed polymer brush. Thus, the long range force between the plates can be described in terms of reduced variables by a single universal function. In this chapter this property will be examined in detail.

As mentioned in chapter 1, in the analytic theories no distinction is made between the compression of one polymer brush by a second identical brush and the compression by a impenetrable surface [11, 40, 133]. Whitmore and Noolandi [64] performed comprehensive analysis of the compression forces in good, Θ and poor solvents, but only compression of the polymer brush by a second identical brush was discussed. To examine the quantitative effects of different ways of compression, three modes are considered in this chapter:

1. compression by second identical brush;
2. compression by a bare, repulsive surface, i.e. a "Hard Wall";
3. compression by a second surface which is neutral for adsorption.

The compression of the polymer brush by a second brush and by a second surface is schematically presented in figure 4.1.

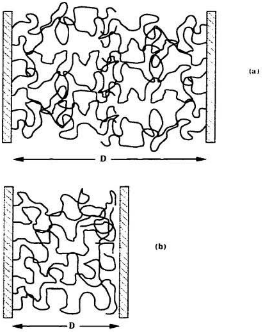

Figure 4.1: Compression of the polymer brush by a second brush (a) and second surface (b). The second surface can be either repulsive or neutral for adsorption

The other important conclusion of the analytic models is that during compression of two opposing brushes, they do not interpenetrate and retain their original shape. The step like profile remains flat [11], and parabolic and elliptic profiles remain parabolic or elliptic up to the midpoint between the plates, where there is a discontinuity in the slope. However recent numerical calculations [95-101] indicate that there is interpenetration, and this motivates some of the results presented in this chapter. The effect of interpenetration of opposing layers is quantified and the results are compared with these recent numerical studies.

The chapter is divided into two main parts. In the first, compression of polymer brushes immersed in good solvent is discussed. The second part deals with the same subject but the polymer brush is assumed to be under Θ solvent conditions. In both parts, the main focus is detailed comparison with the analytic SCF theories.

4.2 Numerical SCF Approach

The numerical SCF theory used in this chapter is essentially the same as that presented in chapter 3. In this section, the main points of the SCF theory and its modifications to treat the three cases introduced in section 4.1 are discussed.

Two infinite, parallel surfaces immersed in a solvent and located at $x = 0$ and $x = D$, are considered. Diblock copolymer or end-grafted homopolymer is attached either to both surfaces or just to the one at $x = 0$. In the case of copolymer, the A-block is assumed to be adsorbed tightly to the surface while the B-block extends into the solution and forms a polymer brush. As previously, the system is assumed to be invariant with respect to translation parallel to the surface and this implies that the problem becomes one dimensional.

The tightly adsorbed A-block is modeled by the same density distribution, Eq. (3.1), with an equivalent expression for the second surface at the distance D in the case of two brushes. It is again assumed that there is a narrow interphase, this time of width $a = 2$ nm which is typical of copolymer systems. As noted previously, the SCF results are not sensitive to this choice. The parameter l in Eq. (3.1) is chosen so that $\phi_A = 0.01$ at the edge of the interphase at $x = a$. The A-B joints are randomly distributed throughout the interphase.

In order to calculate the density profile and free energy of the dangling blocks, 2 or 3 propagators, for the case of 1 or 2 adsorbed layers respectively, have to be calculated. These propagators satisfy the modified diffusion equation (3.4), with appropriate initial and boundary conditions. The first propagator, $q_0(x, \tau)$, is proportional to the probability that a chain of length τ ends at x, given that it starts somewhere between the two surfaces. As in chapter 3, its initial condition is simply

$$q_0(x, 0) = 1, \text{ for } 0 < x < D . \tag{4.1}$$

The second propagator, $q_1(x, \tau)$, is proportional to the probability that a chain of length τ ends at x, given that it starts in the first interfacial region. Its initial condition is

$$q_1(x, 0) = \begin{cases} 1, \text{ for } 0 < x < a \\ 0, \text{ for } a < x < D . \end{cases} \tag{4.2}$$

If chains are also attached to the second surface, a third propagator, $q_2(x, 0)$ is needed.

It describes a chain starting at the second interface, and its initial condition is

$$q_2(x,0) = \begin{cases} 0, \text{ for } 0 < x < D - a \\ 1, \text{ for } D - a < x < D \,. \end{cases} \tag{4.3}$$

Once the the self-consistent solution is obtained, the density of the dangling block is constructed via

$$\phi_B(x) = \phi_{B1}(x) + \phi_{B2}(x) \,, \tag{4.4}$$

where $\phi_{Bi}(x)$ is the volume fraction of the dangling block attached to layer i and is given by Eq. (3.10), which is

$$\phi_{Bi}(x) = \frac{Z_B}{\Sigma \rho_{0B} \mathcal{Q}} \int_0^1 d\tau q_i(x,\tau) q_0(x, Z - \tau) \,. \tag{4.5}$$

with

$$\mathcal{Q} = \int_0^D dx\, q_1(x,1) \,. \tag{4.6}$$

In the case of a single brush and its compression, only q_0 and q_1 are needed, and $\phi_B(x) = \phi_{B1}(x)$. However, the second surface could be repulsive, attractive, or neutral. As mentioned before, two possibilities are considered. The first, sometimes labeled a repulsive surface, is one in which the polymer density falls smoothly to zero at the surface. This is described by the same boundary conditions as in the previous chapter (Eq. (3.6)) given by

$$q_i(0,\tau) = q_i(D,\tau) = 0 \text{ for } i = 0,1 \,. \tag{4.7}$$

The second possibility is a surface which is neutral for adsorption. The appropriate boundary conditions for this case are

$$\begin{aligned} q_i(0,\tau) &= 0 \text{ for } i=0,1 && (4.8)\\ \left.\frac{\partial}{\partial x} q_i(x,\tau)\right|_{x=D} &= 0 \text{ for } i=0,1\,, && (4.9) \end{aligned}$$

which allows for a finite density at the $x = D$ surface. The potential which appears in the diffusion equation for this part of calculation is chosen as

$$\omega(x) = \frac{\rho_{0S}}{\rho_{0B}} \left\{ \ln\left(\frac{1}{\phi_S(x)}\right) + \chi_{SB}\left[\phi_S(x) - \phi_B(x) - 1\right] \right\} + \omega_0\,. \tag{4.10}$$

where ω_0 is an arbitrary additive constant chosen to satisfy

$$\int_0^D dx\,\omega(x)\,\phi_B(x) = 0\,. \tag{4.11}$$

To determine the solvent volume fraction at x, Eq. (3.15), which follows directly from the incompressibility condition, is used.

For a given surface separation, D, the system is specified by the width of the interfacial region, a, degree of polymerization of the dangling block, Z, and its statistical segment length b, the densities of pure components ρ_{0S} and ρ_{0B}, and the average area per end-grafted chain Σ. For each value of D, the diffusion equations are solved in a self-consistent manner. Then, as in the previous chapter, the free energy per unit area of the brush can be determined as

$$\begin{aligned} \frac{E_0}{\rho_{0S} k_B T} &= \int_0^D dx \left\{ \phi_S(x)\ln\phi_S(x) + \phi_B(x) - \chi\phi_B^2(x) \right\} \\ &\quad - \frac{n_b}{\Sigma\rho_{0S}} \ln Q\,. && (4.12) \end{aligned}$$

The free energy *per chain*, in the same units, can be calculated from this via

$$F_c(D) = \frac{\Sigma}{n_b} \frac{E_0}{\rho_{0S} k_B T} \, . \tag{4.13}$$

for either the two brushes or bare surface compression. The number of brush-coated surfaces, n_b is defined as

$$n_h = \begin{cases} 1, \text{ two brushes compression} \\ 2, \text{ bare surface compression} \end{cases} \, . \tag{4.14}$$

4.2.1 Formal Comparison: One And Two Brush Systems

When one brush is compressed by a second one, they can, in principle, interpenetrate. This contrasts with the compression by a bare, repulsive surface, in which case the polymer density falls to zero at the surface. However it is straightforward to show that the compression by a second brush attached to a surface a distance D away can be described by the same total density and the free energy as during the compression by a surface which is neutral for adsorption a distance $D/2$ away. Whether or not the opposing brushes interpenetrate, if the density of the brush is not zero at the midpoint, then these two ways of compression produce the same free energies per chain and the total density profile.

To see this, consider the two brush system. The propagator $q_0(x, \tau)$ and the density distribution $\phi_B(x)$ are both symmetric about the midpoint. In addition,

$$\begin{aligned} q_1(x, \tau) &= q_2(D - x, \tau) \\ \phi_{B1}(x) &= \phi_{B1}(D - x) \, . \end{aligned} \tag{4.15}$$

Instead of solving this problem by calculating all these quantities in the full interval $[0, D]$, a new quantity can be defined

$$q_T(x, \tau) = q_1(x, \tau) + q_2(x, \tau) , \tag{4.16}$$

which is symmetric in the interval $[0, D]$ with respect to $x = D/2$. In particular, its spatial derivative is zero at the center of the interval, i.e.,

$$\left. \frac{\partial}{\partial x} q_T(x, \tau) \right|_{x=D/2} = 0 . \tag{4.17}$$

The propagator $q_T(x, \tau)$ is still zero at $x = 0$, and obeys the same initial conditions in the interval $[0, D/2]$. Because of these symmetry properties, the self-consistent problem has to be solved in the half-interval $[0, D/2]$, the polymer density can then be calculated by convolving q_0 and q_T and, in the second interval, it is obtained trivially from symmetry. Since q_T obeys exactly the same initial and boundary conditions in this interval as $q_1(x, \tau)$ does for the compression by a neutral surface located at $D/2$, the equivalence of these two cases is established. However, the opposing brushes can interpenetrate and it is important to address this problem.

4.3 Compressed Polymer Brush - Good Solvent

In this section the properties of a polymer brush immersed in a good solvent and compressed either by a second identical brush or one of the two types of the bare surfaces are investigated. Since the main focus is the comparison of numerical SCF theory with the analytic predictions given by MWC, model calculations for the same polymer systems described in section 3.3.4 were performed. The values of degree of polymerization, Z, and surface coverages used are summarized in Table 3.3.

As mentioned in chapter 1, the scaling theory of ADG as well as the SCF model of MWC assume that during the compression the opposing brushes do not interpenetrate, and the free energy of the compressed brush can be described by the product of the free energy of uncompressed brush and some universal function of the reduced distance. For compression by a bare surface, the reduced distance is defined simply as $u = D/h$, where D is the distance between the surfaces. For compression by a second brush, $u = D/(2h)$. The two cases can be treated in combination using the number of brush-coated surfaces, n_b, so that the reduced distance in each case is

$$u = \frac{D}{n_b h} . \tag{4.18}$$

For $u \geq 1$, each brush is unperturbed and the free energy per unit area of a single brush is just

$$E_0 = \frac{F_c^0}{\Sigma} , \tag{4.19}$$

where F_c is the free energy per chain of the uncompressed polymer brush, and Σ is the average area per adsorbed diblock molecule. As the brushes are compressed, $u < 1$, the free energy per chain increases. This change can be expressed as

$$\Delta E = E_0 f(u) , \tag{4.20}$$

and using Eq. (1.21), the universal function $f(u)$ for MWC theory is

$$f(u) = \frac{5}{9}\left(\frac{1}{u} + u^2 - \frac{u^5}{5}\right) - 1 . \tag{4.21}$$

As already noted, in the earlier theory of Alexander and de Gennes the scaling relation for the free energy and the brush height, obtained in a mean field approximation, are the same, but the numerical prefactors differ slightly in value. For the brush height, the numerical prefactor is $(1/2)^{1/3}$, and for E_0 it is $(3/2^{5/3})$. The change in the free energy of a compressed brush can be expressed in the same functional form as Eq. (4.20), but with $f(u)$ given by

$$f(u) = \frac{2}{3}\left(\frac{1}{u} + \frac{u^2}{2}\right) - 1 . \tag{4.22}$$

For small compressions, $u \lesssim 1$, less energy is required to compress the MWC brush than the ADG brush, i.e., it is softer. For large compressions, the theories predict the same functional dependence on u, although the numerical prefactors, E_0, differ. Using the Deryaguin approximation, Eq. (1.28), for each of the analytic theories, the force is given by

$$\frac{F}{R} = 2\pi n_b E_0 f(u) . \tag{4.23}$$

In order to compare directly the analytic predictions with numerical SCF calculation, the reduced distance between the surfaces is expressed in a manner analogous to u defined through Eq. (4.18), but using the rms thickness of the uncompressed brush x^0_{rms}, instead of h

$$\tilde{u} = \frac{D}{n_b x^0_{rms}} . \tag{4.24}$$

During the compression the density distribution can be characterized by its rms

thickness defined by

$$x_{rms} = \sqrt{\frac{\int_0^{D/n_b} dx\, x^2 \phi_B(x)}{\int_0^{D/n_b} dx\, \phi_B(x)}} \, . \tag{4.25}$$

If the opposing brushes do not overlap, or if the bare surface does not compress the brush, Eq. (4.25) defines the rms thickness of uncompressed brush, x^0_{rms}, and is equivalent to Eq. (3.21). For compression by the repulsive surface or the neutral for surface, Eq. (4.25) describes the single brush. For the compression of two brushes, Eq. (4.25) describes the total polymer distribution up to the midpoint between the surfaces.

Experimentally, force (F) versus separation D data are presented as $F(D)/R$ and are detectable on the order of a few μN/m [39], and so the calculations extend to surface separations corresponding to this order of magnitude in the force.

As discussed above, there are three modes of compression that can occur without incurring the complications of bridging. In section 4.2.1 the equivalence of the two cases corresponding to two brushes or a surface which is neutral for adsorption has been shown. In the following section the compression of polymer brush by repulsive and neutral surfaces will be discussed. Next the problem of the interpenetration will be addressed.

4.3.1 Compression by a Repulsive Surface

As long as the repulsive surface is far from the tip of the brush, the density profile remains unchanged and there is no force between the surfaces. When the repulsive

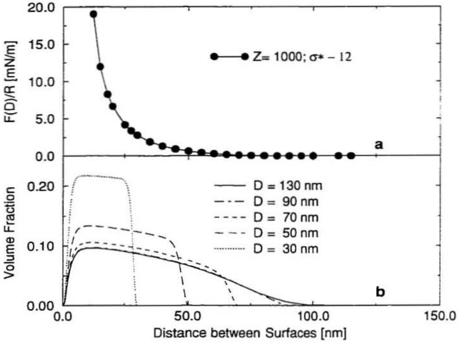

Figure 4.2: Compression of the polymer brush by a repulsive surface. Force curve for polymer characterized by $Z = 1000$. and $\Sigma = 180$ nm^2 as a function of the separation between the plates (a). Density profile of the polymer brush during the compression (b).

surface reaches the tip of the brush, the density profile starts to be altered. A typical force curve, as well as the polymer density distribution, are shown as functions of the separation between the surfaces in figure 4.2. At the initial stage of the compression only the tail region is compressed and the body of the profile remains essentially unchanged. The density profile still has all the features of the uncompressed brush, i.e., a depletion layer, the main body throughout which the density decreases monotonically, and an exponential-like tail region. With decreasing separation, the profile becomes more compact, the tail region vanishes, the depletion layer starts to diminish, and the profile becomes flatter. For a polymer with $Z = 1000$ and $\Sigma = 180$ nm^2 the *rms* thickness of the uncompressed brush, x^0_{rms} is approximately 45 nm and at approximately this separation the profile becomes step-like and the force between the surfaces starts to increase rapidly.

The force curves for all cases studied are shown in figure 4.3. As is apparent from this figure, with the increase of reduced surface concentration the force curves become steeper. Similarly as the degree of polymerization of the dangling block decreases, the force required to compress the brush by unit length becomes greater. In general, the brushes comprised of shorter chains and higher reduced surface concentration are harder to compress.

To extract scaling dependences of the force as a function of the degree of polymerization and surface concentration, the data collapse technique was used. In this method one assumes that all the force curves can be described in terms of a scaled distance and force, and that these scaled variables obey power law dependences on Z and Σ, i.e., one looks for the powers α, β, γ and ε such that

$$\frac{F(D)}{R} = Z^{\alpha}\Sigma^{\beta} g\left(\frac{D}{Z^{\gamma}\Sigma^{\epsilon}}\right) . \tag{4.26}$$

gives the best description of all the force curves. Equation (4.26) can then be written as

$$F_{\alpha\beta}(D) = g(D_{\gamma\epsilon}) . \tag{4.27}$$

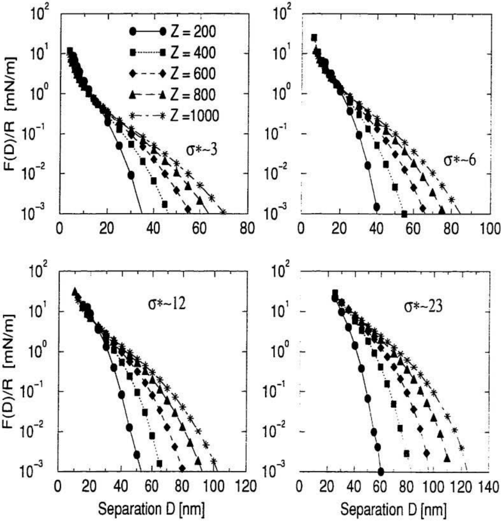

Figure 4.3: Compression of the polymer brushes by a repulsive surface. Force curves for all polymer $Z = 200 - 1000$, and all σ^*. (a) $\sigma^* \sim 3$, (b) $\sigma^* \sim 6$. (c) $\sigma^* \sim 12$. (d) $\sigma^* \sim 23$. The symbols are the same as in figure 4.3 (a).

where

$$F_{\alpha\beta}(D) = \frac{1}{Z^{\alpha}\Sigma^{\beta}} \frac{F(D)}{R} , \tag{4.28}$$

is a scaled force, and

$$D_{\gamma\epsilon} = \frac{D}{Z^{\gamma}\Sigma^{\epsilon}} , \tag{4.29}$$

is a scaled distance. Each force curve can be labeled by the corresponding degree of polymerization, Z_i, and surface concentration Σ_j. If one defines

$$I_{i,j,i',j'} = \frac{\int dx [F^{i,j}_{\alpha,\beta}(x) - F^{i',j'}_{\alpha,\beta}(x)]^2}{\frac{1}{2}\int dx [F^{i,j}_{\alpha,\beta}(x) + F^{i',j'}_{\alpha,\beta}(x)]^2} . \tag{4.30}$$

and

$$I(\alpha, \beta, \gamma, \varepsilon) = \sum_{i,j,i',j'} I_{i,j,i',j'} , \tag{4.31}$$

then minimizing $I(\alpha, \beta, \gamma, \varepsilon)$ determines the scaled variables. To find the minimum of $I(\alpha, \beta, \gamma, \varepsilon)$, the force was expressed in μN/m and the values greater than 1 μN/m were used as an input to the minimization routine E04JAF supplied in the NAG library [134] (the details are discussed in Appendix A). It was found that the best description of force curves is given by $\alpha = 0.64 \pm 0.02$, $\beta = -1.57 \pm 0.02$, $\gamma = 0.87 \pm 0.02$, $\varepsilon = -0.32 \pm 0.02$ and the result is presented in figure 4.4.

The important conclusion, which can be drawn from the figure 4.4, is that if the force curve can be described in terms of scaled variables, then all the force curves should collapse to a single curve. This is the case for moderate and high compression. At the initial stage of compression, there is considerable dispersion from the universal behavior, but interestingly, data sets which correspond to different degrees

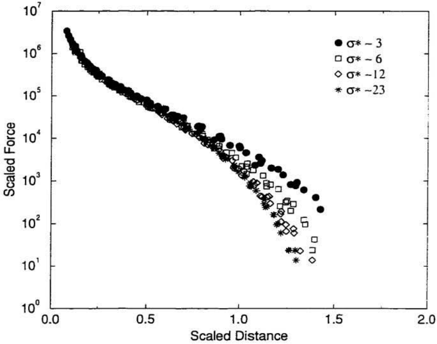

Figure 4.4: Compression of the polymer brush by a repulsive surface. The scaled force, g, as a function of scaled distance, as defined in Eq. (4.26) for all degree of polymerization, Z, and reduced surface concentration, σ^*. The force, F/R in units of μN/m is scaled by $Z^{\alpha}\Sigma^{\beta}$, and distance between the plates expressed in nm is scaled by $Z^{\gamma}\Sigma^{\epsilon}$. The values of exponents are $\alpha = 0.64$, $\beta = -1.57$, $\gamma = 0.87$, $\epsilon = -0.32$ with uncertainties ± 0.02.

of polymerization but the same value of σ^* are well described by single functions.

According to the MWC theory, if the distance between the plates is expressed in terms of reduced distance, $\tilde{u}$, given by Eq. (4.24) and the free energy difference, ΔE, given by Eq. (4.20) is scaled by the free energy of the uncompressed brush, E_0, then all the numerical results should once again collapse to a single curve, which would be given by Eq. (4.21) with u replaced by $\tilde{u} = u/\sqrt{5}$. The result of this procedure, along with the MWC curve, is presented in figure 4.5. In scaling the numerical and MWC energy curves, the numerical and MWC values for E_0 were used respectively.

The numerical results follow the general form of the universal function predicted by MWC theory, but they all fall above that prediction, and as in the case of scaled variables, there is considerable dispersion. Bearing in mind that the normalizing constant E_0 is about 25% higher for the numerical values than for the analytic prediction, the overall difference between the numerical and analytic curves is about a factor of 2 to 2.5, depending on which data sets characterized by the same value of σ^* are chosen for comparison. As in the case of scaled variables, data sets corresponding to different values of the degree of polymerization but the same value of σ^* are well described by a single function.

The results presented in figures 4.4 and 4.5 suggest that for finite σ^*, the force, or correspondingly the free energy difference, can not be described in terms of a universal function of the scaled or reduced distance between the plates. Data sets characterized by the same value of σ^*, however, can be described by a single function of these variables. This suggests that the radius of gyration of the free molecule, R_g, is a relevant length scale during the compression of the polymer brush by a repulsive surface. Furthermore, these results indicate that, during the initial stage of compression, the main body of the profile is essentially unchanged and the force is due to the deformation of the tail region, since the overall characteristics of the density distribution within the brush depend primarily on the reduced surface concentration, σ^*.

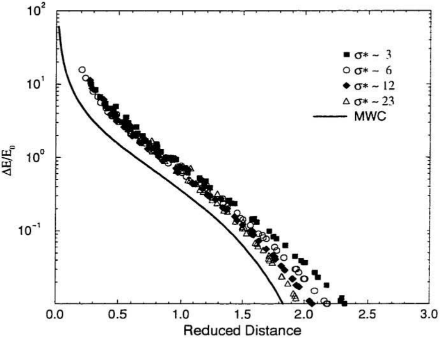

Figure 4.5: Compression of the polymer brush by a repulsive surface. Free energy difference per unit area in μN/m scaled by free energy of uncompressed brush as a function of the reduced distance given by Eq. (4.24). Symbols are the numerical results corresponding to different values of σ^*, and solid line is the analytic prediction of MWC theory, Eq. (4.21).

There is, however, another way to look for the universal behavior of the polymer brush during the compression. If a simple measure of the brush deformation is defined as

$$\xi = \frac{x_{rms}}{x_{rms}^0} \, . \tag{4.32}$$

the dependence of the force on this variable can be examined.

For the MWC profiles, the density profile remains parabolic during the compression, with non zero density at the outer edge of the profile, and simple algebra yields

$$\xi = \frac{1}{\sqrt{3}}\tilde{u}\sqrt{1 - \frac{2}{5^{5/2}}\tilde{u}^3}\,. \tag{4.33}$$

The calculated values of ξ, and the curve of Eq. (4.33) are illustrated in figure 4.6. For small $\tilde{u}$, i.e., very large compression, ξ is a linear function of separation between the plates, D, and the numerical results all reduce to the analytic function of Eq. (4.33). However, for finite σ^*, the initial deformation commences at larger values of $\tilde{u}$, where most of the deformation is occurring in the tail region. Once again, the greatest difference occurs for the smallest σ^*, which is consistent with the fact, that relative to the entire brush, the tail region is largest for smallest σ^*. For clarity, the values corresponding to $\sigma^* \sim 6$ and $\sigma^* \sim 12$ are not shown in the figure 4.6, they lie in between the values corresponding to the minimum and maximum values of σ^*.

Figure 4.7 shows the same results as in figure 4.5, but plotted versus ξ. Even at small deformations, the free energy differences all reduce much more closely to a single function, which is similar in shape to the analytic prediction, although different in magnitude by the same factor as in figure 4.5.

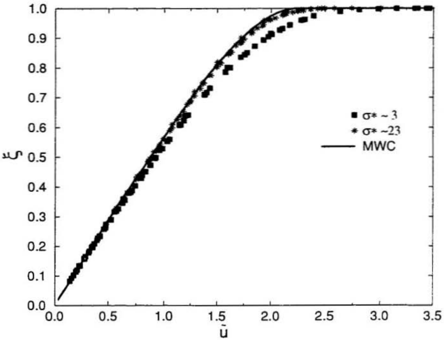

Figure 4.6: Compression of the polymer brush by a repulsive surface. The parameter ξ plotted as a function of the reduced distance $\tilde{u}$. good solvent. Symbols correspond to the numerical values, and the solid line is the analytic function of Eq. (4.33).

4.3.2 Compression by a Neutral Surface

In this section, compression of the polymer brush by a surface which is neutral for adsorption is discussed. As discussed earlier, such a system characterized by a separation D can be described in the same terms as two brushes attached to surfaces separated by the distance $2D$. However, since the force between the plates is related to the free energy difference per unit area, the force in the case of compression of a single brush by a neutral surface is one half of the force between two brushes.

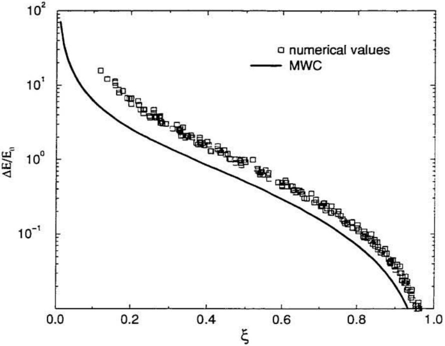

Figure 4.7: Compression of the polymer brush by a repulsive surface, good solvent. Free energy difference per unit area scaled by free energy of uncompressed brush as a function of the parameter ξ given by Eq. (4.32). Symbols are the numerical results corresponding to all values of σ^*, and solid line is the analytic prediction of MWC theory, Eq. (4.21) with u replaced by ξ through Eq. (4.33).

A typical force curve and the density profiles of the dangling block during compression of the polymer brush by a surface which is neutral for adsorption are shown in figure 4.8. As in the case of compression by a repulsive surface, at the initial stage of compression only the tail region is affected, and the body of the profile remains almost unchanged. In this case, however, there is an increase in the density at the neutral surface, and as the separation decreases the long range force between the surfaces increases gradually.

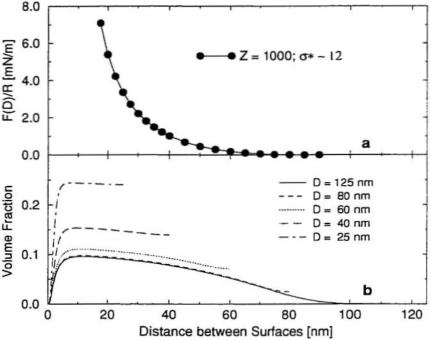

Figure 4.8: Compression of the polymer brush by a neutral surface, good solvent. Force curve for polymer characterized by $Z = 1000$, and $\Sigma = 180$ nm^2 as a function of the separation between the plates (a). Density profile of the polymer brush during the compression (b).

The comparison between compression by repulsive and neutral surfaces is presented in figure 4.9. The repulsive interaction between the surfaces becomes detectable for compression by a repulsive surface at a larger distance than for compression of the polymer brush by a neutral one. This indicates that during the initial compression by a repulsive surface the deformation of the tail region affects the entire profile, while during compression by a neutral for adsorption surface only the outer regions of the brush are affected. Thus, for the initial compression by a neutral

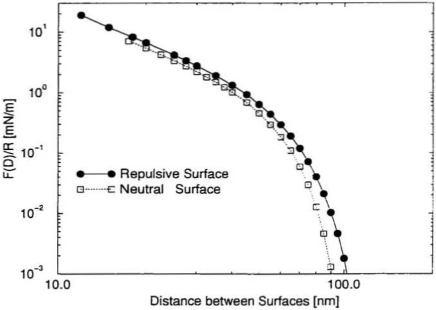

Figure 4.9: Force between the surfaces as function of separation for the polymer brush characterized by $Z = 1000$ and $\sigma^* \simeq 12$, good solvent. Filled circles correspond to the compression by a repulsive surface, open squares are the numerical results for the compression by a neutral for adsorption surface.

surface the body of the profile maintains its original shape and starts to deform at smaller separations.

As in the case of compression by a repulsive surface, the force can be analyzed in terms of scaled variables and a universal function of the separation. Using exactly the same technique of data collapse, Eqs. (4.26)-(4.29), it was found that the best description of all the force curves is given for

$$F_{\alpha,\beta}(D) = \frac{1}{Z^{\alpha}\Sigma^{\beta}}\frac{F(D)}{R}, \tag{4.34}$$

for $\alpha = 0.92 \pm 0.02$ and $\beta = -1.72 \pm 0.02$ with scaled distance

$$D_{\gamma\varepsilon} = \frac{D}{Z^{\gamma}\Sigma^{\varepsilon}} \ . \tag{4.35}$$

for $\gamma = 0.89 \pm 0.02$ and $\varepsilon = -0.35 \pm 0.02$. In chapter 3 it was shown that the free energy of the uncompressed brush scales as $E_0 \propto Z^{0.92\pm0.02}\Sigma^{-1.66\pm0.02}$, and the *rms* thickness of uncompressed brush $x^0_{rms} \propto Z^{0.86\pm0.02}\Sigma^{-0.30\pm0.02}$.

Since the values of the exponents α and β are essentially the same as those for the free energy, the scaled force is equivalent to the free energy difference per unit area for a given distance between the surfaces scaled by the free energy per unit area of the uncompressed brush. Similarly, the values of the exponents γ and ε are very similar to those for the *rms* thickness, and the scaled distance is equivalent to the reduced distance, $\tilde{u}$, given by Eq. (4.24). As was discussed before, according to the MWC theory, if the free energy difference, ΔE, is scaled by E_0, and the distance between the plates is expressed in terms of $\tilde{u}$, all the force curves should collapse to a single curve given by Eq. (4.21) with u replaced by $\tilde{u}$. Figure 4.10 shows the numerical results for the free energy difference, ΔE, as a function of $\tilde{u}$ for compression by a neutral surface together with the analytic prediction of MWC. Comparing the figure 4.10 with figure 4.5, the results are much less dispersed and in better agreement with the analytic function of MWC. However, the normalization constant E_0 is about 25% larger for the numerical results and this implies an overall difference of about a factor of 1.5 to 2 depending on which set of data, i.e. which value of σ^*, is used for comparison. This result is consistent with Watanabe and Tirrell's comparison of

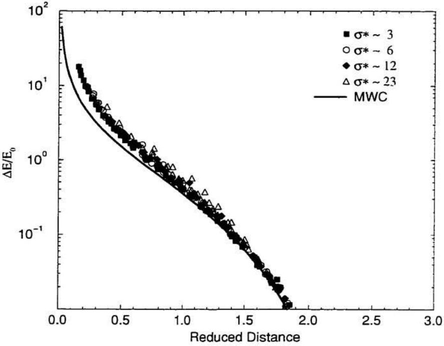

Figure 4.10: Compression of the polymer brush by a neutral for adsorption surface. good solvent. See the caption to figure 4.5 for more details.

their observations with the MWC theory [52].

Figure 4.11 shows the brush deformation ξ as a function of the reduced distance $\tilde{u}$ for the compression of the polymer brush by a neutral surface. From figure 4.11. it is apparent that the brush would encounter the neutral surface beyond $\tilde{u} \simeq \sqrt{5}$, especially for small σ^*. Since ξ remains essentially unity in this case, it means that, initially, only the density at the outer region of the brush is changing, with virtually no brush compression or detectable force developing until smaller distances between the surfaces (see fig. 4.8b). Since it was shown that the compression by a neutral surface is

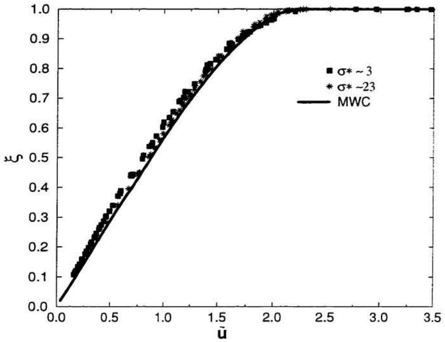

Figure 4.11: Compression of the polymer brush by a neutral surface, good solvent. The parameter ξ as a function of the reduced distance $\tilde{u}$. Symbols correspond to the numerical values, solid line is the analytic function of Eq. (4.33).

equivalent to the compression of two identical brushes, it can be also concluded from figure 4.11 that, for initial compression, two opposing brushes can interpenetrate. The interpenetration of the brushes will be the subject of the next section.

Finally, figure 4.12 shows the equivalence of all three cases, when expressed in terms of the parameter ξ, introduced in Eq. (4.32). All the calculations of the free energy differences per unit area of a single brush compressed by a repulsive surface, a surface which is neutral for adsorption or by a second brush, are all included in this graph. This indicates that the results of the numerical SCF theory, when expressed

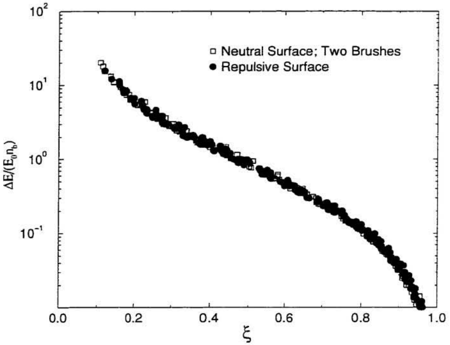

Figure 4.12: The equivalence of the three modes of compression, good solvent. The free energy difference scaled by the free energy of uncompressed system as a function of ξ parameter defined in Eq. (4.32).

in terms of a suitable brush deformation characteristic, can be described by a single function.

4.3.3 Interpenetration of the Polymer Brushes

The analytic theories assume that, when two identical brushes are compressed, they do not interpenetrate. Experiments do not provide a clear measure of any interpenetration, as none have been performed on the density profile of the brush originating from each surface in this case. As was mentioned in chapter 1, an argument for the noninterpenetration assumption is that the stretching which occurs in the single brush is caused by swelling into the pure solvent bath in order to minimize the interactions within the brush. When the two brushes are brought together, this tendency is removed [39]. This argument, however can be only applied to the scaling picture of the ADG theory, in which it is assumed that all the chains are uniformly stretched. In the analytic SCF theory of MWC, the space available to relieve crowding increases with increasing distance from the surface, and the free end of every chain has zero stretching energy. If one assumes that the density profile remains parabolic with a cusp at the midpoint, then the non-interpenetration follows, since a fictitious classical particle will always travel to the nearer of the two surfaces [29]. In the present formalism, none of these assumptions are made and, in general, the opposing brushes can interpenetrate. Furthermore the formalism outlined in section 4.2 allows for the determination of the density profile of each brush, Eqs. (4.4)-(4.6), and the question whether the opposing brushes interpenetrate during compression can be probed in detail.

Evidence for brush interpenetration in the numerical calculations has already appeared, i.e., in comparison of figure 4.6 and figure 4.11. For compression of two brushes the rms thickness of the total density distribution $\phi_B(x)$ for $0 \leq x \leq D/2$ remains virtually unchanged beyond $\tilde{u} \simeq \sqrt{5}$, especially for small σ^*. During the compression of a polymer brush by a bare, repulsive surface, the brush characterized by small values of σ^* is deformed first for $\tilde{u} \gtrsim \sqrt{5}$. The chains in a brush characterized by the smallest σ^* are stretched the least, but when they are compressed by a repulsive surface they retract the most. This is not the case during the compression of two brushes which means that a finite chain density remains in the middle between the surfaces, so the opposing brushes do interpenetrate. This situation can be understood on the basis of configurational entropy, since restricting all of each chain in the volume described by $x < D/2$ would lower the entropy [135].

In Figure 4.13 (a), the total density profile for the polymer characterized by $Z = 1000$ and $\Sigma = 180$ nm^2, which corresponds to $\sigma^* \simeq 12$, compressed to the distance which corresponds to $\tilde{u} = 1.45$, is shown. The solid line represents the density profile predicted by the analytical theory. Figure 4.13 (b) shows the contribution of each brush to the total. The numerically generated profiles are flatter than those of MWC, and the individual brushes interpenetrate up to a distance 1/3 of their total extension.

The interpenetration of the opposing brushes for surfaces separated by a distance D, can be quantified by the quantity $I(D)$ defined as [101]

$$I(D) \equiv \frac{\int_0^{D/2} dx\, \phi_{B2}(x)}{\int_0^{D/2} dx\, \phi_B(x)} . \tag{4.36}$$

This expression, Eq. (4.36) is equal to the fraction of monomers from each brush that penetrate beyond the midpoint. It can easily be shown to be equivalent to

$$I(D) = \frac{\Sigma}{Z} \int_0^{D/2} dx\, \phi_{B2}(x) = \frac{\Sigma}{Z} \int_{D/2}^{D} dx\, \phi_{B1}(x) . \tag{4.37}$$

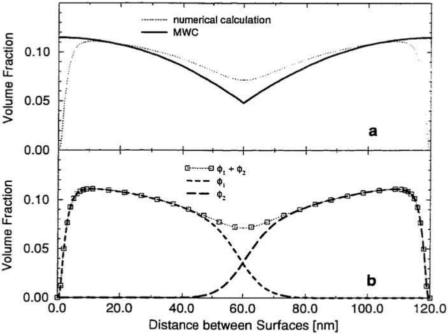

Figure 4.13: Compression of the polymer brush by a second identical brush, good solvent. Total density profile for the polymer with $Z = 1000$, $\Sigma = 180$ nm^2, numerical and analytic profile of MWC theory (a). Contribution of each brush to the total density (b).

Witten, Leibler and Pincus [136] estimated the depth, δ, to which the opposing layers interpenetrate to be

$$\delta \propto \left(\frac{Z^2}{D/2}\right)^{1/3} . \tag{4.38}$$

As shown by Murat and Grest [101], one can obtain a scaling prediction for the overlap by assuming that the density associated with each brush at the center is one half of the total, and that the profile of each brush decays exponentially beyond the midpoint with characteristic length δ. Integration yields

$$I(D) \propto \frac{\Sigma}{Z}\phi_{th}\left(\frac{D}{2}\right)\delta \, , \tag{4.39}$$

where $\phi_{th}\left(\frac{D}{2}\right)$ is the analytical value of the polymer volume fraction in a brush compressed to $D/2 < h$. Using the MWC prediction for the polymer density at the midpoint and Eq. (4.38) for δ, gives

$$I(D) \propto Z^{-2/3}\Sigma^{4/9}\tilde{u}^{-4/3}\left[1-\left(\frac{\tilde{u}}{\sqrt{5}}\right)^3\right] \, . \tag{4.40}$$

The quantity, $I(D)$, is defined for distances between the surfaces for $\tilde{u} \leq \sqrt{5}$. for $\tilde{u} \geq \sqrt{5}$ the interpenetration $I(D) = 0$. Since σ^* is an important and relevant quantity in the theoretical description of the polymer brushes, it is useful to express $I(D)$ in terms of this quantity. Doing so, Eq. (4.40) transforms into

$$I(D) \propto Z^{-2/15}\sigma^{*\,-4/9}\tilde{I}(\tilde{u}) \, . \tag{4.41}$$

with

$$\tilde{I}(\tilde{u}) = \tilde{u}^{-4/3}\left[1-\left(\frac{\tilde{u}}{\sqrt{5}}\right)^3\right] \, . \tag{4.42}$$

Figure 4.14 shows the result of fitting functional forms of Eq. (4.40) to the numerical SCF results. For this fit, all results which satisfy $\tilde{u} \gtrsim 0.6$ were included. $\tilde{I}(\tilde{u})$ as in Eq. (4.42) was used, but the powers of Z and σ^* were determined by the fit. It was found that

$$I(D) \propto Z^{-0.03}\sigma^{*\,-0.45}\tilde{I}(\tilde{u}) \, , \tag{4.43}$$

with the uncertainties ±0.02 in the values of exponents. The analysis performed here

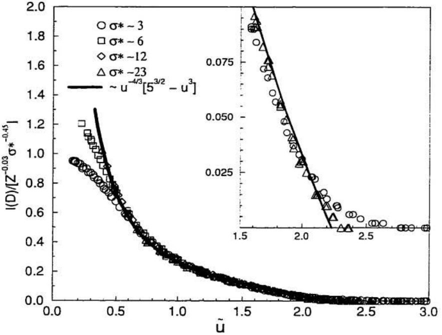

Figure 4.14: Interpenetration of two opposing brushes, $I(D)$, as a function of the reduced distance $\tilde{u}$, good solvent. The open symbols represent the numerical values, solid line is the line of the best fit to the functional form of Eq. (4.42) for all numerical values which satisfy $\sigma^* \sim 23$ and $\tilde{u} \gtrsim 6$. The inset shows the details for the initial stage of the compression.

is very similar to that described by Eqs. (4.26)-(4.31), but instead of four exponents only two have to be determined. Overall, the fit describes the curves very well and the fitted values of 0.03 ± 0.02 and 0.45 ± 0.02 can be compared directly with values found by Murat and Grest, which are $2/15 \simeq 0.133$ and $4/9 \simeq 0.44$. The slightly weaker dependence on Z for the numerical results is consistent with the weaker than linear scaling of the brush thickness with Z.

As is apparent from the inset in figure 4.14, there are interesting effects where the brushes first overlap. Those with lower values of σ^* start to interpenetrate for higher values of the reduced distance. This is consistent with the picture that, relative to the entire brush, the tail region is the largest for smallest σ^*. For small values of the reduced distance, $\tilde{u} < 0.6$, and $\sigma^* \sim 3$ the numerical results start to deviate from the universal format. This occurs as soon as the tail of the individual brush approaches the opposing surface. This deviation must occur since the functional form of $\tilde{I}(\tilde{u})$ diverges as $\tilde{u} \rightarrow 0$. On the other hand, a reasonable upper bound of $I(D)$ can be calculated from the extreme case of each brush profile being flat and extending fully to the opposite surface. In this case, $I(D) \rightarrow 1/2$, so the data as plotted on figure 4.14 must be bounded by $(Z^{0.03}\sigma^{*\,0.45}/2 \simeq \sigma^{*\,1/2}/2)$. The results shown there are consistent with this result, with the greatest deviation occurring for smaller σ^*. The onset of the deviation is at larger $\tilde{u}$ for smaller σ^*, occurring near $\tilde{u} \simeq 0.6$ for $\sigma^* = 3$, $\tilde{u} \simeq 0.4$ for $\sigma^* = 6$, and $\tilde{u} \simeq 0.4$ for $\sigma^* \geq 12$.

In summary the numerical results presented in this section confirm the interpenetration of the opposing brushes during compression and are in the very good agreement with the numerical results of Grest and Murat [101]. However, once again one can see the importance of the tail regions and relevance of the reduced surface concentration, σ^* during the compression, effects neglected in the MD studies of Grest and Murat [101].

4.4 Compressed Polymer Brush - Θ Solvent

In this section the properties of the polymer brush immersed in a Θ solvent and compressed either by the second identical brush or the two types of bare surfaces are investigated. As in the previous section, the main focus is the comparison of numerical SCF theory with the analytic predictions given by Shim and Cates [40] in their extension of the MWC analytic model of polymer brushes in a good solvent [29, 30].

Once again, model calculations for five different values of the degree of polymerization and three different surface coverages for each Z have been performed, as summarized in Table 3.4. As before, the free energy of the uncompressed brush is used a scaling variable, hence, the parameters used in the numerical calculation are the same as in chapter 3, i.e., the solvent polymer interaction parameter is $\chi = 0.5$, the statistical segments are chosen to have unit length, and the solvent and polymer pure component densities are set to unity. The reduced surface concentration is calculated by means of Eq. (3.36) with $\nu = 1/2$.

Before analyzing the results of the numerical SCF calculations, a short overview of the analytic theory of Shim and Cates for the Gaussian chains will be presented. As discussed in chapter 3, they predict an elliptic density profile for the brush in Θ solvent, given by Eqs. (3.42) and (3.43). Under compression of two brushes, there is no interpenetration of the opposing brushes, and the density profile of each brush retains its elliptic shape. It is given by[1]

$$\phi_B(x) = (12)^{1/4} A\left(\frac{D}{n_b}\right) \Sigma^{-1/2} b \left[1 - \left(\frac{x}{hA\left(\frac{D}{n_b}\right)}\right)^2\right]^{1/2} . \tag{4.44}$$

for $0 \leq x \leq D/n_b < h$, where h is the thickness of the uncompressed brush. Eq. (3.43). and the quantity $A\left(\frac{D}{n_b}\right) \equiv A$ has to be determined so that

$$\int_0^{D/n_b} \phi_B(x)\, dx = \frac{Zb^3}{\Sigma} . \tag{4.45}$$

This leads to

$$A = \left[\frac{\pi/2}{\frac{u}{A}\sqrt{1-\left(\frac{u}{A}\right)^2} + \arcsin\left(\frac{u}{A}\right)}\right]^{1/2} . \tag{4.46}$$

For $n_b = 2$ the second brush in the interval $[D/n_b, D]$ is described by the same functional form as Eq. (4.44) with x replaced by $D - x$, and Eq. (4.46) has to be solved numerically.

If one follows the formalism outlined in the work of Shim and Cates, and takes the self-consistent potential[2] to be proportional to $\phi_B^2(x)$, then the ratio of the free energy per unit area of the compressed brush to the free energy of the uncompressed brush is independent of the degree of polymerization and surface coverage and depends only on the reduced distance, $\tilde{u}$, as in Eq. (4.18). Hence, the free energy difference between the compressed and uncompressed brushes would be described by a single universal curve. The free energy of the compressed brush can be calculated as in the MWC

---

[1] As introduced in Eq. (4.14), $n_b = 1$ for a single brush compression and $n_b = 2$ for the compression of the two brushes.

[2] Using Flory-Huggins expression for the free energy of mixing F_{mix} [5] and relating the effective potential to the F_{mix} via the functional derivative $V = -\delta F(\phi(x)/\delta\phi$ [40]. In good solvent, the MWC theory predicts the self-consistent potential to be proportional to $\phi_B(x)$.

theory by selecting a chain near the surface and progressively adding chains. First the brush is built up to the equilibrium height, D/n_b, corresponding to some surface coverage Σ_1, then the brush height is fixed and the coverage increased from Σ_1 to Σ. The numerical procedure is described in the work of Shim and Cates [40] and MWC [29], and the result is given by

$$f_\Theta(u) = u^2 + \int_{u^2}^{1} z A_1^2 dz - 1 \, , \tag{4.47}$$

where A_1 satisfies

$$\frac{2}{\Pi} A_1^2 \left[\frac{u}{A_1 z} \sqrt{1 - \left(\frac{u}{A_1 z} \right)^2} + \arcsin \left(\frac{u}{A_1 z} \right) \right] = 1 \, . \tag{4.48}$$

In section 4.3.1, a simple measure of the deformation of the polymer brush, ξ, was introduced in Eq. (4.32). Since $x^0_{rms} = h/2$ for the elliptic profile of the uncompressed brush, it can be shown that ξ is related to u by

$$\xi = \sqrt{\frac{\pi}{2}} \frac{\sqrt{K(A, u)}}{I(A, u)} \, . \tag{4.49}$$

with

$$I(A, u) = \left[\frac{u}{A} \sqrt{1 - \left(\frac{u}{A} \right)^2} + \arcsin \left(\frac{u}{A} \right) \right] \, , \tag{4.50}$$

$$K(A, u) = \left[\frac{u}{A} \sqrt{1 - \frac{u^2}{A^2}} + \arcsin \left(\frac{u}{A} \right) - 2 \frac{u}{A} \left(1 - \frac{u^2}{A^2} \right)^{3/2} \right] \, . \tag{4.51}$$

and the quantity A has to be determined via the solution of Eq. (4.46).

Finally, in order to characterize the interpenetration, one can recall that according to Witten, Leibler and Pincus [136], the interpenetration depth, δ, does not depend on the solvent quality and is given by Eq. (4.38). Thus, the analysis performed in section 4.3.3 is also applicable to the polymer layers in Θ solvent. Using Eqs. (4.39),(4.44) and (4.46), it follows that $I(D)$, defined by Eq. (4.36), would satisfy

$$I(D) \propto Z^{-2/3}\Sigma^{2/3}\bar{I}_{\Theta}(u) , \tag{4.52}$$

where $\bar{I}_{\Theta}(u)$ is the function of reduced distance only, and can be expressed as

$$\bar{I}_{\Theta}(u) = u^{-1/3}\left[\frac{\frac{\pi}{2}\left(1-\frac{u^2}{A^2}\right)}{\frac{u}{A}\sqrt{1-\frac{u^2}{A^2}}+\arcsin\left(\frac{u}{A}\right)}\right]^{1/2} . \tag{4.53}$$

where once again the quantity A has to be determined via the solution of Eq. (4.46). In order to express Eqs. (4.46)-(4.53) in terms of $\tilde{u}$, the relation $u = \tilde{u}/2$ has to be used.

Using σ^{*}, rather than Σ, Eq. (4.52) transforms into

$$I(D) \propto \sigma^{*\,-2/3}\bar{I}_{\Theta}(\tilde{u}) , \tag{4.54}$$

which is a very interesting result: the interpenetration, $I(D)$ expressed in terms of reduced distance, $\tilde{u}$, and reduced surface concentration, σ^{*}, does not depend on the degree of polymerization.

4.4.1 Compression by a Repulsive Surface

In figure 4.15, a typical force curve and the corresponding density distributions are shown as a function of the separation between the surface with a brush and a bare repulsive surface. Qualitatively, the force and the density distributions are similar

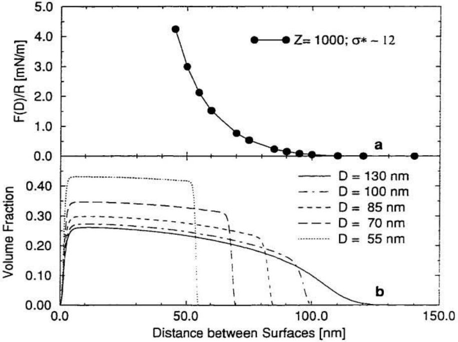

Figure 4.15: Compression of the polymer brush by a repulsive surface, Θ solvent. Force curve for polymer characterized by $Z = 1000$, and $\Sigma = 45$ nm^2 as a function of the separation between the plates (a). Density profile of the polymer brush during the compression (b).

to those for compression of the brush by a repulsive surface in a good solvent: the long-range force between surfaces is purely repulsive, and monotonically increases with decreasing separation. The density profiles, however, become more compact with deformation and, even for the moderate deformations, are step-like. In general, since the brush in a Θ solvent is more compact and the free energy is smaller than in a good solvent (the binary interactions, described by a excluded volume interaction parameter, vanish), less force is required to compress such a brush.

Looking for universal behavior of all the force curves describing the compression of the brush in these systems, the analysis described in the previous section, Eqs. (4.26)-(4.31) was performed. The best description of all the points which satisfy $F/R \geq 1\ \mu\mathrm{N/m}$ and $\sigma^* \geq 3$ is given by

$$\frac{F(D)}{R} = Z^{\alpha}\Sigma^{\beta} g\left(\frac{D}{Z^{\gamma}\Sigma^{\varepsilon}}\right) . \tag{4.55}$$

where $\alpha = 0.92 \pm 0.02$, $\beta = -2.04 \pm 0.02$, $\gamma = 0.88 \pm 0.02$ and $\varepsilon = -0.42 \pm 0.02$. In chapter 3, it was found that the thickness of the uncompressed brush in a Θ solvent can be described by an approximate power law dependence $x^0_{rms} \propto Z^{0.93}\Sigma^{-0.47}$, Eq. (3.45), which is very similar to the scaled distance determined through values of γ and ε respectively. Similarly, in chapter 3 the free energy per unit area of the uncompressed brush was found to satisfy $E_0 \propto Z\Sigma^{-2}$, and these powers are virtually the same as values of α and β.

These results imply that if the free energy difference per unit area between the compressed and uncompressed brush is scaled by E_0, and the distance between the plates is expressed in terms of the reduced distance, $\tilde{u}$, Eq. (4.24), then all the force curves should collapse to a single curve. The results of the numerical SCF calculations together with the theoretical curve calculated according to the Shim and Cates formalism [40] are shown in figure 4.16. For clarity, only extreme values of σ^* are shown. Once again, the points which correspond to different values of reduced surface concentration, σ^*, are dispersed from each other for weak compression, but overall are reasonably well described by a single curve. This effect suggests, as in the case

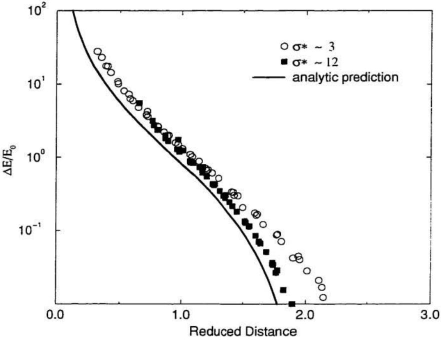

Figure 4.16: Compression of the polymer brush by a repulsive surface. Θ solvent. Free energy difference per unit area scaled by free energy of uncompressed brush as a function of the reduced distance given by Eq. (4.24). Symbols are the numerical results corresponding to different values of σ^*, and solid line is the analytic prediction of Shim and Cates [40].

of good solvent, that mainly the tail region of the profile is affected during the initial compression. In a Θ solvent the brush is more compact and the tail region is less pronounced than in a good solvent, thus there is less scatter of the data. Similarly the numerical results fall above the analytical prediction and the range and the magnitude of the force are underestimated by a factor of 2.

The scatter of the numerical results at the threshold of the repulsive force suggests that, as in the good solvent case, the parameter, ξ, describing the deformation, might be a better length scale. The dependence of ξ on the reduced distance $\tilde{u}$ is presented in figure 4.17. The symbols correspond to the numerical values and the solid line is the analytical prediction of Eq. (4.49). The data sets on order of $\sigma^* \sim 3$ start to be deformed for larger separation and approach the elliptic profile behavior at high compression. The data sets characterized by $\sigma^* \sim 12$ are well described by the analytic curve, although the profiles start to deform for $\tilde{u}$ slightly greater than 2, which is the value predicted by the analytic curve. Once again, the discrepancies between the numerical and analytic results reflect the fact that the latter neglects the tail region. For the larger values of σ^* the tail region is relatively short and, with increasing σ^*, the numerical results for the initial compression are in better agreement with the analytic prediction.

Considering the parameter ξ as a universal length scale, and free energy per unit area as the scaling variable for the free energy difference, all numerical data sets do collapse to a single curve and show reasonably good agreement with the analytic prediction. However the numerical results are above the line of the analytic prediction. This is shown in figure 4.18.

4.4.2 Compression by a Neutral Surface

Figure 4.19 shows a typical force curve and the corresponding density profiles for a brush characterized by $Z = 1000$, and $\Sigma = 45$ nm^2 compressed by a bare surface which is neutral for adsorption.

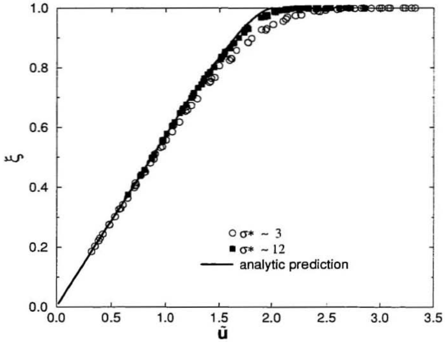

Figure 4.17: Compression of the polymer brush by a repulsive surface. Θ solvent. The parameter ξ as a function of the reduced distance $\tilde{u}$. Symbols correspond to the numerical values. solid line is the analytic function of Eq. (4.49).

The introductory remarks in the first paragraph of section 4.3.2 for a compression of a polymer brush in a good solvent by a such surface are applicable for this solvent. This can be seen through comparison of figure 4.19 with figure 4.15.

Turning attention to the universal behavior and looking for the function g and corresponding powers α, β, γ and ε which give the best description of the force curves. it was found that, for the regime $3 \lesssim \sigma^* \lesssim 13$, the best values of the exponents are $\alpha = 0.92 \pm 0.02, \beta = -2.04 \pm 0.02, \gamma = 0.94 \pm 0.02$ and $\varepsilon = -0.48 \pm 0.02$. These values are essentially the same as for compression of the polymer brush in a Θ solvent

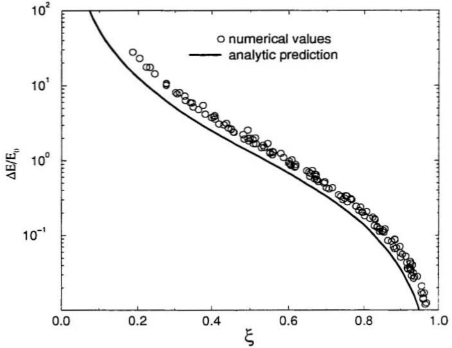

Figure 4.18: Compression of the polymer brush by a repulsive surface. Θ solvent. Free energy difference per unit area in μN/m scaled by free energy of uncompressed brush as a function of the parameter ξ given by Eq. (4.32). Symbols are the numerical results corresponding to all values of σ^*, and solid line is the analytic prediction obtained using the formalism of Shim and Cates [40].

by a repulsive surface, and correspond to the free energy and *rms* thickness of the uncompressed brush. Thus, this is equivalent to the universal behavior proposed by analytic theory and presented in figure 4.20. The numerical results reasonably well collapse to a single curve, even at the threshold of the force. This contrasts with the case of compression by a repulsive surface, in which this was the case only for the highest coverage, $\sigma^* \sim 12$, and for moderate values of compression. The numerical values of the free energy difference are in a good agreement with the analytic

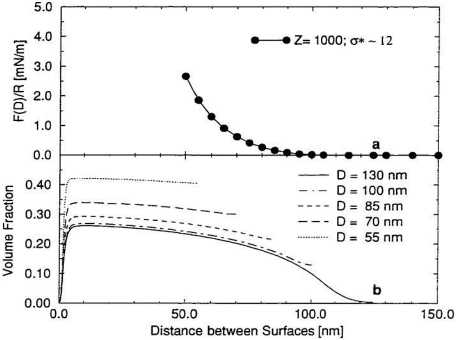

Figure 4.19: Compression of the polymer brush by a neutral surface, Θ solvent. Force curve for polymer characterized by $Z = 1000$, and $\Sigma = 45$ nm^2 as a function of the separation between the plates (a). Density profile of the polymer brush during the compression (b).

prediction for small and moderate compression.

Finally in figure 4.21 the equivalence of three modes of the compression is shown if the parameter ξ is used as the universal length scale. The numerical values of the free energy difference scaled by the free energy of the uncompressed brush plotted as a function of the parameter ξ are well described by a single curve, thus in this representation all three modes of compression can be considered as equivalent.

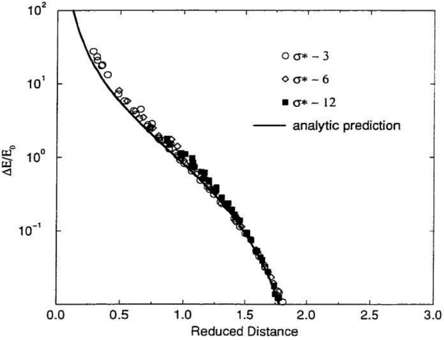

Figure 4.20: Compression of the polymer brush by a neutral surface. Θ solvent. Free energy difference per unit area in μN/m scaled by free energy of uncompressed brush as a function of the reduced distance given by Eq. (4.24). Symbols are the numerical results corresponding to different values of σ^*, and solid line is the analytic prediction of Shim and Cates [40].

4.4.3 Interpenetration of the Polymer Brushes

In section 4.3.3 the interpenetration of two polymer brushes during compression was investigated. Since the numerical SCF results and molecular dynamics studies indicate that the opposing brushes do interpenetrate in good solvent, this should also be anticipated in Θ solvent. The brushes in Θ solvent are not as stretched as in a good solvent, nor do the chains avoid contact to as great an extent.

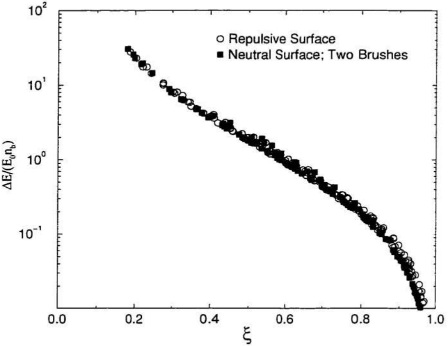

Figure 4.21: The equivalence of the three modes of compression. Θ solvent. The free energy difference scaled by the free energy of uncompressed system as a function of ξ parameter defined in Eq. (4.32).

In figure 4.22 the density profile of polymer $Z = 1000$, $\Sigma = 45$ nm^2 compressed to the reduced distance $\tilde{u} = 0.89$ is shown. The total calculated volume fraction is almost flat without a minimum at the midpoint, and the opposing brushes interpenetrate up to 1/2 of their total thickness. Pursuing the analysis further and looking for the powers α and β for which the numerical results collapse to a single curve

$$I(D) \propto Z^{\alpha}\Sigma^{\beta}\tilde{I}_{\Theta}(\tilde{u})\,, \tag{4.56}$$

where $f(\tilde{u})$ is some universal function of the reduced distance only, it was found

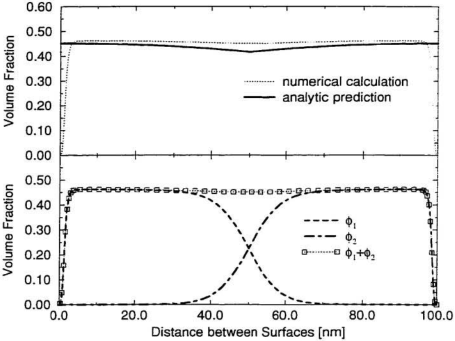

Figure 4.22: Compression of the polymer brush by a second identical brush. Θ solvent. Total density profile for the polymer with $Z = 1000$. $\Sigma = 45$ nm^2. numerical and analytic profile (a). Contribution of each brush to the total density (b).

$\alpha = -0.59 \pm 0.02$ and $\beta = 0.63 \pm 0.02$. If the reduced surface concentration. σ^*. instead of Σ is used Eq. (4.56) can be written as

$$I(D) \propto Z^{0.04} \sigma^{*\ -0.63} \tilde{I}_\Theta(\tilde{u}) \ , \tag{4.57}$$

with the uncertainties ±0.02 in the values of powers. This result is in a very good agreement with the exponents of Eq. (4.52) or Eq. (4.54). The numerical results plotted according to Eq. (4.57) are shown in figure 4.23. For the numerical values of $I(D)$ characterized by $\sigma^* \sim 12$, which satisfy $\tilde{u} \gtrsim 0.6$ and are scaled by $Z^\alpha \Sigma^\beta$. the

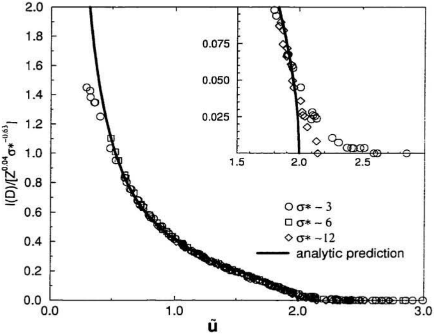

Figure 4.23: Interpenetration of two opposing brushes, $I(D)$, as a function of the reduced distance $\tilde{u}$, Θ solvent. The open symbols represent the numerical values, solid line is the line of the best fit to the functional form of Eq. (4.53) for all numerical values which satisfy $\tilde{u} \gtrsim 0.6$ and $\sigma^* \sim 12$. The inset shows the details for the initial stage of the compression.

best fit to the functional form of Eq. (4.53) has been determined and is presented as a thick solid line in figure 4.23. As is apparent from the inset in figure 4.23, the brushes characterized by $\sigma^* \sim 3$ start to interpenetrate for separations larger than those predicted by the analytic form, which, similar to the good solvent case, is caused by the fact that the tail region is the largest for smallest σ^*, and is neglected in the analytic description.

4.5 Summary

In this chapter the compression of polymer brushes in good and Θ solvents was studied. The prime interest was devoted to the compression of the brush in three different ways, first by a repulsive surface, then by a bare surface which is neutral for adsorption, and finally by a second, identical brush. The formal equivalence of two latter modes was established, i.e., it was shown that the density profile for a single brush compressed by a neutral for adsorption surface and the total density profile up to the midpoint between two surfaces for the compression of two brushes are the same. Similarly for a given separation, D, between the surface with the brush and the neutral surface the free energy is $1/2$ of the total free energy for compression of two brushes with the surfaces separated by a distance $2D$. Extensive numerical calculations for model values of the bulk densities of solvent and dangling block for wide ranges of degree of polymerization, Z, and average area per end-grafted chain, Σ, were performed and the results were compared with the analytical predictions of Milner, Witten and Cates [36, 133] for good solvent conditions, and with the generalization of this approach to Θ solvent, done by Shim and Cates [40].

For the compression of brushes in good solvent, the analytic theory of MWC underestimates the force and its range by a factor of about 2, and this numerical result is consistent with the recent experimental studies of Watanabe and Tirrell [52]. The numerical analysis shows the importance of the tail regions in the initial stage of the compression especially for low and the moderate surface coverages. With increasing coverage, the numerical results tend to be closer to the analytic prediction, but still the force and its range are larger than in the analytic picture. Satisfactory agreement with the analytic extension of the MWC theory proposed by Shim and Cates [40] was found. However for both good and Θ solvents, the compression of the polymer brush by the second brush is not equivalent to the compression by a repulsive surface. Instead, a properly defined deformation parameter should be considered as a universal length scale. In this representation all the modes of compression can be reasonably well described by a single curve.

The interpenetration of the polymer brushes during the compression in both good and Θ solvents was quantified and the results were in good agreement with the molecular dynamics simulations of Murat and Grest [101] for the interpenetration of brushes in good solvent.

Chapter 5

Lateral Compression - Excess Surface Pressure

5.1 Introduction

In this chapter the surface pressure effects in the adsorbed polymer layers are examined. First, the experimental results of Kent *et al.* [1, 2], as well as the recent numerical studies of Grest [82] and Carignano and Szleifer [90, 104] will be presented. Next, the theoretical approach and the details of the numerical calculations will be discussed. The following sections will be devoted to a homopolymer/poor solvent system with an attractive surface interaction and then to the copolymer/solvent system in which the anchoring block is the same as the homopolymer and the solvent is good for the dangling block. The results for the excess surface pressure for this system will be discussed and compared with the experimental, numerical and analytical studies.

The surface of a liquid comprised of small molecules is in a condition of tension, the most prominent evidence of which is its tendency to minimize the area of the surface of the liquid. The surface tension of a liquid can be traced to the force of attraction between its molecules. A molecule in the bulk of a liquid is surrounded by the maximum number of neighboring molecules so that its potential energy becomes minimum. The same molecule at the surface of the liquid is in contact with fewer molecules, since there are fewer neighboring molecules in the gaseous region just at the top of the interface. The energy of the molecule in the interfacial phase thus become greater than that in the bulk phase. The surface tension γ can be defined through Eq. (1.2) which is

$$\gamma = \left(\frac{\partial F}{\partial \mathcal{A}}\right)_{T,V,N_\kappa} , \tag{5.1}$$

where F is the Helmholtz free energy of the system with the interface. $\mathcal{A}$ is the total area of the interface, T is the temperature, V is the volume of the system, and N_κ are the numbers of the molecules present in the system. Thus if the system is comprised of pure solvent in contact with the air surface, it can be fully specified by the surface tension, γ_S.

Properties of the air-liquid interface of polymer solutions in good and Θ solvents have been extensively studied experimentally and theoretically. In the recent experiments of Kent *et al.* [137] the adsorption from solution of PDMS in a good (bromoheptane) and Θ (bromocyclohexane) solvents at the air-liquid interface was investigated. In this study, the effects of the molecular weight, bulk concentrations, and the solvent quality on the details of the density distribution of the polymer near the interface were explored. In both solvents, it was found that the polymer adsorbs at the surface and lowers the surface tension. The surface tension of pure PDMS is lower than the surface tension of either solvent used in the study. This difference provides the driving force for the adsorption. Thus, effectively one can think of an attractive interaction exerted by the surface on the polymer in solution. Similarly, in the study of Ober *et al.* [138], adsorption from solution of PDMS in toluene and of PS in toluene at the air-liquid interface was studied. Toluene is a good solvent for both polymers. It was found that PS adsorbs at the free surface and a concentration excess develops there. By contrast, the density of PDMS at the surface was lower than in the bulk. Similarly the surface tension of PDMS-TOL solution was lower than that of pure solvent, while it was greater for PS-TOL system. Once again the free surface of a solvent can be considered as a repulsive interface for one and attractive for the other polymer. Similar experiments were also performed in Θ solvents [25]. The difference between the surface tension of a clean interface (pure solvent) and of a surface with an adsorbed layer is often referred to as the surface pressure, Π, and is defined through Eq. (1.3).

As was mentioned in chapter 1, in most of the experimental and theoretical studies the change in the interfacial tension in the adsorbed polymer layers was investigated. However, the dependence of the surface pressure, Π, on the surface concentration and molecular weight for copolymer systems, although very interesting, have not been studied extensively. Most of the studies on lateral compression deal with Langmuir monolayers of amphiphilic molecules comprised of a hydrophilic head group and hydrophobic tail at the air-water or oil interface [102, 139].

The details of the structure of the density profiles for polymer chains terminally attached to the interface and under the influence of external potentials were investigated theoretically using the strong-stretching limit of the SCF theory by Marko *et al.* [106], and using the MC approach by Chakrabarti *et al.* [99]. The ideas introduced there, that the interfacial phenomena can be modeled using simple models of the external potential, are also employed in this thesis.

5.1.1 Experimental Studies on the Lateral Compression of Copolymers at the Air-Liquid Interfaces

To investigate the properties of the copolymer systems at the air-liquid interface Kent *et al.* [1, 2] performed a series of the experiments in which the surface pressure, Π, and its dependence on the surface concentration and molecular weight of both blocks was carefully examined. In most of the experiments, the layers of copolymer were formed by depositing onto the surface of ethyl-benzoate (EB) a small dry grain of PDMS-PS copolymer, from which the molecules spread spontaneously. The number of copolymer molecules per unit area, i.e., the surface density, was increased by adding further grains of copolymer to the surface and decreased by aspirating the surface with a movable barrier. Virtually all the chains were adsorbed to the interface; the total volume fraction of copolymer in the sub-phase (bulk solvent) was estimated to be always less than $\sim 10^{-6}$, and this was due to a spreading efficiency less than 100%. In addition, the spreading behavior of each homopolymer (PS and PDMS) was carefully examined. If the grain of pure PS homopolymer was deposited onto the EB surface, the PS molecules dissolved into the solvent after a short period of time, and there was no change in surface tension throughout the process. This indicates that PS is not active at the surface. Conversely, if the PDMS homopolymer was deposited onto the free surface of EB, the surface tension immediately started to drop. The PDMS homopolymer forms a stable Langmuir monolayer on the surface of this solvent, and this indicates that the surface is attractive toward the PDMS. The system under investigation is schematically presented in figure 5.1.

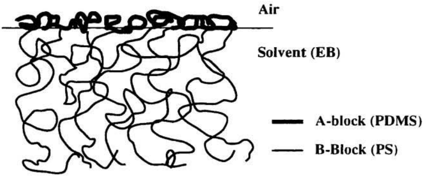

Figure 5.1: Illustration of the monolayer system formed by PDMS-PS diblock copolymer on EB.

Surface pressure-area isotherms were obtained for two different PDMS homopolymers, i.e., $M_w = 25,000$ and $100,000$ (g/mol), and 7 different copolymers, five of them being the same as those investigated in chapter 3 and listed in Table 3.1. The additional copolymers were 1.5-102 PDMS-PS and 10.5-40 PDMS-PS, where the polymers are labeled by the block molecular weights, in kg/mol, of the PDMS and PS blocks respectively. A rapid increase of the surface pressure-area isotherms for copolymer system in comparison to the pressure-area isotherm of pure PDMS homopolymer was observed in almost all the cases studied. The surface pressure excess, defined as the difference between the pressure of the copolymer/solvent and homopolymer/solvent systems for the same surface concentration of homopolymer, was found to vary relatively slowly for low surface coverage of the PS block of copolymer. However for large surface concentrations, it increased more quickly, approximately as $\Pi \propto \sigma^y$, with y in the range of 4.2-6.6 (see Table 5.2). This effect cannot be explained on the basis of the analytical models and is the prime subject of this chapter.

5.1.2 Previous Numerical Studies on the Lateral Compression of the Polymer Layers

The surface pressure, Π, and its dependence on the degree of polymerization, surface concentration and solvent quality were investigated numerically, using MD simulations, by Grest [82], and, using SCMF model, by Carignano and Szleifer [90, 104]. In the analytic pictures the surface pressure of the polymer brush in a good solvent is given by Eqs. (1.22) and (1.23) and predict a single scaling relation in the entire range of the surface concentrations.

Grest [82] carried out MD simulations of 4 chains in good and Θ solvents with Z ranging from 25 to 200 and surface coverages of $\sigma^* \lesssim 20$. The calculated dependence of surface pressure on the grafting density was somewhat stronger than predicted by analytic theories. In a good solvent, for chain lengths and grafting densities where the thickness of the brush, h, scaled as expected, i.e., $h \propto Z\sigma^{1/3}$, the surface pressure scaled as $\Pi \propto \sigma^{2.5}$. Grest explained this effect assuming that Π is much more sensitive to the finite monomer density than the brush height. This finite and high density in the center of the brush gives rise to purely steric effects which limit the interpenetration of the chains and is not included in either scaling or analytic SCF theories. To verify this hypothesis, simulations for much longer chains have to be carried out, and at the present this is not feasible [82]. Similarly, in Θ solvent Grest found that $\Pi \propto \sigma^3$, while both analytic theories predict $\Pi \propto \sigma^2$.

Carignano and Szleifer [104] performed numerical calculations applying the single-chain mean-field theory (SCMF) [89] for end-grafted polymer in good, Θ and poor solvents with $Z = 50$ and surface coverages of $\sigma^* \lesssim 40$. They found that the lateral pressure as a function of surface coverage in a good solvent can be described approximately by a power law with the exponent varying from 2.0 for very low surface coverage ($\sigma^* \ll 1$), to 1.9 for low surface coverage ($\sigma^* \lesssim 18$), and $\Pi \propto \sigma^{2.1}$ for intermediate surface coverage ($\sigma^* \lesssim 40$). They found good agreement between their calculated lateral pressure and the analytic SCF theory only when the parabolic density profile was used in the full virial expansion. In their later study [90] they extended the calculations for 4 different chains with Z ranging from 30 to 100 and surface coverages of $\sigma^* \lesssim 20$. In this work, they presented direct comparison with the experimental results of Kent [2]. They found that the lateral pressure can be described by a universal function of the reduced surface concentration σ^*, and their results were in good agreement with the experimental data up to $\sigma^* \sim 8$. For higher surface concentrations, the theoretical results deviated from the universal format and from the experimental values. They suggested that the experimental observations at large surface coverages were performed in a system that had not reached full equilibrium.

5.2 Numerical SCF Approach

The general numerical SCF formalism form was presented in chapter 2, and some other details which are relevant to the experiments of Kent *et al.* [1, 2] were presented in chapter 3. However, in chapter 3 it was assumed that the adsorbed A-block (PDMS) can be modeled by the simple, standard form of Eq. (3.1). Since in this chapter the effects of the surface pressure of polymer at the air-liquid interface are of the prime interest, this assumption is now eliminated, and the density distribution of the adsorbed A-block is determined self-consistently. Furthermore, two distinct cases have to be considered. The first is the pure homopolymer at the interface. The second is diblock copolymer with properties of the A-block identical to these of the homopolymer, and the B-block dangling into the solution. In both cases, the density distributions and the free energy of the system have to be calculated. In the following sections the numerical SCF formalism for these two cases will be presented.

5.2.1 The Homopolymer Spread as a Monolayer

The system under consideration is comprised of $\tilde{N}_{HA}$ identical homopolymer chains (PDMS) characterized by the density of the pure material, ρ_{0A}, statistical segment length, b_A, and degree of polymerization, Z_A, and $\tilde{N}_S$ solvent molecules (EB) characterized by ρ_{0S}. The partition function, Eq. (2.14), has the same form, except that $\tilde{N}_C$ has to be replaced by $\tilde{N}_{HA}$, and the summation is restricted to the A type molecules. Similarly, since the polymer consists of one type of monomer only, the $\delta(\cdots)$ functional which assures the connectivity has to be dropped. Following the formalism of Eqs. (2.15)-(2.26), the integral of the distribution function, Eq. (2.27) can be written as

$$\mathcal{Q}_H = \int d\boldsymbol{r}\, d\boldsymbol{r}' \boldsymbol{Q}_A(\boldsymbol{r}, Z_A|\boldsymbol{r}', 0)\mathcal{G}(\boldsymbol{r}'(0)) \, . \tag{5.2}$$

The density distribution of the homopolymer given by Eq. (2.48) has the form

$$\rho_A(\boldsymbol{r}) = \frac{\tilde{N}_{HA}}{\mathcal{Q}_H}\int_0^{Z_A} d\tau \left\{\int d\boldsymbol{r}'\, d\boldsymbol{r}'' \boldsymbol{Q}_A(\boldsymbol{r}, \tau|\boldsymbol{r}'', 0)\mathcal{G}(\boldsymbol{r}''(0))\boldsymbol{Q}_A(\boldsymbol{r}', (Z_A - \tau)|\boldsymbol{r}, \tau)\right\} \, . \tag{5.3}$$

As before, it is assumed that the system is translationally invariant parallel to the interface, and the problem is considered as one dimensional. Introducing the integral representation of the propagators in the same manner as in Eqs. (3.2) and (3.3), the propagator q_{0A} corresponds to Eq. (3.2) and the initial condition for this propagator satisfies Eq. (3.8). The second propagator q_{1A} is expressed as

$$q_{1A}(\boldsymbol{r}, \tau) = q_1(x, \tau) = \int d\boldsymbol{r}' \boldsymbol{Q}_A(\boldsymbol{r}, \tau|\boldsymbol{r}', 0)\mathcal{G}(\boldsymbol{r}') \, . \tag{5.4}$$

and the initial condition for this propagator is

$$q_{1A}(x,0) = \int d\boldsymbol{r}'\delta(\boldsymbol{r}-\boldsymbol{r}')\mathcal{G}(\boldsymbol{r}') = \mathcal{G}(x)\ . \tag{5.5}$$

Both propagators satisfy the diffusion equation, Eq. (3.4). In the experiments of Kent, the homopolymer forms a monolayer. Thus, one can assume that one end of every chain starts in the vicinity of the surface. Making use of Eq. (2.15) the propagator $q_{1A}(x,0)$ is assumed to satisfy

$$q_{1A}(x,0) = \exp\Big(-a_1x^2\Big)\ , \tag{5.6}$$

where a_1 is chosen so for $a = 1$ nm $q_{1A}(1,0) = 0.01$. This choice of the probability distribution for the free ends of the homopolymer limits the range of validity of the calculations to the cases in which the thickness of the A-block layer is on the order of 1 nm. This is consistent with the estimate that the thickness of the interphase is on the order of 1 nm [130], and with the experimental observations of Lee *et al.* [140] who determined the thickness of a PDMS monolayer on water from neutron reflectivity to be roughly 0.8 nm at full monolayer coverage. In terms of $q_{0A}(x,\tau)$ and $q_{1A}(x,0)$ the quantity $\mathcal{Q}_H$ is expressed as

$$\begin{aligned}\mathcal{Q}_H &= \int d\boldsymbol{r}d\boldsymbol{r}'\boldsymbol{Q}_H(\boldsymbol{r},Z|\boldsymbol{r}')\mathcal{G}(\boldsymbol{r}')\\ &= \int dx\,dy\,dz\,q_1(x,Z) = \mathcal{A}\int_0^\infty dx\,q_1(x,Z)\\ &= \mathcal{A}\mathcal{Q}_H^x\ .\end{aligned} \tag{5.7}$$

where $\mathcal{A}$ is the total area of the adsorbing surface and the local volume fraction of the homopolymer is given by

$$\phi_A(x) = \frac{N_A}{\rho_{0A} Q_H} \int_0^1 d\tau \, q_{0A}(x,\tau) q_{1A}(x, 1-\tau) \, . \tag{5.8}$$

where again τ was mapped onto $[0,1]$ and $N_A = \tilde{N}_{HA} Z_A$.

To determine the problem completely, the boundary conditions have to be specified. For a repulsive surface, the interface prefers solvent to the polymer, the chains avoid the interface, and this results in the depletion layer near the surface. If the surface prefers the polymer to the solvent there is an adsorption. Thus in the vicinity of the surface, the concentration profile is very sensitive to the details of the polymer-surface interaction. Therefore, it can be assumed that at $x = 0$ the density profile exhibits a local extremum (minimum or maximum) which implies

$$\frac{\partial}{\partial x} q_{iA}(x,\tau)\bigg|_{x=0} = 0 \, , \tag{5.9}$$

for $i = 0, 1$. These boundary conditions also express the fact that there is no flux of probability across the surface and have the effect of removing all configurations which cross the surface. These boundary conditions coincide with the idea of "configurational swap" introduced by Silberberg [141] and were used in the MC study of Bitsanis and Brinke [142]. Similarly, for the other boundary in a pure solvent it is set

$$\frac{\partial}{\partial x} q_{iA}(x,\tau)\bigg|_{x=\infty} = 0 \, , \tag{5.10}$$

which assures the continuity of the solution. In practice, however, these boundary conditions are applied at some finite distance L. The linear size of the system, L, is large enough so that, at $x = L$ there is no spatial variation in the densities of any of the components and the density is that of pure solvent.

The potential which modifies the diffusion equation Eq. (3.4) for this part of calculation is given by

$$\begin{aligned} \omega_A(x) &= \frac{\rho_{0S}}{\rho_{0A}}\chi_{AS}\left[\phi_S(x) - 1 - \phi_A(x)\right] + \frac{\rho_{0S}}{\rho_{0A}}\ln\frac{1}{\phi_S(x)} + u_A(x) - \frac{\rho_{0S}}{\rho_{0A}}u_S(x) \\ &= \omega_A^{int}(x) + u_A(x) - \frac{\rho_{0S}}{\rho_{0A}}u_S(x) \,. \end{aligned} \tag{5.11}$$

which was obtained in the same manner as Eq. (3.11) and the finite range of the potential Eq. (2.56) was, for simplicity, set to zero.

5.2.2 Diblock Copolymer at the Air-Liquid Interface

In this section the formalism for diblock copolymer (PDMS-PS) at the air-liquid interface of solvent (EB) is presented. Diblock copolymer consists of a block A characterized by degree of polymerization, Z_A, statistical segment length, b_A, and the density of pure material, ρ_{0A}. Similarly, block B can be characterized by Z_B, b_B and ρ_{0B}, and the solvent by its density, ρ_{0S}. Further, it is assumed that all the chains which are present in the system are adsorbed at the interface. This is consistent with the experiments of Kent *et al.* [1, 2] in which, as already mentioned, the total concentration of the copolymer in the sub-phase was negligible. The total number of copolymer chains adsorbed at the interface is $\tilde{N}_C$ and $\tilde{N}_S$ is the total number of solvent molecules in the system. Further, it is assumed that one block (A) has a higher affinity to the surface and the second block (B) extends into the solution and forms a polymer brush. The adsorbed A-block is the same as the homopolymer considered in the previous section. The formalism outlined in chapter 2 resulted in the density distribution for the A-block of copolymer given by Eq. (2.48) and the density of the other, B-block is given by Eq. (2.49).

Once again it is useful to introduce the integral representation of the propagators in which one integrates over all starting positions. In the copolymer/solvent system, four propagators are needed. The first one, denoted $q_A(x, \tau)$ is defined as

$$q_A(\boldsymbol{r}, \tau) = q_A(x, \tau) = \int d\boldsymbol{r}' \boldsymbol{Q}_A(\boldsymbol{R}, \tau|\boldsymbol{r}', 0)\mathcal{G}(\boldsymbol{r}'(0)) \ . \tag{5.12}$$

Since it is assumed that the free end of the A block is located near the surface, Eq. (5.12) is identical to Eq. (5.4) and satisfies the same initial conditions, Eq. (5.5). The second propagator, $q_B(x, \tau)$ is defined as

$$q_B(\boldsymbol{r}, \tau) = q_B(x, \tau) = \int d\boldsymbol{r}' \, \boldsymbol{Q}_B(\boldsymbol{r}, \tau|\boldsymbol{r}', 0) \ , \tag{5.13}$$

and satisfies the initial condition Eq. (3.8). This propagator, $q_B(x, \tau)$ reflects the fact that the free end of a B block could, in principle, be found anywhere in solution. Two other propagators are needed, and are defined as follows:

$$\tilde{q}_A(\boldsymbol{r}, \tau) = \tilde{q}_A(x, \tau) = \int d\boldsymbol{r}' \boldsymbol{Q}_A(\boldsymbol{r}, \tau|\boldsymbol{r}') q_B(\boldsymbol{r}', Z_B) \ , \tag{5.14}$$

and

$$\tilde{q}_B(\boldsymbol{r}, \tau) = \tilde{q}_B(x, \tau) = \int d\boldsymbol{r}' \boldsymbol{Q}_B(\boldsymbol{r}, \tau|\boldsymbol{r}', 0) q_A(\boldsymbol{r}', Z_A) \ . \tag{5.15}$$

The initial conditions for any point in the semi-infinite region, $x > 0$, are

$$\tilde{q}_A(x, 0) = q_B(x, Z_B) \ . \tag{5.16}$$

for $\tilde{q}_A$ and

$$\tilde{q}_B(x,0) = q_A(x, Z_A) \ , \tag{5.17}$$

for the propagator $\tilde{q}_B$. As in the case of homopolymer spread as a monolayer, it is assumed that all the propagators satisfy the same boundary conditions as previously, Eqs. (5.9) and (5.10). In terms of the propagators q and $\tilde{q}$, the densities can be expressed as

$$\phi_A(x) = \frac{N_{CA}}{\mathcal{Q}_C \rho_{0A}} \int_0^1 d\tau \, q_A(x,\tau)\tilde{q}_A(x, 1-\tau) \ , \tag{5.18}$$

$$\phi_B(x) = \frac{N_{CB}}{\mathcal{Q}_C \rho_{0B}} \int_0^1 d\tau \, q_B(x,\tau)\tilde{q}_B(x, 1-\tau) \ . \tag{5.19}$$

where $N_{CA} = \tilde{N}_C Z_A$ and $N_{CB} = \tilde{N}_C Z_B$ are the total number of monomers of type A and B respectively. The integral of the distribution functions, $\mathcal{Q}_C$, Eq. (2.27), becomes

$$\mathcal{Q}_C = \mathcal{A} \int_0^\infty dx q_A(x, Z_A) q_B(x, Z_B) = \mathcal{A} \mathcal{Q}_C^x \ . \tag{5.20}$$

The self consistent potentials which modify the diffusion equations for diblock copolymer/solvent system are given by

$$\begin{aligned} \omega_A(x) &= \frac{\rho_{0S}}{\rho_{0A}} \left\{ \chi_{AS} \left[\phi_S(x) - 1 - \phi_A(x) \right] + \phi_B(x) \left[(\chi_{AB} - \chi_{BS}) \right] + \ln \frac{1}{\phi_S(x)} \right\} \\ &\quad + u_A(x) - \frac{\rho_{0S}}{\rho_{0A}} u_S(x) \qquad (5.21) \\ &= \omega_A^{int}(x) + u_A(x) - \frac{\rho_{0S}}{\rho_{0A}} u_S(x) \ , \end{aligned}$$

and corresponding expression for $\omega_B(x)$.

5.2.3 The Model of the Interaction with the Surface

The terms which remain to be specified are the interactions of the homopolymer, solvent and copolymer molecules with the surface, $u_\kappa(x)$. In general, the monomers and solvent molecules interact through some intermolecular potential which can be described by Lennard-Jones or Morse type potentials [143]. In the mean-field approach to polymer/solvent systems, however, the interactions are described by a single parameter $\chi_{\kappa\kappa'}$. In the theoretical model presented in this thesis, the polymer chains and solvent molecules are confined in the x-direction by a planar surface which lacks the molecular roughness of real surfaces. As a result of this, any ordering of the system in the directions parallel to the interface is neglected and it is assumed that the potential energy due to the presence of the surface depends on the distance x from the surface and can be described in the mean-field fashion through energy and length parameters.

The interactions of the homopolymer or one block of copolymer with the surface appear in the formalism only in the self-consistent potentials which modify the diffusion equation, together with the solvent-surface potential energy. From Eq. (5.21), it follows that an effective surface-polymer potential can be introduced as

$$u_k^{eff}(x) = u_k(x) - \frac{\rho_{0S}}{\rho_{0k}} u_S(x) \ . \tag{5.22}$$

If the homopolymer molecules show a tendency to locate near surface or if there is adsorption of one block of the copolymer, the effective potential is attractive and this attraction extends over a distance at least on the order of a few statistical segment lengths. On the other hand, when the density profile of the homopolymer exhibits a depletion region or the diblock copolymer chains remain in solution, the surface can be considered as repulsive.

If $u_k^{eff}(x)$ is attractive and arises from L-J type interactions between the surface and the molecules in solution then this long-range potential is of the form [3, 144]

$$u_k^{eff}(x) \propto -\frac{1}{x^3} \,. \tag{5.23}$$

Thus, the repulsive surface can be modeled as

$$u_k^{eff}(x) = \begin{cases} \chi_S & \text{for } x \leq l \\ 0 & \text{for } x > l \end{cases} \,. \tag{5.24}$$

and the attractive surface as

$$u_k^{eff}(x) = \begin{cases} -\chi_S & \text{for } x \leq l \\ -\chi_S \left(\frac{x}{l}\right)^{-3} & \text{for } x > l \end{cases} \,. \tag{5.25}$$

where χ_S is the energy (in units of $k_B T$) and l the length parameter.

5.2.4 Free Energy of the System, Interfacial Tension and Surface Pressure

The general expression for the free energy for the copolymer/solvent system at the air-liquid interface was derived in chapter 2, and is given by Eq. (2.62). Substitution of Eq. (2.53) for the potential energy, W, and Eq. (5.21) for the self-consistent potentials,

$\omega_k(x)$, into Eq. (2.62) yields

$$\begin{aligned} F &= \frac{1}{2}\sum_{k=S,A,B} W_{kk}\rho_{0k}N_k + \tilde{N}_S\left(\ln\frac{\rho_{0S}}{\mathcal{Z}_S}-1\right) + \tilde{N}_C\left(\ln\frac{\tilde{N}_C}{\mathcal{Q}_C\mathcal{Z}_C}-1\right) \\ &+\mathcal{A}\rho_{0S}\int dx\left\{\frac{1}{2}\sum_{k,k'}\chi_{kk'}\phi_k(x)\phi_{k'}(x) + \phi_S(x)\ln\phi_S(x)\right. \\ &\left.-\sum_{k=A,B}\frac{\rho_{0k}}{\rho_{0S}}\omega_k^{int}(x)\phi_k(x) + u_S(x)\right\} , \end{aligned} \tag{5.26}$$

where the relation $\tilde{N}_S/\mathcal{Q}_S = \rho_{0S}$ was used and the reference density was explicitly set to the density of the pure solvent. For a pure solvent system of $\tilde{N}_S$ molecules and the surface, this free energy expression has the simple form

$$F_S = \frac{1}{2}W_{ss}\rho_{0S}N_S + N_S\left(\ln\frac{\rho_{0S}}{\mathcal{Z}_S}-1\right) + \mathcal{A}\rho_{0S}\int dx u_S(x) . \tag{5.27}$$

Using this, the free energy Eq. (5.26) can be written as

$$\begin{aligned} F &= F_S + \frac{1}{2}\sum_{k=A,B} W_{kk}\rho_{0k}N_k + \tilde{N}_C\left(\ln\frac{\tilde{N}_C}{\mathcal{Q}_C\mathcal{Z}_C}-1\right) \\ &+\mathcal{A}\rho_{0S}\int dx\left\{\frac{1}{2}\sum_{k,k'}\chi_{kk'}\phi_k(x)\phi_{k'}(x) + \phi_S(x)\ln\phi_S(x)\right. \\ &\left.-\sum_{k=A,B}\frac{\rho_{0k}}{\rho_{0S}}\omega_k^{int}(x)\phi_k(x)\right\} . \end{aligned} \tag{5.28}$$

Since the densities and potentials depend on the distance, x, from the interface, one can divide Eq. (5.28) by the total area of the interface to obtain the free energy per unit area, $f = F/\mathcal{A}$. In units of k_BT, f can be written as

$$\begin{aligned} f &= f_S + \frac{1}{2}\frac{1}{\Sigma}\sum_{k=A,B} W_{kk}\rho_{0k}Z_k + \frac{1}{\Sigma}\left(\ln\frac{1}{\Sigma\mathcal{Q}_C^x\mathcal{Z}_C}-1\right) \\ &+\rho_{0S}\int dx\left\{\frac{1}{2}\sum_{k,k'}\chi_{kk'}\phi_k(x)\phi_{k'}(x) + \phi_S(x)\ln\phi_S(x)\right. \end{aligned}$$

$$- \sum_{k=A,B} \frac{\rho_{0k}}{\rho_{0S}} \omega_k^{int}(x) \phi_k(x) \Bigg\} , \tag{5.29}$$

where, as before, $\Sigma = (\bar{N}_C/\mathcal{A})^{-1}$.

The free energy of the multicomponent system with a surface can be written as a Legendre transform of the internal energy with respect to entropy, and can be written as

$$F = \sum_{\kappa} \mu_\kappa N_\kappa - PV + \gamma \mathcal{A} . \tag{5.30}$$

and its total differential as

$$dF = -PdV - SdT + \sum_{\kappa} \mu_\kappa dN_\kappa + \gamma d\mathcal{A} . \tag{5.31}$$

In this representation, the interfacial tension, γ, is defined as the change in the total free energy when the interfacial area, $\mathcal{A}$, is increased at constant temperature T, total volume of the system, V, and constant numbers of particles in the system, N_κ.

The free energy per unit area depends explicitly on Σ, similarly the densities of homopolymer and every block of copolymer depend explicitly on Σ rather than on total area of the interface, $\mathcal{A}$. Taking this into account, the interfacial tension, γ, has to be expressed in a more convenient form

$$\begin{aligned} \gamma &= \left(\frac{\partial F}{\partial \mathcal{A}}\right)_{N_\kappa,T,V} \\ &= f + \mathcal{A}\left(\frac{\partial f}{\partial \mathcal{A}}\right)_{N_k,T,V} \\ &= f + \bar{N}_C \Sigma \left(\frac{\partial f}{\partial \Sigma}\right)_{\mathcal{A},T,V} \left(\frac{\partial \Sigma}{\partial \mathcal{A}}\right)_{N_\kappa,T,V} . \end{aligned} \tag{5.32}$$

Since $\mathcal{A} = \bar{N}_i\Sigma$ (i can be homopolymer, HA, or diblock copolymer, C), the result for constant T and V is

$$\gamma = f + \Sigma \left(\frac{\partial f}{\partial \Sigma} \right)_{\mathcal{A},T,V} . \tag{5.33}$$

For a pure solvent

$$\gamma_s = \rho_{0S} \int dx u_S(x) . \tag{5.34}$$

Furthermore, as is apparent from Eq. (5.33), all terms in f which are linear in $1/\Sigma$ do not contribute to γ. Finally the expression for the interfacial tension can be written as

$$\gamma = \gamma_s + \mathcal{L} + \Sigma \frac{\partial \mathcal{L}}{\partial \Sigma} , \tag{5.35}$$

where $\mathcal{L}$ is given by

$$\begin{aligned} \mathcal{L} \;=\; & \frac{1}{\Sigma} \ln \left(\frac{1}{\Sigma Q_C^x} \right) + \rho_{0S} \int dx \left\{ \frac{1}{2} \sum_{k,k'} \chi_{kk'} \phi_k(x) \phi_{k'}(x) + \phi_S(x) \ln \phi_S(x) \right. \\ & \left. - \sum_{k=A,B} \frac{\rho_{0k}}{\rho_{0S}} \omega_k^{int}(x) \phi_k(x) \right\} . \end{aligned} \tag{5.36}$$

As was mentioned in chapter 1 and in the introduction to this chapter, the change in the surface tension $\gamma_s - \gamma$ can be interpreted as a two-dimensional pressure, commonly referred to as the surface pressure

$$\Pi \equiv \gamma_s - \gamma , \tag{5.37}$$

which in the formalism presented above has the form

$$\Pi = -\mathcal{L} - \Sigma \frac{\partial \mathcal{L}}{\partial \Sigma} . \tag{5.38}$$

In order to analyze this result in detail, it is useful to transform Eq. (5.36) so that all the terms can be interpreted physically. As already noted in chapters 3 and 4, a constant value can be added to the self-consistent potentials without affecting any results. If the potentials for the A and B-blocks are chosen so that

$$\int_0^\infty dx\, \omega_k(x)\, \phi_k(x) = 0, \quad k = A, B \ . \tag{5.39}$$

then Eq. (5.36) becomes

$$\begin{aligned} \mathcal{L} \;=\; & \rho_{0S} \int dx \left\{ \frac{\rho_{0A}}{\rho_{0S}} \phi_A(x) u_A(x) + \frac{\rho_{0B}}{\rho_{0S}} \phi_B(x) u_B(x) + (\phi_S(x) - 1) u_S(x) \right\} \\ & + \rho_{0S} \int dx \left\{ \chi_{AB} \phi_A(x) \phi_B(x) + \chi_{AS} \phi_A(x) \phi_S(x) + \chi_{BS} \phi_B(x) \phi_S(x) \right\} \\ & + \frac{1}{\Sigma} \ln\left(\frac{1}{\Sigma Q_C^x} \right) + \rho_{0S} \int dx \phi_S(x) \ln \phi_S(x) \ . \end{aligned} \tag{5.40}$$

The first line can be interpreted as the contribution due to the external potential, the second line is the interaction energy within the components, and the third line can be interpreted as the entropic contribution to the free energy. Physically this entropic contribution includes effects due to chain conformations, chain localization and solvent distribution. Equation (5.40) can be written as

$$\mathcal{L} = \mathcal{L}_{ext}(\Sigma) + \mathcal{L}_{int}(\Sigma) + \mathcal{L}_{ent}(\Sigma) \ . \tag{5.41}$$

Using the condition of no volume change upon mixing (incompressibility), and setting $u_B^{eff}(x) = 0$, the first contribution can be written as

$$\mathcal{L}_{ext} = \int dx \rho_{0A} \phi_A(x) u_A^{eff}(x) \ . \tag{5.42}$$

Equations (5.40) and (5.41) are applicable to both the homopolymer/solvent and copolymer/solvent systems with appropriate modifications. Namely, for the homopolymer/solvent system, $\mathcal{Q}_C^x$ in the entropic part has to be replaced by $\mathcal{Q}_H^x$, and in $\mathcal{L}_{int}$ there are no terms for AB and BS interactions. The $\mathcal{L}_{ext}$ is the same for both systems, and can be interpreted as the anchoring energy.

5.3 Results and Discussion

As already mentioned, in the following sections the numerical results for homopolymers and diblock copolymers at the air-liquid interface of solvent will be presented and discussed. In order to make the comparison with the experimental observations, the densities of pure materials, statistical segment lengths and molecular weights of homopolymer and copolymer used in the calculations were chosen to agree, as closely as possible with the experimental values. The material characteristics for PS and EB are listed in chapter 3. For the homopolymer and the A-block of the diblock copolymer, which both correspond to PDMS, the following material characteristics were chosen: $\rho_{0A} = 7.89$ nm^3 and $b_B = 0.57$ nm [125, 145].

The PDMS-EB interaction parameter has not been measured, to the author's knowledge. Hence, a reasonable value needed to be chosen. Given that EB is a non-solvent for PDMS [1, 127], $\chi_{AS} = 0.7$ was used. The PDMS and PS polymers are not compatible and again, a reasonable interaction parameter was chosen. For this $\chi_{AB} = 0.1$ was used, which is typical of diblock copolymers systems [146, 147]. The

A-block of copolymer is restricted to the narrow interface, and there is a little overlap between A and B blocks, thus the results should not be sensitive to these choices of χ_{AS} and χ_{AB} parameters. Since the PS is not active at the surface it was assumed that u_B^{eff} is negligible and it was zero everywhere.

The PDMS homopolymer, when spread onto the surface of EB, forms a stable monolayer on the surface and the surface tension γ starts to drop, indicating that the surface is attractive toward the PDMS. To model this effect, the following effective potential was chosen

$$u_A^{eff}(x) = \begin{cases} -0.45 & \text{for } x \leq 0.7 \text{ nm} \\ -0.45\left(\frac{x}{0.7}\right)^{-3} & \text{for } x > 0.7 \text{ nm} \end{cases} . \tag{5.13}$$

These choices of the energy, χ_S = - 0.45, and length, $l = 0.7$, parameters were based on many numerical calculations, with the final values chosen to produce a reasonable description of the surface pressure isotherm for the homopolymer discussed in in the next section.

For a given system, which is specified by the values of the degree of polymerization of the homopolymer or the two blocks of the copolymer, the material characteristics discussed above, and the average number of chains per unit area, $1/\Sigma$, the self-consistent solution is found. The free energy of the system, given by Eq. (5.40), is then calculated. The surface pressure isotherms as a function of the surface coverage are obtained by numerical evaluation of Eq. (5.38) [134]; the numerical procedure is outlined in Appendix A.

5.3.1 Surface Pressure Isotherms - Homopolymer

To investigate the properties of the homopolymer at the air-liquid interface, numerical calculations for two PDMS homopolymers characterized by $M_w = 25,000$ and 50,000 g/mol ($Z_A = 337$ and 675 respectively) at the surface of EB were performed. For each homopolymer, the adsorbed amount, $\Gamma_A = Z_A/\Sigma$, was varied from just above 0 to almost 20 PDMS monomers/nm^2. The adsorbed amount, Γ_A, can also be defined as the total number of monomers per unit area which belong to the adsorbed layer

$$\Gamma_A = \rho_{0A} \int_0^\infty dx[\phi_A(x) - \phi_A^b] \, , \tag{5.44}$$

and since $\phi_A^b = 0$, Γ_A can be determined through the integration of the numerically generated profile. The difference between the value $\Gamma_A = Z_A/\Sigma$ and the value obtained by Eq. (5.44) is the measure of the accuracy of numerical calculations. In all the calculations discussed here this difference was always less then $1\times10^{-5}\%$.

Figure 5.2 shows the surface pressure isotherms for two PDMS homopolymers, $M_w = 25,000$ and $M_w = 50,000$, as a function of the number of adsorbed chains per unit area. For large values of Σ the surface pressure remains constant and essentially zero which means that the surface tension for small concentrations is the same as that of the pure solvent. The chains are isolated and only very weakly interacting. In the numerical studies of Carignano and Szleifer [104] it was found that for chains end-grafted to the surface and immersed in a poor solvent, the surface pressure is negative in some range of surface coverage which suggests that homopolymer chains

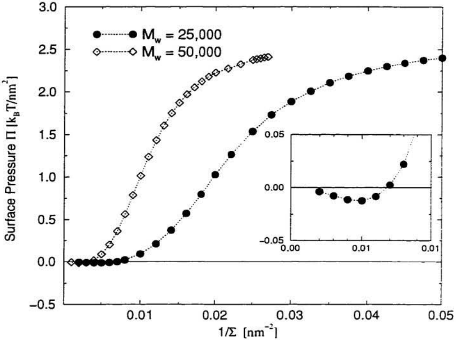

Figure 5.2: Surface pressure Π as a function of the number of adsorbed chains per unit area for PDMS homopolymers. $M_w = 25,000$ and $M_w = 50,000$. (The dotted lines are guides to the eye) The inset shows the behavior of the surface pressure Π for large values of Σ for $M_w = 25,000$.

prefer to form larger aggregates rather than replenish onto the surface. The inset in the figure 5.2 shows the surface pressure for large values of Σ. There is a narrow region where the surface pressure is negative. However, the surface pressure was obtained by the numerical differentiation of the functional $\mathcal{L}$, Eq. (5.40), and the accuracy in these and all subsequent calculations was estimated to be $(\delta\Pi)_{max} \lesssim 0.01$ k$_B$T/nm^2. Taking into account this accuracy, these negative values are too small, to confirm. As the area per adsorbed molecule decreases the surface pressure rises, but then it

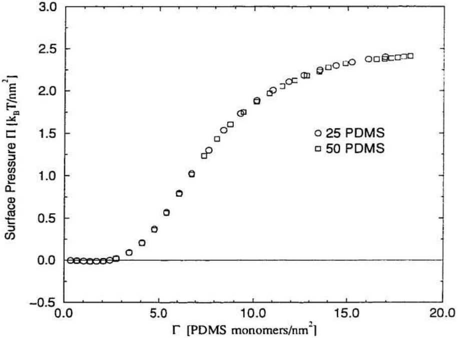

Figure 5.3: Surface pressure Π as a function of the number of adsorbed monomers per unit area for two PDMS homopolymer with $M_w = 25,000$ and $50,000$.

begins to to level off. This occurs at $1/\Sigma = 0.04$ nm^{-2} and $1/\Sigma = 0.02$ nm^{-2} for $M_w = 25,000$ and $M_w = 50,000$ homopolymer, respectively.

In figure 5.3 the numerical results of the surface pressure isotherms for two PDMS homopolymers as a function of the adsorbed amount, Γ_A are shown. In this representation, the isotherms collapse to a single curve, independent of the molecular weight of homopolymer. This is in perfect agreement with the observations of Kent *et al.* [1, 2].

This leveling off of the surface pressure at higher concentrations can be explained by the fact that for a given depth of the well, χ_S, characterizing the external potential, there is a maximum in the surface concentration for which all the chains in the system are tightly adsorbed onto the surface. Experimentally, beyond this maximum the steric repulsion among the chains becomes greater than the attraction toward the surface and the monolayer collapses, or the chains desorb [1]. The SCF model presented in this chapter lacks the desorption mechanism since the average area per adsorbed molecule is specified. However, as figure 5.4 shows, the density profiles exhibit a qualitative change at about this level of coverage. This figure shows the density profiles for the 25 PDMS homopolymer for six values of Σ. For very low coverage, the maximum density concentration at the surface is relatively low but the thickness of the profile is on the order of the width of the attractive well. As the coverage increases, i.e., as Σ decreases, the thickness of the profile remains almost constant but the average density within the layer increases. Beyond $\Sigma \lesssim 50$ nm^2, the maximum density saturates but the thickness of the layer begins to increase. The effect of the leveling off of the surface pressure occurs for coverage greater than a full monolayer so a significant fraction of the polymer falls beyond the attractive well. This leveling off of the surface pressure is in very good agreement with the experimental observations of Kent *et al* [1, 2]. At full monolayer coverage, $\Sigma \sim 33$ nm^2, most of the polymer can be found in a region on the order of 1 nm from the surface, consistent with the experimental data of Kent. Beyond a full monolayer coverage, the thickness of the layer becomes greater than the width of the region where the chain ends were

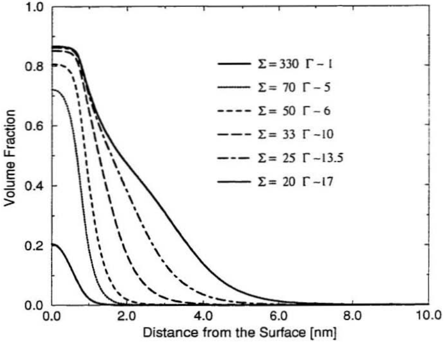

Figure 5.4: Density profiles for PDMS homopolymer with $M_w = 25.000$ for different values of the surface coverages. Surface coverage Σ expressed in units of nm^2. adsorbed amount Γ in numbers of adsorbed monomers per nm^2

assumed to start. This limits the calculations to $\Gamma_A \lesssim 10$ monomers/nm^2. In all subsequent calculations $\Gamma_A \sim 10$ PDMS monomers/nm^2 was chosen as the limit for which the PDMS homopolymer or the A-block of the diblock copolymer can be treated as forming the monolayer.

In summary, the surface pressure isotherms for the homopolymer adsorbed at the air-liquid interface depend on the total number of adsorbed monomers per unit area and are independent of the molecular weight of the adsorbed chains, at least for relatively high molecular weights. This can be understood, since the strong attraction toward the surface and poor solvent conditions lead to a collapsed layer and there is no stretching of the chains in the direction perpendicular to the surface. For small values of the surface concentration, a region of negative surface pressure can exist, which can be understood in a similar way to the attractive region observed during the compression of polymer brushes in the direction perpendicular to the surface in poor solvent conditions, where for the initial compression the opposing brushes reach out [64].

5.3.2 Surface Pressure Isotherms - Copolymer

In this section the numerical results for the lateral compression of the diblock copolymer/solvent system corresponding to the experiments of Kent *et al.* [1, 2] are discussed. The numerical calculation of the surface pressure isotherms as a function of surface coverage were performed for the six PDMS-PS copolymers studied in chapter 3. The degrees of polymerization of every block are listed in Table 5.1.

Table 5.1: Polymers used in the calculations. The polymers are labeled by the block molecular weights, in kg/mol, of the PDMS and PS blocks respectively.

Copolymer M_w	4-30	4.5-60	10-40	21-169	25-35	28-330
Z_A	54	61	135	283	337	378
Z_B	290	576	384	1625	336	3173

In figure 5.5 the surface pressure isotherms are shown as functions of surface coverage for all the asymmetric copolymers. In each case, Π varies slowly for small concentration and increases rapidly for larger values of $1/\Sigma$. The interesting part of

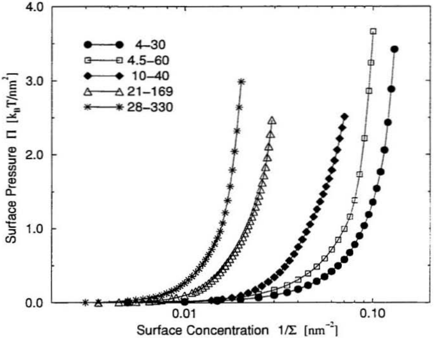

Figure 5.5: Surface pressure Π as a function of the surface concentration $1/\Sigma$. The polymers are labeled by the block molecular weights in kg/mol. of the PDMS and PS blocks, respectively.

all the curves is above the mushroom regime of the dangling block (PS), but even for $\sigma^* \sim 1$ the surface pressure is always positive. This can be understood since the PS block is in a good solvent and chains extend into the solution on the order of R_g, and neighboring chains effectively repel one another.

In order to compare the surface pressure isotherms for the diblock copolymer with that for the homopolymer, the surface pressure has to expressed as a function of the surface concentration of the A-block (PDMS). This comparison is presented in figure 5.6. For the 25-35 PDMS-PS copolymer, $Z_A \simeq Z_B$ and the isotherm falls very

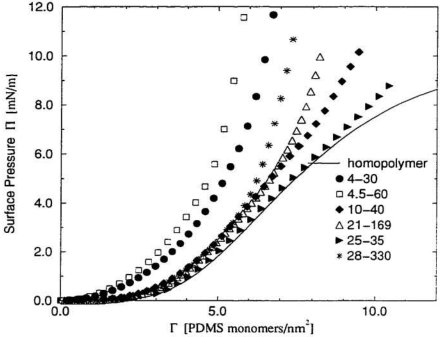

Figure 5.6: Comparison of the surface pressure, Π, for the diblock copolymer with homopolymer. The polymers are labeled by the block molecular weights in kg/mol. of the PDMS and PS blocks, respectively. T=300K as the ambient temperature was used to express the pressure in the units of [mN/m].

close to the homopolymer curve. This indicates that the surface pressure is mainly due to the interactions among the A chains and that the contribution from the dangling B-block is negligible up to the surface concentration, $\Gamma \simeq 9$ PDMS monomers/nm^2, where the deviation from the homopolymer isotherm begins. In general, as the asymmetry in the copolymer degrees of polymerization increases, the deviation from the homopolymer isotherm occurs at lower surface homopolymer concentration[1]. Since,

---

[1] The asymmetry can be defined as Z_{PS}/Z_{PDMS}, and for all the studied cases $Z_{PS} > Z_{PDMS}$, so the asymmetry is always larger than unity.

the surface pressure Π as a function of the adsorbed amount of A-block or PDMS homopolymer is independent of homopolymer molecular weight, and the A-block and its interaction with the surface are the same as the homopolymer, these deviations are due to the presence of the B-block.

As already mentioned, the surface pressure isotherm for the homopolymer is in good quantitative agreement with the experimental curve (with the appropriate choice of parameters, $\chi_S = -0.45$, $l = 0.7$ for the external potential and $\chi_{AS} = 0.7$ for the solvent quality). There is also qualitative agreement between the experimentally measured surface pressure isotherms and the numerical results. The copolymer isotherms rise more rapidly than the homopolymer isotherm and the order of the curves is the same as in the experiments. The isotherm for 4.5-60 PDMS-PS copolymer rises the most in this representation and is followed by the 4-30, 28-330, 21-169 and 10-40 PDMS-PS isotherms. The calculated surface pressure isotherms for copolymer are shifted toward larger values of adsorbed amount of PDMS compared with these obtained experimentally. In the experimental studies the isotherms for asymmetric copolymers were confined to concentrations smaller than 0.6 mg PDMS/m^2, which corresponds to approximately 5 PDMS monomers/nm^2. Numerical isotherms for these copolymers were calculated in the region $\Gamma \leq 10$ PDMS monomers/nm^2.

The fact that the numerically calculated surface pressure isotherms deviate from the homopolymer isotherm for surface concentrations, Γ_A, approximately 2 times larger than observed experimentally might be accounted for by the specific model of the external potential employed in the numerical work. For the asymmetric copolymer, the dangling PS block is large compared to the adsorbed PDMS block, and the PDMS forms a discontinuous layer on the surface. In the theoretical model it is assumed that the adsorbed block forms a continuous and uniform layer. This is a limitation of the theory, since these discontinuities cannot be described by a one-dimensional model. On the other hand, as pointed by Carignano and Szleifer [90] it is possible that the experimental observations of Kent *et al.* [2] were performed on a system that had not reached full equilibrium due to the long time scales necessary for lateral interpenetration in highly stretched polymer layers.

5.3.3 Surface Pressure Excess

To investigate the functional dependence of surface pressure due to the dangling blocks of copolymer, the surface pressure excess is defined as the difference between the pressure for copolymer/solvent and homopolymer/solvent systems for the same number of A-block and homopolymer monomers adsorbed at the surface, i.e.,

$$\Delta\Pi \equiv \Pi^{C}(\Gamma_A) - \Pi^{H}(\Gamma_A) \; . \tag{5.45}$$

where $\Gamma_A = Z_A/\Sigma$.

The surface pressure excess, $\Delta\Pi$, as a function of the number of chains per unit area $1/\Sigma$, is presented in the figure 5.7. In this figure only results for the most asymmetric copolymers, for which the surface pressure excess reached beyond 4 mN/m, are shown. The analysis for the 10-40 PDMS-PS is not included, because for this case

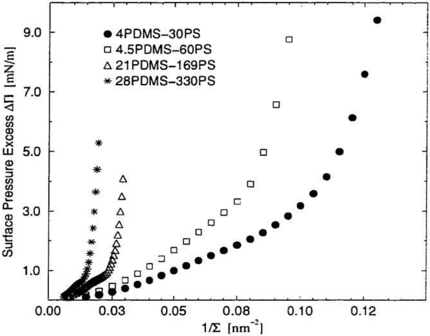

Figure 5.7: Surface pressure excess. $\Delta\Pi$ as a function of the number of chains per unit area.

the surface pressure excess exceeded 4 mN/m only for the concentrations larger than $\Gamma_A \simeq 10$ PDMS monomer/nm^2, where the approximation underlying the treatment of this block may be invalid, as discussed in section 5.3.1.

There are two distinct regimes for every curve. Initially. $\Delta\Pi$ increases relatively slowly but beyond some point it increases rapidly. To investigate this behavior. and in the spirit of searching for a power law dependence, the excess surface pressure curves were reploted on a log-log scale. A typical example is shown in figure 5.8 for the 28PDMS-330PS copolymer. In the first regime, the surface pressure excess can

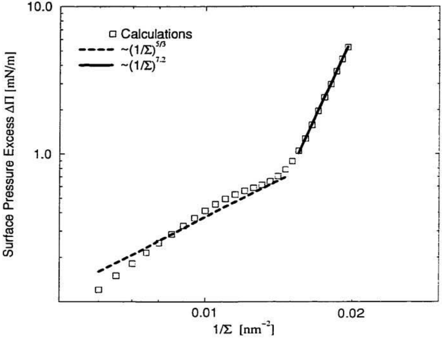

Figure 5.8: Two regimes for surface pressure excess, $\Delta\Pi$ as a function of the number of chains per unit area for 28-330 PDMS-PS copolymer. The solid line is fitted to the calculations. The dashed line is the line of the best fit using an assumed 5/3 power law dependence.

be described reasonably well by the power law dependence predicted by the analytic theory of MWC,

$$\Delta\Pi \propto \left(\frac{1}{\Sigma}\right)^{5/3} . \tag{5.46}$$

In the second regime, beyond about $\Sigma_l = 65$ nm^2 for this case, the results fall on another straight line, again implying a power law dependence. However, the value of the exponent is much larger, $\alpha = 7.2 \pm 0.1$ for this polymer. This rapid increase cannot be explained by the analytic theory. All four curves have similar behavior.

The values of the exponents and the approximate values of the Σ_I and $\sigma^*{}_I$ at which the second regime begins are listed in Table 5.2 for each case.

Table 5.2: Experimental and theoretical power law exponents obtained from fitting $\Delta\Pi \propto (1/\Sigma)^{\alpha}$, in the region where the deviation from analytic prediction is observed. Approximate theoretical values of the surface concentration, Σ_I, and reduced surface concentration $\sigma^*{}_I$ where the deviation begins. Polymers are labeled by block molecular weights, in kg/mol, of the PDMS and PS blocks respectively.

Copolymer M_w	Power law exponent-Experiment	Power law exponent-Theory ± 0.1	Σ_I [nm^2]	$\sigma^*{}_I$
4 - 30	4.2 ±1.0	5.3	10	9
4.5-60	4.4 ±0.4	5.2	15	13
21-169	6.6 ±0.6	8.2	48	16.5
28-330	5.6 ±0.9	7.2	65	24

In general, the larger the degree of polymerization of the dangling block, the larger is the reduced surface concentration, $\sigma^*{}_I$, at which the deviation from 5/3 scaling occurs. The values of the exponents are much higher than the value of 5/3 predicted by analytic theory, and are in semi-quantitative agreement with the values obtained in the experiments [2]. As already mentioned, in the numerical study of Grest [82] a value of 2.5 was obtained for all polymers and $\sigma^* \lesssim 20$, while Carignano and Szleifer [104] obtained a value of 2.4 for the scaling exponent over a similar range of Z and σ^*. The numerical values of the exponents obtained by Grest and Carignano and Szleifer are higher than 5/3 but still much lower than these obtained here and in the experimental studies of Kent *et al* [2].

To pursue the analysis further, the contribution of the particular terms in Eq. (5.41) to the total surface pressure isotherm can be analyzed. Using this equation, the surface pressure expression, Eq. (5.38), can be written as

$$\Pi = \Pi_{ext} + \Pi_{int} + \Pi_{ent} \, , \tag{5.47}$$

where each term corresponds to contribution to the $\mathcal{L}$ in Eqs. (5.40) and (5.41), and has the same physical origin.

In figure 5.9, the contribution, Π_{ext} as a function of Γ_A is shown. All the numerical values collapse reasonably well to a single curve obtained for both homopolymers. This implies that, although the external potential acting on the A-type monomers determines the overall dependence of the pressure on the surface concentration, it has a negligible effect on the rapid increase of the excess pressure for the copolymer.

Next, the contribution of the interactions between all the components in the system, Π_{int}, is considered and the results are presented in figure 5.10. For the homopolymer, the interaction energy $\mathcal{L}_{int}$ consists only of one term, i.e., the homopolymer-solvent interaction. Initially an increase in the surface concentration leads to an increase in the surface tension due to the interaction between homopolymer chains and the solvent molecules. This results in a negative contribution to the surface pressure. For higher values of the surface concentration, $\Gamma \gtrsim 5$ monomers/nm^2, the interactions per unit area saturate and then increase more than linearly in $1/\Sigma$. Similar behavior is observed for the symmetric copolymer, which once again indicates that the interaction between the dangling block and the solvent starts to contribute at higher surface concentrations. For the asymmetric copolymers, the surface pressure

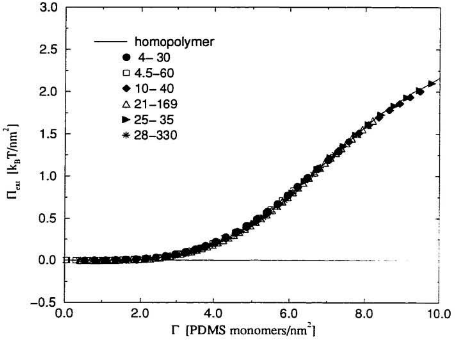

Figure 5.9: The contribution Π_{ext} to the surface pressure Π as a function of the number of PDMS monomers per unit area adsorbed onto the surface.

curves deviate from the homopolymer curve because the interaction between solvent and the dangling block contributes. As the surface concentration increases the total amount of the *B*-block increases and, since the dangling block is similar to an end-grafted polymer in a good solvent, interactions between the solvent and this block result in an increase of the surface tension. For higher surface concentrations, the surface pressure due to the interactions tends to be independent of Γ_A (the curves become flatter, in the same order as the surface pressure isotherms deviate from that of homopolymer).

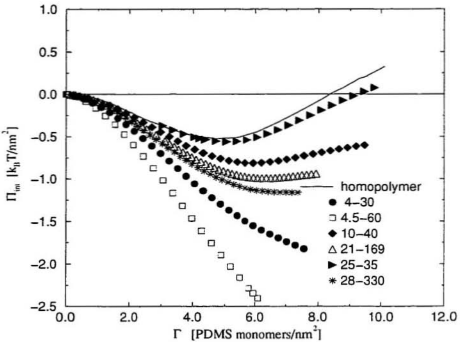

Figure 5.10: The contribution Π_{int} to the surface pressure Π as a function of the number of PDMS monomers per unit area adsorbed onto the surface.

Figure 5.11 shows Π_{ent}, the entropic contribution to the surface pressure. All the curves in this figure are controlled by the size of the A-block and the asymmetry ratio. By comparing this figure with figures 5.9 and 5.10, one sees that the entropic contribution is the main factor causing the rapid increase in the excess surface pressure found in the second regime. In the first regime, the interactions and entropy contributions lead to the relatively weak 5/3 scaling behavior. However, for the surface concentrations where the interaction contribution to the pressure, Π_{int}, tends to level off, or the rate of decrease becomes smaller, there is a rapid increase in the

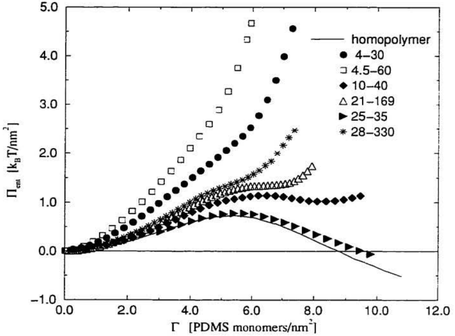

Figure 5.11: The contribution Π_{ent} to the surface pressure Π as a function of the number of PDMS monomers per unit area adsorbed onto the surface.

entropic contribution, Π_{ent}, to the total surface pressure, Π. The rapid increase in the surface pressure originating from the entropic interactions is in agreement with the conclusions drawn by Kent *et al* [2] and Grest [82]. They suggested that lateral interpenetration among neighboring chains is limited and may explain why the surface pressure rises more rapidly than predicted by analytic theories. More analysis of exactly why the numerical SCF produces this rapid increase, whereas the analytic SCF does not, is needed.

5.4 Summary

In this chapter the lateral compression of polymer layers at the air-liquid interface was investigated. A self-consistent formalism for the calculation of the surface pressure was introduced and the results of numerical calculations for different polymer/solvent systems at the air-liquid interface were presented.

First, the homopolymer/solvent system was studied. The solvent was assumed to be poor for the polymer. Furthermore, an attractive surface-monomer potential was introduced to simulate the adsorption of the chains at the surface. It was also assumed that all the homopolymer chains start at the surface, which corresponds to the formation of monolayer. The surface pressure isotherm as a function of the average number of chains per unit area was calculated for two homopolymers characterized by different degrees of polymerization. It was found that the surface pressure isotherm does not depend on Z_A if expressed as a function of the number of monomers adsorbed onto the surface. Good quantitative and qualitative agreement was found with the surface pressure isotherms obtained experimentally [1, 2].

Next, the diblock copolymer/solvent system at the air-liquid interface with one block equivalent to the homopolymer in the homopolymer/solvent system was considered. The second, B-block was assumed to be in a good solvent. The surface pressure isotherms as a function of surface coverage were obtained for six copolymers with different asymmetries. For the symmetric copolymer, the surface pressure isotherm was essentially the same as for the homopolymer system, and the contribution of the dangling block started to affect the isotherm for large values of the adsorbed amount of A type monomers. For the asymmetric copolymers the corresponding surface pressure isotherms deviated from that obtained for the homopolymer. The excess surface pressure for these copolymers was calculated and the results showed that this excess pressure can be divided into two distinct regions. In the first. the excess surface pressure can be well described by the analytic theories which predict a 5/3 power law dependence of the pressure on the surface coverage. In the second region. however. the power law dependence is much stronger than this predicted by analytic pictures. The calculated power law dependences in the second regime are in semi-quantitative agreement with these obtained in the experimental studies of Kent *et al.* [2] and much higher than the values predicted by analytic theories and some recent numerical studies [82. 104]. It was found that this rapid increase in the surface pressure can be explained on the basis of the entropic interactions between the chains. This entropic contribution to the surface pressure depends on both the asymmetry ratio and the molecular weight of the adsorbed A-block and is different from the entropic interactions in the homopolymer/solvent system. The numerical studies of Grest [82] and Carignano and Szleifer [104] consider only the dangling B-block. which may be why their surface pressure isotherms are described by a lower values of the exponents.

Chapter 6

Conclusions

The main goal of all the studies discussed in this thesis was to gain a better understanding of the physical properties of polymer/solvent systems near surfaces and interfaces. In particular, a major focus was on understanding the structure of polymer layers, the effects of solvent quality, the interactions among the polymer chains during compression and the behavior of polymer/solvent systems at the air-liquid interface. In all the studies, the results obtained through the numerical SCF theory were compared to the analytic predictions, as well as to experimental studies on similar systems. This chapter summarizes and concludes the work presented in this thesis. Extensions and prospective studies are also outlined.

6.1 Summary of the Results

The studies presented in this thesis are based on the numerical self consistent field approach. The polymer configurations are idealized as space curves and the partition function is written as a functional integral over the domain of configuration space. The introduction of the mean field approximation results in a set of coupled equations for the density profiles of every component, self-consistent potentials and a free energy expression written in terms of the densities and interaction parameters. The polymer, either homopolymer or each block of copolymer, is characterized by the degree of polymerization, Z_κ, segment statistical length, b_κ and the density of pure material $\rho_{0\kappa}$. The profiles for the polymers are calculated by solving the diffusion equations for the polymer distribution functions, $q_i(\boldsymbol{r},\tau)$, subject to geometry and the surface dependent initial and boundary conditions. The functions $q_i(\boldsymbol{r},\tau)$ are proportional to the probability that a section of length τ ends at $\boldsymbol{r}$ given that it starts in the interface or somewhere in the solution. The potentials $\omega_p(\boldsymbol{r})$ which modify the diffusion equation include enthalpic interactions between the molecules, written in terms of the Flory interaction parameters, as well as interactions with the surface, plus terms arising from the condition that there is no volume change upon mixing.

In chapter 3, the properties of uncompressed polymer brushes formed by the selective adsorption of the diblock copolymer or end-grafting and immersed either in a good or Θ solvent were discussed. In the case of a brush in good solvent, three regimes of stretching can be defined. The first is characterized by $\sigma^* \lesssim 2$, in which the chains extend from the surface a distance on the order of R_g of the free coil in a solution. In this case neighboring chains do not overlap. This corresponds to the mushroom regime, in which the SCF theory and the lateral averaging parallel to the surface are not suitable approximations. For $2 \lesssim \sigma^* \lesssim 20$ the neighboring chains start to overlap and begin to stretch away from the surface. This regime is characteristic of many experiments in good solvent. To date the systems studied by Auroy *et al.* [62, 56] and by Karim *et al.* [58] appear to be the only ones which fall into the third, asymptotic regime, $\sigma^* \gtrsim 20$. The scaling dependences of the thickness of the polymer brush on the degree of polymerization and surface coverage predicted by the analytic theories can be applied only in the third regime. In the regime $2 \lesssim \sigma^* \lesssim 20$ the scaling dependences found in this thesis are much weaker than predicted by analytical pictures, but are in very good agreement with the recent experimental studies of Kent *et al.* [1, 2].

This agreement motivated the next part of the study, in which a detailed comparison between the numerical SCF theory and the analytic pictures of polymer brushes in good and Θ solvent conditions was carried out. In good solvent conditions it was found that the numerically generated profiles extend further than those of the parabola. All the profiles have a depletion layer and an exponential-like tail region. The thickness of the end-grafted layer is about 50% thicker, and the maximum volume fraction is about 20% lower than in parabolic profile. The scaling relation of the thickness of the brush with the surface coverage and the degree of polymerization is significantly lower than that predicted analytically, but the difference becomes smaller with increasing reduced surface concentration, σ^*. The free energy of the brush obtained in the numerical theory is about 25% higher than predicted by analytic theory. The numerical results for the polymer brush in Θ solvent are in significantly better agreement with the analytic predictions. However, the numerically obtained density distributions still have characteristic depletion layers and tail regions, features which are absent in the elliptic type of the profile proposed by the analytic pictures. The free energy of the brush in a Θ solvent is in good agreement with the analytic predictions. The onset of stretching for the polymer brush in a Θ solvent appears at $\sigma^* \gtrsim 3$.

Different modes of compression of polymer brushes either in good or Θ solvent in the direction perpendicular to the grafting surface were the subject of chapter 4. The main goals of these studies were to find a universal description of the long-range force between the surfaces during the compression, and to analyze some very strong assumptions made in the analytic theories. The analytic pictures assume that, during the compression of the two identical polymer brushes, they do not interpenetrate: thus this mode of compression would be equivalent to the compression of the single polymer brush by a wall which is impenetrable for the chains and neutral for adsorption. Furthermore, the long range force between the surfaces can be described by the product of the free energy of the uncompressed brush and some universal function of the reduced distance which is defined as the ratio between the surfaces separation and the thickness of uncompressed polymer layer.

The numerical results differ from most of these assertions. For the compression of the polymer brush in a good solvent by a bare repulsive surface, they are dispersed if plotted according to the universal format proposed by the analytic picture of MWC, especially in the initial stage of compression. However, if only one value of σ^* is considered, the numerical results collapse reasonably well to a single curve. Together, these results imply that in this mode of compression it is mainly the tail region, neglected in the analytic picture, which is deformed. However, all the free energy difference curves do collapse to a single curve if plotted as a function of a simple measure of the deformation, i.e., the ratio of the *rms* thicknesses of the compressed and uncompressed total polymer density profiles. In this representation all three modes of compression become equivalent. For a polymer brush in a good solvent, the analytic theory underestimates the range of the force and its magnitude by a factor of 2 in comparison with the numerical results, in good agreement with the recent experimental observations. For the compression of two polymer brushes, the numerical results predict the interpenetration of the opposing polymer layers during compression, and are in very good agreement with MD simulations of Murat and Grest [101]. For the compression of a polymer brush in a Θ solvent the agreement between the numerical results and the extension of the MWC picture to different solvent conditions [40] was satisfactory. However, the advantage of the analytic theory over the numerical studies is lost since, even for the Θ solvent, there is no closed analytic form and the results have to be obtained through the numerical evaluations. As in a good solvent, the numerical results confirm the interpenetration effects neglected by Shim and Cates [40].

The final aspect of this thesis was a study of the lateral compression of polymer layers. Both blocks of the diblock copolymer were incorporated within the SCF treatment, and an effective external potential was introduced to model the adsorption of the polymer chains at the air-liquid interface. First a homopolymer/solvent system was studied. Surface pressure isotherms were calculated as a function of the surface coverage and compared with experimental observations. The isotherms for this system were found to be independent of the degree of polymerization of the adsorbed homopolymer if the surface coverage was expressed in terms of the adsorbed amount, Γ_A, at least in the range of the molecular weights used in the numerical studies.

Next, the diblock copolymer/solvent system was investigated. The adsorbing block of copolymer and the solvent were the same as in the homopolymer/solvent system. The calculated surface pressure isotherms as a function of the number of A-type monomers adsorbed at the interface depended strongly on the asymmetry of copolymer and also on the molecular weight of the A-block. For the symmetric copolymer the isotherm was essentially the same as for the homopolymer although differences occurred for large values of the surface concentration. The surface pressure isotherms for the asymmetric copolymers deviated strongly from the homopolymer isotherm. As the asymmetry in block length increases the deviation from the homopolymer isotherm occurs at a lower surface concentration of the A-block.

The excess surface pressure for these copolymers was calculated. The analytic pictures predict that the surface pressure for such a system should scale as $(1/\Sigma)^{5/3}$. The MD and SCMF studies predict a slightly higher value for the exponent. Two distinct regimes were found in the numerical results in this thesis. The excess surface pressure was described reasonably well by this scaling in the first regime. but deviated strongly from it in the second regime. A detailed analysis of the surface pressure isotherms showed that the entropic contributions result in the rapid increase of the surface pressure. The numerical calculations presented in this chapter are in semi-quantitative agreement with the experimental results of Kent *et al.* [2]. which are the only ones known to the author in which the rapid increase in $\Delta\Pi$ was observed.

6.2 Future Work

Polymer/solvent systems near surfaces and interfaces are far from being fully understood. While the theoretical studies presented in this thesis were able to answer a number of questions, there are many which remain to be addressed and resolved.

The SCF theory used throughout this dissertation can be extended and improved in many different directions. More detailed modeling of interactions among all the constituents, as well as interactions with the surface, can be investigated. The incorporation of fluctuations, especially at the tip of the brush where the polymer density is low, will provide a more detail picture of the polymer layers during compression. Finally, extensions of the model which allow for a non-uniform polymer density at the free surface of the solvent, as well as the inclusion of a desorption mechanism, would lead to a better understanding of the systems studied in chapter 5. More detailed and comprehensive studies are needed in order to reveal the scaling dependences of the excess surface pressure on the asymmetry ratio and degrees of polymerization of both blocks.

The structure and properties of the polymer layers can be studied in a variety of different geometries and under the influence of different external fields. More complicated architectures than linear diblock copolymers and polydisperse brushes can be considered. These are only some examples of possible challenging future projects.

Bibliography

[1] M. Kent, L. Lee, B. Farnoux, and F. Rondelez, Macromolecules **25**, 6240 (1992).

[2] M. Kent *et al.*, J. Chem. Phys. **103**, 2320 (1995).

[3] F. Garbassi, M. Morra, and M. Occhiello, *Polymer Surfaces. From Physics to Technology* (John Wiley & Sons, Chichester, England, 1994).

[4] G. Fleer and J. Lyklema, in *Adsorption from Solution at the Solid/Liquid Interface*, edited by G. D. Prafitt and C. H. Rochester (Academic Press, London, 1983), pp. 156–219.

[5] P.-G. de Gennes, *Scaling Concepts in Polymer Physics* (Cornell University Press, Ithaca, NY, 1979).

[6] H. Yamakawa, *Modern Theory of Polymer Solutions* (Harper & Row, New York, 1971).

[7] P. G. de Gennes, Macromolecules **13**, 1069 (1980).

[8] C. Marques and J. Joanny, Macromolecules **22**, 1454 (1989).

[9] C. Marques, J. Joanny, and L. Leibler, Macromolecules **21**, 1051 (1988).

[10] P. G. de Gennes, Macromolecules **14**, 1637 (1981).

[11] P. G. de Gennes, Advances in Colloid and Interface Science **27**, 189 (1987).

[12] P. G. de Gennes and P. Pincus, Journal de Physique - Letters **44**, L (1983).

[13] E. Bouchaud and M. Daoud, Journal de Physique **48**, 1991 (1987).

[14] C. Ligoure, Journal de Physique II **3**, 1607 (1993).

[15] D. Williams, Langmuir **9**, 2215 (1993).

[16] M. Aubouy, O. Guiselin, and E. Raphaël, Macromolecules **29**, 7261 (1996).

[17] J. Cahn and J. Hilliard, J. Phys. Chem. **28**, 258 (1958).

[18] I. Jones and P. Richmond, J. Chem. Soc. Faraday II **73**, 1062 (1977).

[19] C. Poser and I. Sanchez, Journal of Colloid and Interface Science **69**, 539 (1979).

[20] A. N. Semenov and J. Joanny, Europhysics Letters **29**, 279 (1995).

[21] S. Edwards, Proc. Phys. Soc. **85**, 613 (1966).

[22] A. Dolan and S. Edwards, Proc. R. Soc. Lond. **A 343**, 427 (1975).

[23] V. Aharonson *et al.*, Physica A. **204**, 1 (1994).

[24] P. J. Flory, *Principles of Polymer Chemistry* (Cornell Univ. Press, Ithaca, NY, 1953), p. 509.

[25] J. di Meglio *et al.*, Journal de Physique **44**, 1035 (1983).

[26] J. Klein and P. Pincus, Macromolecules **15**, 1129 (1982).

[27] G. Fleer *et al.*, *Polymers at Interfaces* (Chapman & Hall, London, 1993).

[28] S. Alexander, J. Phys. Fr. **38**, 983 (1977).

[29] S. T. Milner, T. A. Witten, and M. E. Cates, Macromolecules **21**, 2610 (1988).

[30] S. T. Milner, Journal of Polymer Science: Part B **32**, 2743 (1994).

[31] S. Patel and G. Hadziioannou, Colloids and Surfaces **31**, 157 (1988).

[32] K. F. Freed, *Renormalization Group Theory of Macromolecules* (John Wiley & Sons, New York, 1987).

[33] S. T. Milner, T. A. Witten, and M. E. Cates, Europhys. Lett. **5**, 413 (1988).

[34] V. A. Pryamitsyn, O. V. Borisov, E. B. Zhulina, and T. M. Birshtein, *Modern Problems in Physical Chemistry of Solutions* (Donish and Leningrad University, Dunshabe and Leningrad (USSR), 1987).

[35] A. N. Semenov, Sov. Phys JETP. **61**, 733 (1985).

[36] S. T. Milner, Europhysics Letters **7**, 695 (1988).

[37] S. T. Milner, Z.-G. Wang, and T. A. Witten, Macromolecules **22**, 489 (1989).

[38] S. T. Milner, T. A. Witten, and M. E. Cates, Macromolecules **22**, 853 (1989).

[39] S. Patel and M. Tirrell. Annu. Rev. Phys. Chem. **40**, 597 (1989).

[40] D. Shim and M. Cates, J. Phys. Fr. **50**, 3535 (1989).

[41] A. Halperin, J. Phys. Fr. **49**, 547 (1988).

[42] E. Zhulina, O. Borisov, V. Pyramitsin, and T. Birshtein. Macromolecules **24**, 140 (1991).

[43] E. Zhulina, O. Borisov, and V. Pyramitsin. J. Colloid Interface Sci. **137**. 495 (1990).

[44] A. Halperin and E. Zhulina, Macromolecules **24**, 5393 (1991).

[45] R. Ross and P. Pincus, Europhysics Letters **19**. 79 (1992).

[46] P.-Y. Lai and A. Halperin, Macromolecules **25**, 6693 (1992).

[47] T. Birshtein and Y. Lyatskaya, Macromolecules **27**. 1256 (1994).

[48] C. Yeung, A. Balzas. and D. Jasnow. Macromolecules **26**. 1914 (1993).

[49] G. Hadziioannou. S. Patel. S. Granick. and M. Tirrell. J. Am. Chem. Soc. **108**. 2869 (1986).

[50] J. Marra and M. L. Hair, Colloids and Surfaces **34**, 215 (1988/89).

[51] H. J. Taunton, C. Toprakcioglu, L. J. Fetters, and J. Klein, Macromolecules **23**, 571 (1990).

[52] H. Watanabe and M. Tirrell, Macromolecules **26**, 6455 (1993).

[53] H. Dhoot, S. anad Watanabe and M. Tirrell, Colloids and Surfaces A. **86**. 47 (1994).

[54] J. Israelachvili, M. Tirrell, J. Klein, and Y. Almog, Macromolecules **17**. 204 (1994).

[55] T. Cosgrove, T. G. Heath, J. S. Phipps, and R. M. Richardson, Macromolecules **24**, 94 (1991).

[56] P. Auroy, L. Auvray, and L. Leger, Phys. Rev. Lett. **66**, 719 (1991).

[57] L. Lee, O. Guiselin, B. Farnaoux, and A. Lapp, Macromolecules **24**, 2518 (1991).

[58] A. Karim *et al.*, Phys. Rev. Lett. **73**, 3407 (1994).

[59] M. Stamm, Advances in Polymer Science **100**, 357 (1992).

[60] M. Tirrell and E. Parsonage, in *Materials Science and Technology. A Comprehensive Treatment*, edited by R. Cahn, P. Haasen, and E. J. Kramer (VCH Verlagsgesellschaft mbH, Weinheim, Germany, 1993), Vol. vol. 12, pp. 653–697.

[61] J. B. Field *et al.*, Macromolecules **25**, 434 (1992).

[62] P. Auroy, L. Auvray, and L. Leger, Macromolecules **24**, 2523 (1991).

[63] M. Ansarifar and P. Luckham, Polymer **29**, 329 (1988).

[64] M. D. Whitmore and J. Noolandi, Macromolecules **23**, 3321 (1990).

[65] B. Deryaguin, Kolloid Zh. **69**, 155 (1934).

[66] H. J. Taunton, C. Toprakcioglu, L. J. Fetters, and J. Klein, Polymer **30**, 368 (1989).

[67] R. Roe, J. Phys. Chem. **60**, 4192 (1974).

[68] H. Ploehn, Macromolecules **27**, 1617 (1994).

[69] J. M. H. M. Scheutjens and G. J. Fleer, J. Phys. Chem. **83**, 1619 (1979).

[70] J. Scheutjens and G. Fleer, J. Phys. Chem. **84**, 178 (1980).

[71] J. Scheutjens and G. Fleer, Macromolecules **18**, 1882 (1985).

[72] O. A. Evers, J. Scheutjens, and G. J. Fleer, Macromolecules **23**, 5221 (1990).

[73] O. A. Evers, J. M. Scheutjens, and G. J. Fleer, J. Chem. Soc. Faraday Trans. **86**, 1333 (1990).

[74] O. A. Evers, J. Scheutjens, and G. J. Fleer, Macromolecules **24**, 5558 (1990).

[75] K. Binder, in *Molecular Level Calculations of the Structure and Properties of Non-Crystalline Polymers*, edited by J. Biscerano (Dekker, New York, 1990).

[76] D. Heermann, *Computer Simulation Methods in Theoretical Physics* (Springer-Verlag, Berlin, 1990).

[77] Y. Zhan, W. Mattice, and D. Napper, J. Chem. Phys. **98**, 7502 (1993).

[78] Y. Zhan, W. Mattice, and D. Napper, J. Chem. Phys. **98**, 7508 (1993).

[79] Y. Zhan and W. Mattice, Macromolecules **27**, 683 (1994).

[80] M. Murat and G. Grest, Macromolecules **22**, 4054 (1989).

[81] G. Grest and M. Murat, Macromolecules **26**, 3108 (1993).

[82] G. Grest, Macromolecules **27**, 418 (1994).

[83] F. Aguilera-Granja and R. Kikuchi, Physica A **189**, 81 (1992).

[84] M. Adamuti-Trache, E. McMullen, and J. Douglas, J. Chem. Phys. **105**, 1798 (1996).

[85] *Physics of Polymer Surfaces and Interfaces*, edited by I. Sanchez (Butterworth-Heinemann, Stoneham, MA (USA), 1992).

[86] D. H. Napper, *Polymeric Stabilization of Colloidal Dispersions* (Academic Press, London, 1983).

[87] S. T. Milner, J. Chem. Soc. Faraday Trans. **86**, 1349 (1990).

[88] C. Wijmans, J. Scheutjens, and E. Zhulina, Macromolecules **25**, 2657 (1992).

[89] M. Carignano and I. Szleifer, J. Chem. Phys. **98**, 5006 (1993).

[90] M. Carignano and I. Szleifer, Macromolecules **28**, 3197 (1995).

[91] K. Shull, Macromolecules **29**, 2659 (1996).

[92] A. Chakrabarti and R. Toral, Macromolecules **23**, 2016 (1990).

[93] P. Lai and K. Binder, J. Chem. Phys. **95**, 9288 (1991).

[94] M. Muthukumar and J.-S. Ho, Macromolecules **22**, 965 (1989).

[95] N. Dan and M. Tirrell, Macromolecules **26**, 6467 (1993).

[96] J. Martin and Z.-G. Wang, J. Phys. Chem. **99**, 2833 (1995).

[97] C. Wijmans, E. Zhulina, and G. Fleer, Macromolecules **27**, 3228 (1994).

[98] C. Singh and A. Balazs, J. Chem. Phys. **105**, 707 (1996).

[99] A. Chakrabarti, P. Nelson, and R. Toral, J. Chem. Phys. **100**, 748 (1994).

[100] R. Dickman and P. Anderson, J. Chem. Phys. **99**, 3112 (1993).

[101] M. Murat and G. Grest, Phys. Rev. Lett. **63**,, 1074 (1989).

[102] D. Langevin and J. Meunier, in *Micelles, Membranes Microemulsions, and Monolayers*, edited by W. M. Gelbart, A. Ben-Shaul, and D. Roux (Springer-Verlag, New York, 1994), Chap. 10. Interfacial Tension: Theory and Experiment, pp. 485–519.

[103] J. Martin, Z.-G. Wang, and M. Schick, Langmuir **12**, 4950 (1996).

[104] M. Carignano and I. Szleifer, J. Chem. Phys. **100**, 3210 (1994).

[105] P.-G. de Gennes, *Simple Views on Condensed Matter* (World Scientific, Singapore, 1992).

[106] J. F. Marko, A. Johner, and C. Marques, J. Chem. Phys. **99**, 8142 (1993).

[107] R. Baranowski and M. Whitmore. J. Chem. Phys. **103**. 2343 (1995).

[108] K. M. Hong and J. Noolandi, Macromolecules **14**, 727 (1981).

[109] K. M. Hong and J. Noolandi, Macromolecules **16**, 1083 (1983).

[110] J. Noolandi and K. Hong, Macromolecules **17**. 1531 (1984).

[111] E. Helfand, J. Chem. Phys. **62**, 999 (1975).

[112] E. Helfand, Macromolecules **8**, 552 (1975).

[113] E. Helfand, in *Recent Advances in Polymer Blends, Grafts and Blocks*, edited by L. Sperling (Plenum, New York, 1974).

[114] T. Ohta and K. Kawasaki, Macromolecules **19**, 2621 (1986).

[115] M. D. Whitmore and J. Noolandi, Macromolecules **21**, 1482 (1988).

[116] M. Banaszak, Ph.D. thesis, Memorial University of Newoundland. 1991.

[117] S. Edwards, Proc. Phys. Soc. **88**. 265 (1966).

[118] M. Doi and S. Edwards, *The Theory of Polymer Dynamics* (Calderon Press, Oxford, 1986).

[119] L. Schulman, *Techniques and Applications of Path Integration* (John Wiley & Sons, New York, 1981).

[120] F. Wiegel, *Introduction to Path-Integral Methods in Physics and Polymer Science* (World Scientific, Singapore, 1986).

[121] R. Feynman and A. Hibbs, *Quantum Mechanics and Path Integrals* (McGraw-Hill, New York, 1965).

[122] H.-H. Kuo, *Gaussian Measures in Banach Spaces*, Vol. 463 of *Lecture Notes in Mathematics* (Springer-Verlag, Berlin, 1975).

[123] J. Jensen, *Saddlepoint Approximation* (Oxford University Press, Oxford, 1995).

[124] H. Kleinert, *Path-Integrals in Quantum Mechanics Statistics and Polymer Physics* (World Scientific, Singapore, 1990).

[125] *Polymer Handbook*, 3rd ed., edited by J. Brandrup and E. H. Immergut (John Wiley & Sons, New York, 1989).

[126] *Dictionary of Organic Compounds*, 5th ed., edited by J. Buckingham (Chapman, New York, 1982).

[127] M. Kent, M. Tirrell, and T. Lodge, Polymer **32**, 314 (1991).

[128] Y. Higi, N. Ueno, and I. Noda, Polymer Journal **15**, 367 (1983).

[129] T. Cosgrove, J. Chem. Soc. Faraday Trans. **86**, 1323 (1990).

[130] M. Kent, personal communication.

[131] J. Israelachvili, Acc. Chem Res. **20**, 415 (1987).

[132] J. Israelachvili, Proc. Natl. Acad. Sci. USA **84**, 4722 (1987).

[133] S. T. Milner, Journal of Polymer Science: B **32**, 2743 (1994).

[134] *NAG Fortran Library, Mark 16*. NAG, 1994.

[135] R. R. Netz and M. Schick, submitted to Europhysics Lett. (unpublished).

[136] T. Witten, L. Leibler, and P. Pincus, Macromolecules **23**, 824 (1990).

[137] M. Kent, L. Bosio, and F. Rondelez, Macromolecules **25**, 6231 (1992).

[138] R. Ober *et al.*, Macromolecules **16**, 50 (1983).

[139] D. Andelman, F. Brochard, C. Knobler, and F. Rondelez, in *Micelles, Membranes Microemulsions, and Monolayers*, edited by W. M. Gelbart, A. Ben-Shaul, and D. Roux (Springer-Verlag, New York, 1994), Chap. 12. Structure and Phase Transitions in Langmuir Monolayers, pp. 559–602.

[140] L. Lee, E. Mann, D. Langevin, and B. Farnoux, Langmuir **7**, 695 (1991).

[141] A. Silberberg, Journal of Colloid and Interface Science **125**, 14 (1988).

[142] I. Bitsanis and G. Brinke, J. Chem. Phys. **99**, 3100 (1993).

[143] C. Kittel, *Introduction to Solid State Physics* (John Wiley & Sons, New York, 1986).

[144] Z. Y. Chen, J. Noolandi, and D. Izzo, Physical Review Letters **66**, 727 (1991).

[145] *CRC Handbook of Chemistry and Physics 74th ed.*, CRC, 1994.

[146] M. D. Whitmore and J. D. Vavasour, Macromolecules **25**, 2041 (1992).

[147] M. Banaszak and M. D. Whitmore, Macromolecules **25**, 3406 (1992).

[148] D. Potter, *Computional Physics* (John Wiley & Sons, London, 1973).

Appendix A

Computational Aspects of Calculations

In order to evaluate the density distributions of all the components of the system, as well as the free energy for a given system, a self-consistent solution has to be found. To do so, the original numerical program was written using Fortran 77, modified further to the F90 standard, and optimized to minimize the time needed to obtain the converged solution. The numerical calculations were performed on a number of platforms. At Memorial University of Newfoundland the code was run on Silicon Graphics R4000 Crimson workstations, a number of DEC Alpha systems and a Digital AlphaServer 4100. Through a scholarship provided by The High Performance Computing Centere in Calgary, access was granted to the Fujitsu VPX240, which is a vector supercomputer.

For a given system, which is specified by the values for Z_A, Z_B, Σ, ρ_{0B}, ρ_{0A}, ρ_{0S}, b_A, b_B, and the Flory interaction parameters χ_{AS}, and χ_{BS}, as well as the external potential, $u_A^{eff}(x)$, an iterative procedure is used to obtain a self-consistent solution.

To start the iterations, initial potentials, $\omega_i^{int}(x) = 0$, are chosen. The next step is the solution of the diffusion equations for all the propagators, $q_i(x,\tau)$, which are used in a particular problem. Then the corresponding density profiles are constructed through the proper convolution of propagators. The density profile for the solvent is determined by means of the incompressibility, which implies that the local volume fractions of all components sum locally to unity everywhere. From all the profiles, new potentials $\omega_i(x)$ are determined and a linear combination of the new and old potentials is used to initiate the next iteration. As the convergence criterion, $|\omega_i^n(x) - \omega_i^{n-1}(x)| \leq \delta = 10^{-7}$ for all x, and i is used, where $\omega_i^n(x)$ is the self-consistent potential for $i = A, B$ obtained at the n^{th} iteration.

The diffusion equation is solved via the Crank-Nicholson method [148] which is unconditionally stable and is accurate to second order in both the "time" (τ) and spatial steps. The procedure is particularly efficient and can easily be generalized to different boundary conditions used in this thesis.

In order to obtain the scaling relations, the non-linear least squares fitting routine E04GEF provided by NAG [134] was used. E04GEF is applicable to problems of the form

$$\text{Minimize } F(x) = \sum_{i=1}^{m} [f_i(x)]^2 \ . \tag{A.1}$$

where $x = (x_1, x_2, \ldots, x_n)$ and $m \geq n$, where n is the number of fitted parameters, and m is the number of points a given quantity has be determined. The functions

$f_i(x)$ are referred to as residuals, and if one looks for the fit of the form

$$G = a_1 Z^{a_2} \Sigma^{a_3} \,, \tag{A.2}$$

then these residuals are defined as

$$f_i(Z_i, \Sigma_i) = G_i - a_1 Z_i^{a_2} \Sigma_i^{a_3} \,. \tag{A.3}$$

This routine can be used if the functional form of the scaling relation is known, and the Jacobian matrix of first derivatives $\frac{\partial f_i}{\partial x_j}$ at any point x can be determined.

For the data collapse when the functional dependence of a given quantity was not a priori assumed, a similar method was used. However, in these cases the routine E04JAF, which does not require the Jacobian matrix, was used in fitting. This was used for the long range force as a function of scaled distance in chapter 4.

To evaluate the surface pressure as a function of the surface coverage, the derivative of the $\mathcal{L}$ functional, Eq. (5.40), with respect to Σ is required. In all cases, the functional $\mathcal{L}$ was evaluated for equally spaced values of Σ and this derivative could be approximated by

$$\left.\frac{\partial \mathcal{L}}{\partial \Sigma}\right|_{\Sigma_i} \simeq \frac{\mathcal{L}(\Sigma_{i+1}) - \mathcal{L}(\Sigma_{i-1})}{\Sigma_{i+1} - \Sigma_{i-1}} \,. \tag{A.4}$$

However, in order to take into account the fact that the functional $\mathcal{L}$ has been evaluated with finite accuracy and to include more than only two points in the evaluation of the derivative, the routines E02BCF, E02BEF supplied by NAG [134] were used. The routine E02BEF computes a cubic spline approximation, in the B-spline representation, to an arbitrary set of data points. The knots of the spline are located automatically, but a single parameter must be specified to control the trade-off between closeness of fit and smoothness of fit. The values of the functional $\mathcal{L}$ are on order of 0.1 k_BT/nm^2 for small values of $1/\Sigma$ to an order of 10 k_BT/nm^2 for the highest values of $1/\Sigma$. Performing many simulations with different grids in both Cartesian and "time" space and using REAL*8 and REAL*16 representations for the variables, the accuracy of calculations for the functional $\mathcal{L}$ was estimated to be on order of ± 0.0005 k_BT/nm^2. The value of the smoothness parameter, S, in all the calculations was chosen to be on this order (usually S$\sim$0.0001). On successful exit from the routine, the approximation returned is such that the sum of the squared residuals is equal to the smoothing parameter. The output of the E02BEF routine was used as an input to the E02BCF routine which evaluates the required derivative.

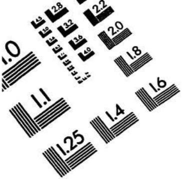

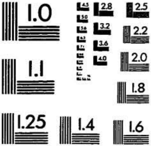

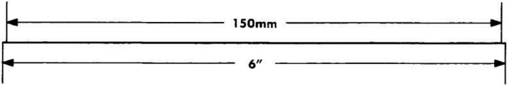

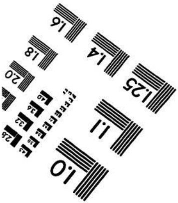

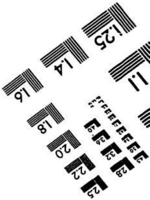

APPLIED IMAGE, Inc
1653 East Main Street
Rochester, NY 14609 USA
Phone: 716/482-0300
Fax: 716/288-5989